

· 90.520 2002

### LIBRARY Michigan State University

# This is to certify that the dissertation entitled

### DEFECT STRUCTURE AND TRANSPORT PROPERTIES OF NARROW GAP SEMICONDUCTOR PbTe AND RELATED SYSTEMS

presented by

#### SALAMEH M. AHMAD

has been accepted towards fulfillment of the requirements for the

Ph.D.	degree in	Physics
	$S.D. \cap$	chanli
	Major Pro	fessor's Signature
	Dece	ember 5, 2007
		Date

MSU is an affirmative-action, equal-opportunity employer

# **PLACE IN RETURN BOX** to remove this checkout from your record. **TO AVOID FINES** return on or before date due. **MAY BE RECALLED** with earlier due date if requested.

DATE DUE	DATE DUE	DATE DUE
	-	
	<b>-</b>	

6/07 p:/CIRC/DateDue.indd-p.1

# DEFECT STRUCTURE AND TRANSPORT PROPERTIES OF NARROW GAP SEMICONDUCTOR PbTe AND RELATED SYSTEMS

Ву

Salameh M. Ahmad

#### A DISSERTATION

Submitted to
Michigan State University
in partial fulfillment of the requirements
for the Degree of

**DOCTOR OF PHILOSOPHY** 

Department of Physics

2007

### **ABSTRACT**

# DEFECT STRUCTURE AND TRANSPORT PROPERTIES OF NARROW GAP SEMICONDUCTOR PbTe AND RELATED SYSTEMS

By

#### Salameh M. Ahmad

Understanding the detailed electronic structure of deep defect states in narrow band-gap semiconductors has been a challenging problem. Self-consistent ab initio calculations within density functional theory (DFT) using supercell models have been quite successful in tackling this problem. In this thesis, we carry out such calculations in PbTe and SnTe, two well-known narrow band-gap semiconductors, for a large class of defects: cationic and anionic substitutional impurities of different valence, and cationic and anionic vacancies. For the cationic defects, we study the chemical trends in the position of defect levels by looking at a series of compounds RQ<sub>2n-1</sub>Te<sub>2n</sub>, where Q is Pb or Sn, R is vacancy or monovalent, divalent, or trivalent atom. Similarly, for anionic defects, we study compounds  $MPb_{2n}Te_{2n-1}$ , where M is vacancy, S, Se or I. We find that the density of states (DOS) near the top of the valence band and the bottom of the conduction band get significantly modified for most of these defects. This suggests that the transport properties of PbTe and SnTe in the presence of impurities may not always be interpreted by simple carrier doping (from bound impurity states in the gap) concepts, confirming such ideas developed from qualitative and semi-quantitative arguments.

Transport coefficient calculations using the Boltzmann equation within energy-dependent relaxation time approximations have been carried out for n-type PbTe over a wide temperature (T) and concentration (n) range,  $300 \text{ K} \leq T \leq 900 \text{ K}$  and  $1 \leq n/n_0 \leq$ 

10,  $n_0 = 5 \times 10^{19} \text{cm}^{-3}$ . The nonparabolic Kane model for the energy dispersion was used in these calculations following the earlier work of Ravich et. al. Although the T dependence of the electrical conductivity  $\sigma$  comes from several sources (band structure parameters, chemical potential  $\mu$ , scattering relaxation time  $\tau$ ), we find that the T dependence of  $\tau$  dominates. We represent the temperature dependence and the energy of the electrons ( $\varepsilon$ ) dependence of the total relaxation time  $au_{tot}$  by a scaling function  $\left(\tau \sim \frac{aT^{-p}}{h+c\varepsilon^{r}}\right)$ , where a, b, c, p, r are T and  $\varepsilon$  independent parameters but depend on the carrier concentration. Using this simple scaling function in the calculation of  $\sigma$ , we find that for these concentrations changing the parameter r which governs the energy dependence of scattering does not appreciably affect the T dependence of  $\sigma$ . In addition to the study of the T dependence of  $\sigma$ , a careful electronic thermal conductivity calculation (both at constant current J and constant electric field E) was done to reexamine the validity of the Wiedemann-Franz (WF) law in PbTe, extending the earlier work of Bhandari and Rowe. We point out that using the standard WF law to estimate the electronic contribution of the thermal conductivity  $(\kappa_{el})$  usually overestimates this contribution by more than 0.5 W K<sup>-1</sup>m<sup>-1</sup>, and hence underestimates the lattice thermal conductivity. This has important implications in the question of how low the lattice thermal conductivity can go in the presence of nanostructures in PbTe.

To My Parents,

My Wife Haya ... My Son Omar

My Brothers ... My sisters

And

My Best Friend Mustafa

#### **ACKNOWLEDGMENT**

This work would not have been possible without the support and encouragement of my advisor Prof. S. D. Mahanti, under whose supervision I chose this topic and began the thesis. I would like to acknowledge Prof. M. G. Kanatzidis in Chemistry and Prof. Tim Hogan in Engineering for collaboration on the thermoelectricity project. Deepest appreciation goes to Dr. D. Bilc who has helped me a great deal in almost all aspects when I just started my research. Special thanks for K. Hoang and Z. Rak for the valuable assistance. I would also like to acknowledge Prof. Tessmer, Prof. Piermarocchi, Prof. Pratt and Prof. Schmidt for the support as members of my Guidance Committee. I would like to thank D. Simmons and C. Cords for taking care of all aspects of my graduate study and research. I would like to greatly acknowledge funding from the Office of Naval Research (MURI program) for financial support.

This joyful moment is especially for my family. My father, my mother, my wife, my brothers, and my sisters. I should have spent all the time with you all. This moment belongs to you all.

### **Table of Content**

List of Tables	viii
List of Figures	ix
Chapter 1	
Introduction	1
1.1 Why Study IV-VI Narrow Gap Semiconductors	1
1.2 Defects in Semiconductors: Shallow and Deep	
1.3 Transport Properties of Thermoelectrics	
Chapter 2	
Defects in Semiconductors	11
2.1 Point Defects	11
2.1.1 Intrinsic Point Defects	11
2.1.2 Extrinsic Point Defects	14
2.2 Evolution of Theory of Defects in Semiconductors	17
2.3 Density Functional Theory for Defect Calculations	
2.3.1 Density Functional Theory	
2.3.2 Full Relativistic Single Particle Dirac Equation	23
2.3.3 Scalar Relativistic Approximation	
2.3.4 Method of calculations	
2.4 Supercell Method	31
2.5 Issues with the Supercell Method in Defects Studies	33
Chapter 3	
Electronic Structure of Defects in PbTe	36
3.1 General Introduction	
3.2 Electronic Structure of PbTe	
3.3 Supercell Model to Calculate Defect Structure	
3.4 Pb-site Defects	
3.4.1 Pb Vacancy in PbTe	
3.4.2 Monovalent impurities (Na, K, Rb, Cs, Cu, Ag) in PbTe	
3.4.3 Divalent impurity (Zn, Cd, Hg, Sn, Ge) in PbTe	
3.4.4 Trivalent impurity (Ga, In, Tl, As, Sb, Bi) in PbTe	
3.5 Te-site defects	
3.5.1 Te vacancy in PbTe	
3.5.2 S and Se impurities in PbTe	
3.5.3 I impurity in PbTe	
3.6 Impurity-impurity interaction and the dilute defect limit	
3.7 Comparison with Experiments	
3.8 Summary	
Chapter 4	
Electronic Structure of Defects in SnTe	78
4.1 General Introduction	78

4.2 Electronic Structure of SnTe	79
4.3 Defects in SnTe	81
4.3.1 Sn vacancy in SnTe	82
4.3.2 Te vacancy in SnTe	
4.3.3 Ag impurity in SnTe	
4.3.4 Cd impurity in SnTe	
4.3.5 Sb impurity in SnTe	
4.3.6 In impurity in SnTe	
4.4 Summary	
Chapter 5	
Energy and Temperature dependence of relaxation time and Wiedemani	n-Franz law
in PbTe	
5.1 General Introduction	93
5.2 Transport Coefficients using the Boltzmann Transport Equation	95
5.3 Nonparabolic Kane Model for Energy Dispersion	
5.4 Transport Coefficients in the Kane Model	
5.5 Relaxation Time in the Kane Model	106
5.6 The Electronic Thermal Conductivity	115
5.7 Results and Discussions	
5.7.1 Energy and Temperature Dependence of the Relaxation time	
5.7.2 Electronic Thermal Conductivity and the Validity of Wiedemann-Fra	
5.8 Summary	
Chapter 6	
General Summary	130
Defense	126

### List of Tables

Table 3.1	Characteristics of the hyper-deep and deep defect states in PbTe with In impurity. Results obtained in PAW calculations using two different supercell sizes, (2x2x2) supercell (64 atoms/cell) and (3x3x3) supercell (216 atoms/cell). $E_{0v}$ and $E_{0c}$ are respectively at the bottom of the valence band (used as the reference for the hyper-deep states) and at the bottom of the conduction band (used as the reference for the deep states). $E_1$ and $E_2$ are respectively at the top and the bottom of the lower (upper) localized band formed by the hyper-deep (deep) defect state. W and $E_{av}$ are respectively the width and the average position of the lower and upper localized bands. All these quantities are measured in eV
Table 5.1	Parameters used to calculate the relaxation times for PbTe. [52, 106]111
	Inverse of the relaxation time of different scattering mechanisms in PbTe for different temperatures $T$ and different carrier energy $\varepsilon$

## List of Figures

Figure 2.1	Schematic representation of electronic states associated with the Vacancy. The shaded regions represent the conduction and valance states of the bulk. Left: the vacancy configuration before any relaxation of the neighbors: each broken bond contains one electron denoted by an up or a down arrow for the spin states, and all levels are degenerate, coincident with the Fermi level which is indicated by a dashed line. Right: the reconstructed vacancy, with pairs of broken bonds formatting bonding and antibonding states; the former are fully occupied, the latter empty, and the two sets of states are separated by a small gap. [54]
Figure 2.2	Schematic illustration of shallow donor and acceptor impurity states in semiconductor with direct gap. The light and heavy electron and hole states are also indicated; the bands corresponding to the light and heavy masses are split in energy for clarity. [54]
Figure 2.3	Division of a unit cell in <i>muffin tin</i> regions and the interstitial region, for a case with two atoms. The black dot is the origin of the axis system
Figure 2.4	Schematic presentation of the supercell construction of lattice vacancy in a solid
Figure 3.1	(a) fcc Brillouin zone of PbTe (b) Band structure of PbTe in fcc Brillouin zone at $V_{opt}$ . [23]
Figure 3.2	Supercell model of $RPb_{31}Te_{32}$ where $R$ is either a vacancy or an impurity atom. Small balls are for Pb and Te, large balls are for $R$
Figure 3.3	(a) The total DOS of PbTe with and without Pb vacancy, (b) the difference in the partial DOS between PbTe with and without Pb vacancy where the six nearest neighbor Te atoms of the Pb vacancy are denoted as Te2 and there are three other inequivalent Te atoms (denoted as Te1, Te3, and Te4), and (c) Atomic spheres ( $\Delta \rho_{at}$ ), and interstitial components $\Delta \rho_i$ of $\Delta \rho_{tot}$ . The energy origin in (b) and (c) is chosen to be the top of the valence band of PbTe; whereas the energy origin in (a) is the highest occupied Kohn-Sham single-particle state (which will be denoted as the Fermi energy) of the system with defect
Figure 3.4	The difference in the total DOS ( $\Delta \rho_{tot}$ ) between PbTe with and without monovalent impurities: Na, K, Rb, Cs, Cu, and Ag. The energy origin (0 eV) is chosen to be at the top of the valence band of PbTe
Figure 3.5	The difference in the total DOS ( $\Delta \rho_{tot}$ ) of PbTe with and without s-type divalent defects: Zn, Cd and Hg. The energy origin (0 eV) is chosen to be at the top of the valence band of PbTe

Figure 3.6 (	(a) The total DOS of PbTe with and without Cd impurity, (b) their difference $\Delta \rho_{\text{tot}}$ , (c) partial DOS per Te associated with nearest neighbor Te atoms, and (d) Cd partial DOS of s-character. The Fermi energy of PbTe with Cd impurity is at the energy origin (0 eV).
Figure 3.7	The difference in the total DOS ( $\Delta \rho_{tot}$ ) of PbTe with and without <i>p</i> -type divalent defects: Sn and Ge. The energy origin (0 eV) is chosen to be at the top of the valence band of PbTe
Figure 3.8	(a) The total DOS of PbTe with and without In impurity, (b) their difference $\Delta \rho_{\text{tot}}$ , (c) partial DOS per Te associated with nearest neighbor Te atoms, and (d) In partial DOS of s-character. The Fermi energy of PbTe with In impurity is at the energy origin (0 eV).
Figure 3.9	The difference in the total DOS ( $\Delta\rho_{tot}$ ) between PbTe with and without trivalent group III impurities: Ga, In, and Tl. The energy origin (0 eV) is chosen to be at the top of the valence band of PbTe
Figure 3.10	(a) The total DOS of PbTe with and without Ga impurity, (b) their difference $\Delta \rho_{\text{tot}}$ , (c) partial DOS per Te associated with nearest neighbor Te atoms, and (d) Ga partial DOS of s character. The Fermi energy of PbTe with Ga impurity is at the energy origin (0 eV)
Figure 3.11	The difference in the total DOS ( $\Delta \rho_{tot}$ ) between PbTe with and without trivalent group V impurities: As, Sb, and Bi. The energy origin (0 eV) is chosen to be at the top of the valence band of PbTe
Figure 3.12	(a) The total DOS of PbTe with and without As impurity, (b) their difference $\Delta \rho_{\text{tot}}$ , (c) partial DOS per Te associated with nearest neighbor Te atoms, and (d) As partial DOS of $p$ character. The Fermi energy of PbTe with As impurity is at the energy origin (0 eV).
	(a) The total DOS of PbTe with and without Te vacancy, (b) their difference $\Delta \rho_{tot}$ , and (c) partial DOS per Pb associated with nearest neighbor Pb atoms. The Fermi energy of PbTe with Te vacancy is at the energy origin (0 eV) 65
Figure 3.14	(a) The total DOS of PbTe with and without S impurity, (b) their difference $\Delta \rho_{\text{tot}}$ , (c) partial DOS per Pb associated with nearest neighbor Pb atoms, and (d) S partial DOS of $p$ character. The Fermi energy of PbTe with S impurity is at the energy origin (0 eV).
Figure 3.15	(a) The total DOS of PbTe with and without Se impurity, (b) their difference $\Delta \rho_{tot}$ , (c) partial DOS per Pb associated with nearest neighbor Pb atoms, and (d) Se partial DOS of $p$ character. The Fermi energy of PbTe with Se impurity is at the energy origin (0 eV).
Figure 3.16	(a) The total DOS of PbTe with and without I impurity, (b) their difference $\Delta \rho_{tot}$ , (c) partial DOS per Pb associated with nearest neighbor Pb atoms, (d) I

	partial DOS of p character. The Fermi energy of PbTe with I impurity is at the energy origin (0 eV)
Figure 3.1	The total DOS of PbTe with In impurity obtained in PAW calculations using two different models: InPb <sub>31</sub> Te <sub>32</sub> with one In impurity at the corner, and In <sub>2</sub> Pb <sub>30</sub> Te <sub>32</sub> with one In at the corner and the other one at the center of a (2x2x2) supercell; the distance between the two In impurities being 13.1 Å and 11.345 Å, respectively. The two lines are almost identical except at ~-0.5 eV and ~4.5 eV where the integrated DOS of the deep and hyper-deep defect states of In <sub>2</sub> Pb <sub>30</sub> Te <sub>32</sub> are larger than those of InPb <sub>31</sub> Te <sub>32</sub> by a factor of 2. The Fermi energy is at the top of the upper localized band formed by the deep defect state. [50]
Figure 3.18	The total DOS of PbTe with In impurity obtained in PAW calculations using two different supercell sizes, (2x2x2) supercell [InPb <sub>31</sub> Te <sub>32</sub> ] and (3x3x3) supercell [InPb <sub>107</sub> Te <sub>108</sub> ]; the distance between the two In impurities being 13.1 Å and 19.65 Å, respectively. The Fermi energy is at the top of the upper localized band formed by the deep defect state. [50]
Figure 4.1	Electronic energy band structure of SnTe calculated using GGA including SOI.[80]
Figure 4.2	Total Density of state of SnTe calculated using GGA including SOI
Figure 4.3	(a) The total DOS of SnTe with and without Sn vacancy, (b) their difference $\Delta \rho_{tot}$ , and (c) partial DOS per Sn associated with nearest neighbor Te atoms. The Fermi energy of SnTe with Sn vacancy is at the energy origin (0 eV) 83
Figure 4.4	(a) The total DOS of SnTe with and without Te vacancy, (b) their difference $\Delta \rho_{tot}$ , and (c) partial DOS per Te associated with nearest neighbor Sn atoms. The Fermi energy of SnTe with Te vacancy is at the energy origin (0 eV) 85
Figure 4.5	(a) The total DOS of SnTe with and without Ag impurity, (b) their difference Δρ <sub>tot</sub> ,. The Fermi energy of SnTe with Ag impurity is at the energy origin (0 eV)
Figure 4.6	(a) The total DOS of SnTe with and without Cd impurity, (b) their difference $\Delta \rho_{\text{tot}}$ , (c) partial DOS per Te associated with nearest neighbor Te atoms, and (d) Cd partial DOS of s-character. The Fermi energy of SnTe with Cd impurity is at the energy origin (0 eV).
Figure 4.7	(a) The total DOS of SnTe with and without Sb impurity, (b) their difference $\Delta \rho_{\text{tot}}$ , (c) partial DOS per Te associated with nearest neighbor Te atoms, and (d) Sb partial DOS of $p$ -character. The Fermi energy of SnTe with Sb impurity is at the energy origin (0 eV).
Figure 4.8	(a) The total DOS of SnTe with and without In impurity, (b) their difference $\Delta \rho_{tot}$ , (c) partial DOS per Te associated with nearest neighbor Te atoms, and

	(d) In partial DOS of s-character. The Fermi energy of SnTe with In impurity is at the energy origin (0 eV).
Figure 5.1	Energy dependence of the inverse of the relaxation time of the three dominant scattering mechanisms ( $\tau_a$ , $\tau_o$ and $\tau_{po}$ ) in PbTe for electron carrier density $t=5\times10^{19}$ cm <sup>-3</sup> at different temperatures (a) 300K (b) 600K (c) 900 K. The smooth curves gives the $(-\partial f_0/\partial \varepsilon)$ indicating the energy region contributing to the transport at different temperatures.
Figure 5.2	Temperature dependence of the chemical potential $\mu$ for <i>n</i> -type PbTe a different concentrations $n = 5 \times 10^{19}$ cm <sup>-3</sup> and $n = 5 \times 10^{20}$ cm <sup>-3</sup>
Figure 5.3	Temperature dependence of the electrical conductivity $\sigma$ and thermopower of the for <i>n</i> -type PbTe at concentration $n = 5 \times 10^{19}$ cm <sup>-3</sup> . The experimental values are shown as solid points from Ref [128]
Figure 5.4	Energy dependence of the total relaxation time $\tau_{tot}$ , calculated from Eq. 5.80 for <i>n</i> -type PbTe at concentration $n = 5 \times 10^{19}$ cm <sup>-3</sup> . for different temperatures
Figure 5.5	Energy dependence of the scaled (to 300K) total relaxation time $\tau_{tot}$ a different temperatures.
Figure 5.6	Energy dependence of the total relaxation time $\tau_{tot}$ for T=300 K
Figure 5.7	Temperature dependence of the total relaxation time $\tau_{tot}$ at $\varepsilon = 0.1$ eV 120
Figure 5.8	A comparison between the electrical conductivity $\sigma$ using the scattering mechanisms of the relaxation time with the scaled formula
Figure 5.9	A comparison between the thermopower S using the scattering mechanisms of the relaxation time with the scaled formula
Figure 5.10	0 (a) Temperature dependence of $\sigma$ , using the scaling formula of the total relaxation time for different $r$ parameter. (b) Temperature dependence of the scaled $\sigma$ (to $r = 1.74$ ).
Figure 5.1	1 Temperature dependence of the electronic thermal conductivity $(\kappa_{el})$ a constant electric field $E$ $(\kappa_{el,E})$ and at constant current density $J$ $(\kappa_{el,J})$ using Boltzmann transport equations. We also give their values using WF law 118
Figure 5.12	2 Temperature dependence of ZT for <i>n</i> -type PbTe at concentration $n = 5 \times 10^1$ cm <sup>-3</sup> assuming $\kappa_l = 0$
Figure 5.13	Temperature dependence of the scaled effective Lorenz number $(L/L_0)$ for n type PhTe at different concentration n $(L_0 = 2.45 \times 10^{-8} \text{ WOK}^{-2})$

# Chapter 1

## Introduction

### 1.1 Why Study IV-VI Narrow Gap Semiconductors

Narrow-gap IV-VI semiconductors are materials unique in their physical properties, the diversity of effects observed in them, and the possibilities for practical use. In particular, these compounds are the basis for creating infrared semiconductor lasers that can operate at near-room temperatures, highly efficient thermoelectric converters, and radiation detectors in the far-infrared and submillimeter ranges [88]. All the above possibilities are the consequence of a nontrivial combination of properties characteristic of the materials under consideration. These properties include the direct gap whose width can be smoothly varied by creating solid solutions, the high efficiency of radiative recombination, very high values of the static permittivity  $\epsilon$  up to  $10^4$ , and small effective masses of carriers  $\sim 10^{-2} m_0$ , where  $m_0$  is the mass of free electron. [88] As a result, the Coulomb potential of charged impurities in IV-VI semiconductors is almost completely screened. Therefore, it has no substantial effect on the mobility of carriers.

One of the important disadvantages of type IV-VI semiconductors is the high concentration of defects in their structure. For standard synthesis methods, the concentration of vacancies and interstitial atoms reaches  $10^{18} - 10^{19} \ cm^{-3}$ .[88] All the growth defects are electroactive, because of which the low carrier concentration necessary for a number of applications cannot be reached in undoped compounds.

Doping is one of the main methods for controlling the concentration of free carriers in semiconductors. The use of this method as applied to IV–VI semiconductors and, in particular, to lead telluride–based solid solutions not only allows the concentration of electrons and holes to be changed but also leads to the appearance of radically new properties uncharacteristic of the starting material. For example, when PbTe and a number of PbTe-based alloys are doped with group III impurities (indium, gallium, or thallium) the phenomena of Fermi-level pinning is observed. In this case, the Fermi-level position is determined by the alloy composition alone and is independent of the concentration of doping impurities and lattice defects [45]. In particular, a situation can arise when the Fermi level is stabilized within the band gap and a semi-insulating state is accomplished at low temperatures. Such a state is not observed in alloys that have not been specially doped.

PbTe was one of the first materials studied by Ioffe and his colleagues in the middle of the last century when there was a revival of interest in thermoelectricity.[4] This compound, its alloys with SnTe and PbSe, and related compounds called TAGS (alloys of AgSbTe<sub>2</sub> and GeTe) were for many years the best thermoelectric materials at temperatures ~700 K.[5] In recent years, quantum wells of PbTe/Pb<sub>1-x</sub>Eu<sub>x</sub>Te, PbSe<sub>0.98</sub>Te<sub>0.02</sub>/PbTe superlattices.[6] and quaternary compounds AgSbPb<sub>2m</sub>Te<sub>2m+2</sub> (m=9,10) [7] have attracted considerable attention because of their large thermoelectric figure of merit (FOM). Similar quaternary systems with Ag replaced by Na are also promising high temperature thermoelectrics.[8] Most of the above systems have stoichiometry closer to the parent compound PbTe.

### 1.2 Defects in Semiconductors: Shallow and Deep

The band gap, the energy region that is free of electronic states and is bounded by the valence and conduction bands, is the hallmark that differentiates metals, semiconductors, and insulators. Dopants and defects can dramatically modify the electrical conductivity of semiconductors as they add states in this band gap, which can provide electrical charge carriers (electrons or holes) to the respective bands at energies very much lower than the gap energy. Electrically active defects in semiconductor crystals have different characteristics, depending on the location of their energy states relative to the conduction- or valence-band edge. Shallow defects have energy levels within a few tens of millielectron volts from the respective band edges, whereas deep defects typically reside within the middle third of the semiconductor energy band gap. In fact the above simple definition and classification are no longer generally applicable. Instead one uses the degree of localization of the defect state to characterize this state. Deep levels have highly localized wave functions whereas shallow-level wave functions are as extended as the far reaching Coulomb potential. According to this definition, oxygen in GaN is a deep defect even though it is located inside the conduction band.[89] A shallow defect is easily explained. For example, a shallow donor resembles a hydrogen atom with a positive nucleus binding an electron. Two modifications to the hydrogenic model arise inside a solid. First, the mass of the electron is renormalized because of its interactions with the lattice. This "effective mass" is usually smaller than that of the free electron. Second, the crystal reduces the Coulomb potential caused by the dielectric screening. Combined, these two effects reduce the ground-state binding energy (ionization energy) of a donor, from the well-known 13.6 eV of the isolated hydrogen atom, down to, for example, merely 45 meV in Si. Other hydrogenic features remain: a series of bound excited states, which are observable with far-infrared spectroscopy, and the ionization into the energy continuum, that is, the conduction band in the case of a donor. This strikingly simple and effective hydrogenic model of shallow-level impurities or dopants has been amply confirmed with a broad range of electrical and optical studies of a vast number of dopants in numerous semiconductor materials.[90] The deep defects are much more difficult to understand.[91] Badly fitting impurity atoms distort the host lattice so extensively that the binding energy greatly exceeds that of shallow, hydrogenic defects. In wide band-gap semiconductors, the energy level lies "deep" within the forbidden energy band gap. Despite the availability of highly sophisticated computational tools, deep defects still represent one of the most challenging of problems of current semiconductor theory. Many atoms around the distorting defect must be considered when a first-principles calculation is attempted; the defect extends over many lattice constants. The carriers can interact strongly with the lattice. The effects of deep defects are to drastically reduce minority carrier lifetimes and to act as traps for charge carriers. Some deep defects can be used to pin the Fermi level near the middle of the energy gap and thus lead to highly resistive materials.

In Recent years a lot of progress has been made in tackling the deep defect states in wide band-gap semiconductors, using *ab initio* methods. For example, Lany *et. al.* [134] investigated theoretically using density functional theory the In *DX* center and the *DX*-like configuration of the Cd host atom in CdTe. Another well known example is P and As impurities in GaN. Mettila *et. al.* [135] found that P and As substitutional impurities in GaN induce deep levels in the band gap in contrast with all other

conventional III-V systems. The calculated exciton binding energy for (P)GaN has an excellent agreement with the available experimental data. In contrast to the wide bandgap semiconductors, the problem of defects in narrow-gap semiconductors, particularly the physics underlying the deep defect states, is far from understood. In these systems both shallow defects caused by the long-range Coulombic potential and deep defects formed by short range interactions and mixtures of these may coexist.

The theory of deep defects in narrow band-gap semiconductors has a long history. For substitutional defects in PbTe, Lent et al[14] presented a simple chemical theory of sand p-bonded substitutional impurities almost 20 years ago. This theory naturally gave deep defect states near the fundamental band gap and also predicted resonant levels further away from the gap. In this thesis we review the basic ideas underlying this theory and discuss the results of our recent attempts to understand the physics behind these deep defect states using first principle ab initio electronic structure calculations. We also discuss how these defect states get modified when different types of impurity microstructures are present. It is well-known that transport and optical properties of semiconductors are dominated by the states in the neighborhood of the band gap. Thus it is important to have a fundamental understanding of the changes in the electronic states near the band-gap region in PbTe when it is mixed with other binary and ternary compounds. Before being able to understand the nature of the electronic states near the band gap and/or the Fermi energy in the complex systems mentioned above, one must understand how the electronic states of PbTe change when Pb or Te is replaced by impurity atom or by vacancy.

Before studying the defect states in narrow band-gap semiconductors, one must understand their band structure without any defect. In recent years ab initio electronic structure calculation using density functional theory (within local density or generalized gradient approximations, LDA [61] or GGA [32]) have been extremely successful in unraveling the electronic structure (including the band gap) of many narrow band gap semiconductors with complex crystal structures. Examples are: skutterudites [117], and ternary bismuth chalcogenides systems (BaBiTe<sub>3</sub> [119] and CsBi<sub>4</sub>Te<sub>6</sub> [120]). Although the fundamental reason for this success is not known, the subtle nature of the origin of gap formation (i.e. hybridization, spin-orbit interaction etc.) in these compounds may be responsible for the above mentioned quantitative agreement. [119, 120] Even in systems where the quantitative predictions of LDA/GGA are not that good, one has been able to understand the physics of gap formation., the nature of bonding, and the parentage of states contributing to the transport properties of these narrow band gap semiconductors.[121] It is clear that ab intio electronic structure calculations are able to provide great insight about the physical properties of complex systems.

### 1.3 Transport Properties of Thermoelectrics

The efficiency  $\eta$  of thermoelectric (TE) energy conversion depends on the transport coefficients of the constituent materials through the figure of merit (FOM)  $ZT = \sigma S^2 T/(\kappa_l + \kappa_{el,J})$ , where  $\sigma$  is the electrical conductivity and S is the thermopower (Seebeck coefficient) [9]. The quantity in the denominator is the thermal conductivity; it is given by the sum of contributions from the electronic carriers at constant electrical current  $\vec{J}$  ( $\kappa_{el,J}$ ) and the lattice contribution  $\kappa_l$ . ( $\eta \to \eta_{carnot}$  when  $ZT \to \infty$ ) Z has units of inverse temperature, so it is generally quoted as a dimensionless number ZT, with T the

absolute operating temperature of the TE device [9]. TE devices are usually made from semiconductors. From the definition of ZT, it is clear that, to increase ZT we have to decrease the thermal conductivity of the material and/or increase the thermopower and the electrical conductivity. Among the four quantities involved in ZT, three of them  $(\sigma, S)$  and  $(\kappa_{el,j})$  are mainly related to the electronic structure of the material and the fourth one  $(\kappa_l)$  is mainly related to the lattice. One possible way to improve the FOM is to reduce  $(\kappa_l)$  without significantly altering the electronic properties of the materials, referred to as electron crystal phonon glass concept [92]. This approach has been explored extensively in the past [93, 94] through the enhancement of phonon scattering. The other way to improve the thermoelectric properties of a material is to increase the power factor  $(\sigma S)^2$  by varying the doping concentration and manipulating the electronic structure in the neighborhood of the chemical potential [95, 96]. In this thesis we focus on the electronic contributions to the thermoelectric properties of PbTe.

PbTe is a well known for its excellent thermoelectric properties. It is used for power generation in the temperature range 400 to 800 K [97]. In general, iodine and PbI<sub>2</sub> are the ordinary dopants for n-type PbTe used to optimize the carrier concentration [98]. But the lattice thermal conductivities of PbTe with these dopants are too high ( $\sim 2.2$  WK<sup>-1</sup>m<sup>-1</sup> at 300 K and  $\sim 1.1$  WK<sup>-1</sup>m<sup>-1</sup> at 650 K) [132] to restrain application (ZT has only been  $\sim 0.1$  at 300 K and  $\sim 0.9$  at 650 K). [98, 132] Therefore many methods have been used to reduce  $\kappa_l$  of PbTe, such as hot pressing and spark plasma sintering (SPS) techniques [99]. The lattice thermal conductivity of PbTe samples prepared by hot pressing is about  $2WK^{-1}m^{-1}$  which is much higher than the ideal value of 1 WK<sup>-1</sup>m<sup>-1</sup> needed for good thermoelectric materials as pointed out by Mahan [100]. Although there

are many successful examples of reducing the thermal conductivity of PbTe by alloying such as in  $Pb_{1-x}Sn_xTe$ , a product of PbTe alloyed with SnTe, and  $(Bi_{1-x}Sb_x)_2Te_3$  solutions [100], recently, novel bulk quaternary systems  $AgPb_mSbTe_{m+2}$  (LAST-m) with special m values [7, 19], and MBE (molecular beam epitaxy) grown PbSeTe/PbTe quantum dot (QD) superlattices [101] have been found to give a large  $ZT \sim 2$  in the temperature range (400-800 K). LAST-m gives large ZT values at the higher temperature end.

A different approach to increase ZT by increasing the power factor has been suggested recently by Heremans and collaborators [102] and by Kanatzidis and collaborators[103]. The proposal is to alter the energy dependence of the carrier scattering rate (and consequents the T dependence of  $\sigma$ ) by inserting metallic nanoparticles such as Pb and/or Sb inside bulk PbTe. The precise effect of these nano-particles ( $\sim 30-50$  nm size) on electronic and phononic transport properties are not understood. One of the motivation of the present work is to alter the value of the parameter that controls the energy dependence of the effective scattering time (rather than individual scattering processes) and see how the T-dependence of electronic conductivity changes

From the theoretical side, several calculations of the transport coefficients of PbTe and related systems have been reported over the years [52, 95, 102, 104, 105]. These calculations have been performed using the Boltzmann transport equation within the energy-dependent relaxation time approximation and the nonparabolic Kane model [133] for the energy dispersion  $\varepsilon_{\vec{k}}$  vs  $\vec{k}$ . The energy and temperature dependence of different scattering mechanisms were incorporated in these calculations. Depending on the temperature, different scattering mechanisms (from impurities, acoustic and optical phonons) contributed to the relaxation time  $\tau$ . At high temperatures when optical phonons

dominate the scattering mechanism, it was found that both polar and deformation couplings with optical phonons played equally important role. [106, 107] Earlier work by Bhandari and Rowe [104] focused on the electronic thermal conductivity  $\kappa_{el,J}$ ; they indicated that the inclusion of non-parabolicity in energy dispersion had a pronounced effect on  $\kappa_{el,J}$  and neglecting it would overestimate  $\kappa_{el,J}$ . Also they pointed out that acoustic phonon scattering was the dominant carrier scattering mechanism in PbTe at room temperature (RT). In a later work, Bilc et al [52] work focused on the power factor at high temperatures, and showed that the strength of the deformation coupling constant had to be reduced by about 30% from its earlier value (used in fitting to the room temperature data) to get a better quantitative fit to the high T transport data. All these earlier work did not explore the relationship between the energy and temperature dependence of the effective relaxation rate and the T-dependence of  $\sigma$ ,  $\kappa_{el,J}$  and  $\kappa_{el,E}$  . Also a careful analysis of the difference between these two different electronic conductivities and its impact on the Wiedemann Franz (WF) law in doped PbTe was not made. In this thesis we address these issues by focusing on (1) a careful analysis of the energy and T dependence of  $\tau$  to develop a simple scaling form, (2) understanding the relation between the energy dependence of  $\tau$  and the T dependence of  $\sigma$ , S, and the power factor  $(\sigma S^2)$ , and (3) finding out the difference between electronic thermal conductivity at constant  $\vec{E}$  and at constant  $\vec{J}$  and reexamine the validity of WF law  $\kappa_{el} \equiv \kappa_{el,E} = L_0 \sigma T$ , where the Lorentz number  $L_0 = 2.45 \times 10^{-8} \ W\Omega/K$ . The last point is quite important because in many papers in the current literature the WF law is used to obtain  $\kappa_{el}$  and subtracting it from  $\kappa_{tot}$ , one gets  $\kappa_{l}$ . This method gives unusually small values of  $\kappa_l$  ( $\ll 1~{\rm WK}^{-1}{\rm m}^{-1}$ ). One of the motivations behind this reexamination of WF

using realistic scattering models for PbTe is to check whether these ultra low values of  $\kappa_l$  are reasonable.

# Chapter 2

## **Defects in Semiconductors**

### 2.1 Point Defects

Point defects can be either intrinsic, that is, atoms of the same type as the host crystal but in a wrong position, or extrinsic, that is, atoms of a different type than those of the ideal crystal. The most common intrinsic point defects are the vacancy (a missing atom from a crystalline site) and interstitial (an atom in a non-crystalline site). The most common extrinsic defects are substitutional impurities, that is, atoms which are foreign to the crystal but are situated at crystalline sites, substituting for a regular crystal atom. The presence of defects often distorts significantly the atomic structure of the crystal in the immediate neighborhood of the defects.

#### 2.1.1 Intrinsic Point Defects

Vacancies are quite common in many crystals, both in close-packed metallic structure, ionic solids and open covalent structure. The creation of a vacancy costs some energy, due to the breaking of bonds, which is called the formation energy  $\epsilon_f^{vac}$ . This is defined as the ground state energy of the crystal containing a vacancy, that is, one atom fewer than the ideal crystal which has N atoms, denoted as  $E_0^{vac}(N-1)$ , plus the energy per atom for an ideal crystal, minus the energy of an equal number of atoms in a perfect crystal (with  $N \to \infty$  for an infinite crystal) [54]:

$$\epsilon_f^{vac} = \lim_{N \to \infty} \left[ \left( E_0^{vac} (N - 1) + \frac{E_0(N)}{N} \right) - E_0(N) \right], \tag{2.1}$$

where  $E_0(N)$  is the ground state energy of a crystal consisting of N atoms at ideal positions. Sometimes instead of using  $(E_0(N)/N)$  in Eq. 2.1, one uses  $e^{iso}$ , the energy of an isolated atom, the difference between these two definitions is the binding energy per atom of the perfect crystal. Vacancies can move in the crystal, jumping from one crystalline site to the next – what actually happens is that an atom jumps from one of the sites surrounding the vacancy, into the vacant site. The concentration of vacancies per site in the crystal at temperature T under equilibrium condition is determined by the vacancy formation energy, and is given by [54]

$$c^{vac}(T) = C \exp(-\epsilon_f^{vac}/k_B T), \qquad (2.2)$$

where  $k_B$  is the Boltzmann constant and C takes account of the appropriate unit. The concentration of defects in a crystal is usually determined by the balance between the entropy gain due to the various ways of arranging the defects in the crystal and the energy cost to introduce each defect.

Interstitial atoms are extra atoms that exist inside the crystal at positions that do not coincide with regular crystalline sites. These defects are common in crystals with open structures since in close-packed crystals there simply is not enough room to accommodate these extra atoms: it costs a large energy to squeeze the extra atom into a close-packed crystal. The energy to create an interstitial, its formation energy  $\epsilon_f^{int}$ , by analogy to the formation energy of the vacancy, is given by [54]

$$\epsilon_f^{int} = \lim_{N \to \infty} \left[ \left( E_0^{int}(N+1) - \frac{E_0(N)}{N} \right) - E_0(N) \right], \tag{2.3}$$

where  $E_0^{int}(N+1)$  is the ground state energy of the solid containing a total of N+1 atoms, N of them at regular crystalline positions (allowing for small relaxation) plus one at the interstitial position. Interstitials in crystals with open structures can also move, undergoing a thermally activated process by which they are displaced from one stable position to another, either through a direct jump, or by exchanging positions with an atom of the host lattice. By analogy to the vacancy, there is a thermal activation energy associated with motion of interstitials, called the interstitial migration energy  $\epsilon_f^{int}$ , and the concentration of interstitials per site in the crystal at temperature T under equilibrium conditions is given by [54]

$$c^{int}(T) = C \exp(-\epsilon_f^{int}/k_B T). \tag{2.4}$$

The presence of intrinsic defects in a crystal has an important consequence: it introduces electronic states in the solid beyond those of the ideal crystal. If the energy of such defect-related states happens to be in the same range of energy as that of states of the perfect crystal, the presence of the defect does not make a big difference to the electronic properties of the solid. However, when the defect states happen to have an energy different than that of the crystal states, for example, in the band gap of semiconductors, or resonant states near the valence band maximum or conduction band minimum, their effect can be significant. To illustrate this point, consider a vacancy in Si: the presence of the vacancy introduces four broken bonds (called "dangling bonds"), the energy of which is in the middle of the band gap, that is, outside the range of energy that corresponds to crystal states. By counting the available electrons, it becomes clear that each dangling bond state is occupied by one electron, since two electrons are required to

form a covalent bond. If the neighbors of the vacant site are not allowed to distort from their crystalline positions, symmetry requires that the four dangling bond states are degenerate in energy, and are each half filled (every electronic level can accommodate two electrons with opposite spin). The actual physical situation is more complex but interesting [54]: the four dangling bonds combine in pairs, forming two bonding and two antibonding combinations. The four electrons end up occupying the two bonding states, leaving the antibonding ones empty. This is achieved by slight distortion in the position of the immediate neighbors of the vacancy, which move in pairs closer to each other as shown in Fig. 2.1. The net effect is to produce a more stable structure, with lower energy and a new band gap between the occupied bonding and unoccupied antibonding states, as illustrated schematically in Fig.2.1. This is called a Jahan-Teller distortion; it is common in defect configurations when the undistorted defect structure corresponds to partially occupied, degenerate electronic states.

#### 2.1.2 Extrinsic Point Defects

The most common type of extrinsic point defect is a substitutional impurity, that is, a foreign atom that takes the place of a regular crystal atom at a crystalline site. A common application of extrinsic point defects is the doping of semiconductor crystals. This is a physical process of crucial importance to the operation of modern electronic devices, so we discuss its basic aspects. The energy of states introduced by the impurities, which is relevant to doping, lies within the band gap of the semiconductor. If the energy of the impurity related states is near the middle of the band gap, these are called "deep" states; if it lies near the band extrema (Valance Band Maximum-VBM- or Conduction Band Minimum-CBM) they are called "shallow" states [54]. If the impurity atom has

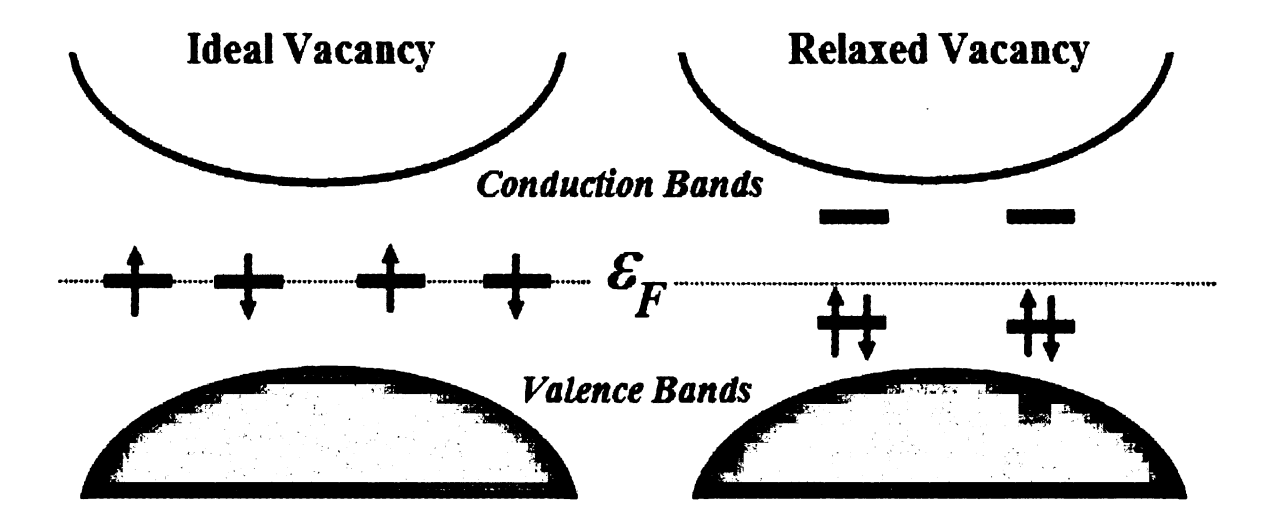


Figure 2.1 Schematic representation of electronic states associated with the Vacancy. The shaded regions represent the conduction and valance states of the bulk. Left: the vacancy configuration before any relaxation of the neighbors: each broken bond contains one electron denoted by an up or a down arrow for the spin states, and all levels are degenerate, coincident with the Fermi level which is indicated by a dashed line. Right: the reconstructed vacancy, with pairs of broken bonds formatting bonding and antibonding states; the former are fully occupied, the latter empty, and the two sets of states are separated by a small gap. [54]

more valence electrons than the host atom, as P impurity in Si, in which case it is called a donor, these extra electrons occupy states near the CBM. At finite T, these electrons get excited to the conduction band and contribute to transport (n-type). In the opposite case, the impurity creates states near the VBM, which is empty at T=0. At finite T it is occupied, which leaves empty states in the VBM of the crystal called "holes"; this type of impurity is called acceptor and the charge carriers are holes (p-type). One important

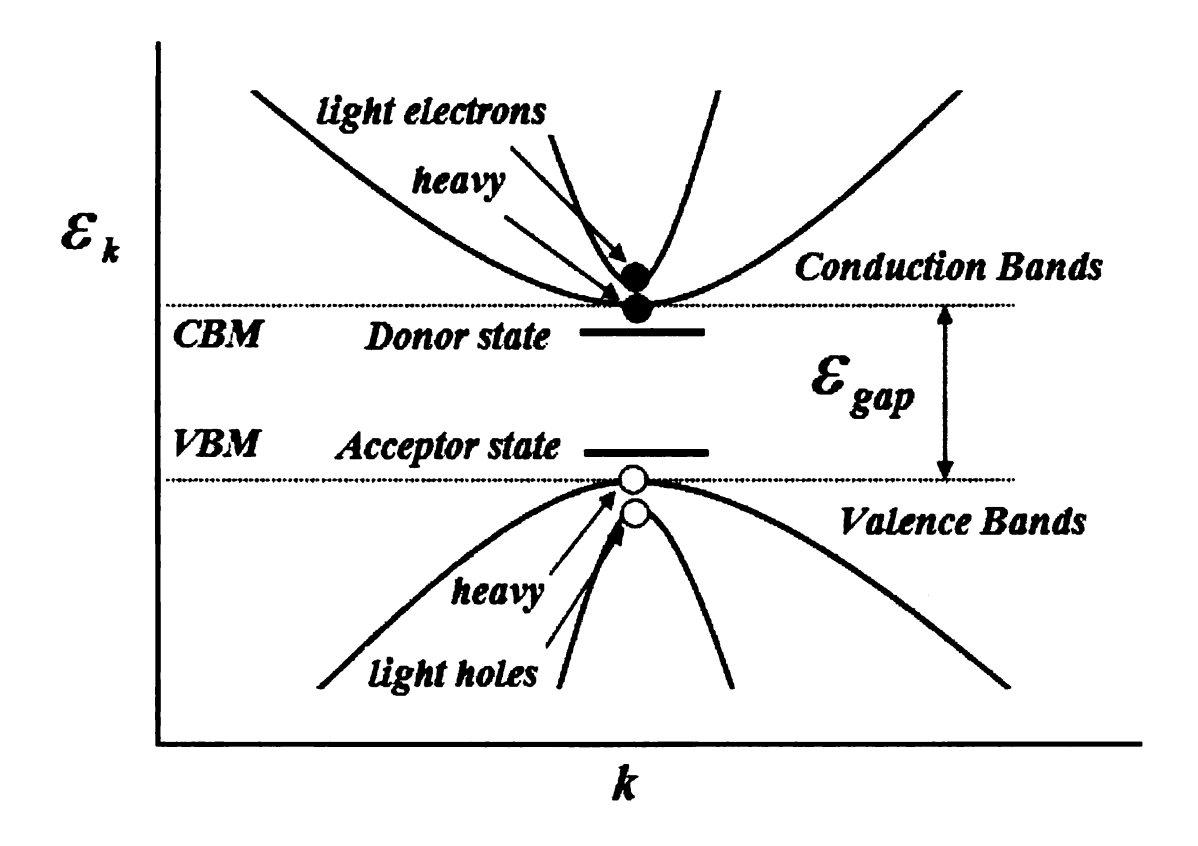


Figure 2.2 Schematic illustration of shallow donor and acceptor impurity states in semiconductor with direct gap. The light and heavy electron and hole states are also indicated; the bands corresponding to the light and heavy masses are split in energy for clarity. [54]

aspect of the impurity related states is the effective mass of charge carriers (extra electrons or holes): due to band-structure effects, these can have an effective mass which is smaller or larger than the bare electron mass, described as "light" or "heavy" electrons or holes, respectively. These features are illustrated in Fig. 2.2. [54]

Electronic transitions between impurity levels through absorption or emission of photons, reveal a signature that is characteristic of, and therefore can uniquely identify, the impurity. Such transitions are often responsible for the color of crystals that otherwise would be transparent. This type of impurity is called a color center.

### 2.2 Evolution of Theory of Defects in Semiconductors

The first device-related problem that required understanding was the creation of electrons or holes by dopants. These (mostly substitutional) impurities are a small perturbation to the perfect crystal and are well described by Effective Mass Theory (EMT) [129]. The Schrödinger equation for the nearly-free charge carrier, trapped very close to a parabolic band edge, is written in hydrogenic form with an effective mass  $(m^*)$ determined by the curvature of the band. The calculated binding energy of the charge carrier is that of a hydrogen atom but reduced by the square of the static dielectric constant of  $\epsilon_0$  of the host material. The binding energy is given by  $[(m^*/m_0\epsilon_0^2)R_{vd}]$ . Typically ( $\epsilon_0 \approx 10$ ) and ( $m^* \sim 0.1 m_0$ ) where  $m_0$  is the free electron mass. As a result, the binding energy ~ meV instead of eV and the associated wavefunction is substantially delocalized, with an effective Bohr radius some 100 times larger than that of the free hydrogen atom. EMT has been refined in a variety of ways [130] and provides a basic understanding of doping in many broad band-gap semiconductors. However, it cannot be applied to defects that have energy eigenvalues far from band edges. These so-called deep state defects are not weak perturbations to the crystal and often involve substantial relaxations and distortions. [69]

The first theoretical tool used to describe the localized defects in semiconductors involved Green's functions.[109-111] These calculations begin with the Hamiltonian  $H_0$  of the perfect crystal. Its eigenvalues give the crystals band structure and the eigenfunctions are Bloch functions. One constructs a set of localized functions (Wannier function's) formed by linear combination of Bloch functions and uses these localized basis to study the defect problem. In principle, the defect-free host crystal is perfectly

described. The localized defect is represented by a Hamiltonian H' which includes the defect potential U. The Green's function of the perturbed crystal is G(E) = 1/(E - H'). The perturbed energies E, in the presence of defect, coincide with its poles. The new eigenvalues include the levels of the defect and the corresponding eigenfunctions are the defect wavefunctions. In principle, Green's functions provide a correct description of a defect in its crystalline environment. In practice, there are many difficulties associated with the construction of perfect-crystal eigenfunctions that can be used as a basis set for the defect calculation, [108] and the construction of the defect potential itself. This is specially true for deep defect states and those defects which induce large lattice relaxations and/or distortions.

The first successful Green's functions calculations for semiconductors date back to the late 1970s. They were used to study charged defects and to calculate forces and total energies. These calculations also provided important clues about the role of native defects in impurity diffusion. However, while Green's functions do provide a near ideal description of a single defect in a perfect crystal, their implementation is difficult and not very intuitive. Alternative methods have been introduced to treat the defect problem; these are cluster and supercell methods. Clusters or supercells are much easier to use and provide a physically and chemically appealing description of the defect and its immediate surroundings. In the cluster approach one takes finite size cluster of the host system and introduces a defect. [131] These types of calculations were performed in real space with basis sets consisting of localized functions such as Gaussians or LCAOs. The dangling bonds on the surface atoms of the cluster must be tied up in some way, most often with H atoms. However, without the underlying crystal and its periodicity, the band structure is

missing and the defect's energy eigenvalues cannot be placed precisely within a gap. Further, the finite size of the cluster artificially confines the wavefunctions. This affects the charged defects the most, as the charge tends to distribute itself on the surface of the cluster. However, the local covalent interactions are well described by the cluster approach. [69]

The Schrödinger equation for a cluster containing a defect can be solved using almost any electronic structure methods. The early work was empirical or semiempirical, with heavily approximated quantum chemical methods. At first, semiempirical extended Hückel theory [113] then self-consistent Hartree-Fock method. Geometries could be optimized, albeit often with symmetry assumptions. The methods suffered from a variety of problems such as cluster size and surface effects, basis set limitations, lack of electron correlation, and the use of adjustable parameters. Their values are normally fitted to atomic or molecular data, and transferability is a big issue.

Substantial progress in the theory of defects in semiconductors occurred in the mid 1980's with the combination of periodic supercells to represent the host crystal, abinitio type pseudopotentials [114] for the core regions, density functional theory (DFT) for the valence regions, and ab-initio molecular dynamics (MD) simulations [115] for nuclear motion. This combination is now referred to as first-principles in contrast to semiempirical. There are a few parameters in the theory. They include the size of the supercell, k-point sampling, type and size of the basis set, chosen by the user, as well as the parameters associated with the basis sets and pseudopotentials. However, these parameters and user inputs are not fitted to an experimental database. Instead, some are determined self-consistently, other are calculated from first principles or obtained from

high-level atomic calculations. For more accurate calculations one uses full potential, all electrons, rather than the pesudupotential. Note that although the first supercell calculations were done in the 1970's in conjunction with approximate electronic structure methods, [116] density functional theory and *ab initio* electronic structure methods using large supercells are just becoming possible.

### 2.3 Density Functional Theory for Defect Calculations

Density-functional theory (DFT) [55, 56] has become the most successful theory for studying atomic-scale computational condensed matter physics and is also widely used to study defects in semiconductors, predict their structures and energetics, vibrational and diffusional dynamics, and elucidate their electronic and optical properties, as observed by various experimental probes. The central quantity in DFT is the electron density. The ground-state total energy is a functional of the electron density and can be obtained via variational minimization of the functional. The wave-mechanical kinetic energy part of the total-energy functional is obtained not from the density directly but through a mapping to a non-interacting Kohn-Sham system.

The basis of electronic structure calculations lies in the nature of electrons in a solid. Electrons interact through long range Coulomb forces which makes it very difficult to describe them as distinct entities. However, the electrons in solids do not act as "bare" particles, rather they are screened out by positively charged polarization clouds. The electron and its screening cloud form a "quasiparticle" which weakly interacts with other quasiparticles in the solid. The effective weak interaction between these quasiparticles allows for an effective single particle approximation, particularly for low energy

properties where they can be treated as acting in the mean field of the other quasiparticles. Such an approximation is valid in a large class of solids (metals, semiconductors, and insulators) but not in solids with strong electron-electron interactions and weak screening (such as magnetic insulators).

### 2.3.1 Density Functional Theory

Because of its great successful in making computational advances in electronic structure of solids, I will briefly discuss the basics of DFT. This theory states that the ground state electronic properties of a solid are determined solely through its electronic density  $\rho(\mathbf{r})$  in terms of which the total energy is:

$$E_{tot}(\rho(\mathbf{r})) = T_s(\rho(\mathbf{r})) + E_{ee}(\rho(\mathbf{r})) + E_{Ne}(\rho(\mathbf{r})) + E_{xc}(\rho(\mathbf{r})) + E_{NN}$$
 (2.5)

where  $T_s$  is the kinetic energy of the noninteracting particles having the same density  $\rho(\mathbf{r})$ ,  $E_{ee}$  is the electron-electron repulsive Coulomb energy,  $E_{Ne}$  is the nuclear-electron attractive Coulomb energy,  $E_{xc}$  is the exchange-correlation energy, and  $E_{NN}$  is the repulsive Coulomb energy of the fixed nuclei.

In the local density approximation (LDA) [61],  $E_{xc}$  is expressed as a function of the local exchange-correlation energy density  $\mu_{xc}$ :

$$E_{xc}^{LDA} = \int \mu_{xc} (\rho(\mathbf{r})) \rho(\mathbf{r}) d^3 \mathbf{r}. \qquad (2.6)$$

This approximation is generalized for both the spin densities  $\rho^{\uparrow}(\mathbf{r})$  and  $\rho^{\downarrow}(\mathbf{r})$  in local spin density approximation (LSDA):

$$E_{xc}^{LSDA} = \int \mu_{xc} \left( \rho^{\dagger}(\mathbf{r}), \, \rho^{\downarrow}(\mathbf{r}) \right) \left[ \rho^{\dagger}(\mathbf{r}) + \rho^{\downarrow}(\mathbf{r}) \right] d^{3}\mathbf{r} \,. \tag{2.7}$$

Recent progress has been made by going beyond LSDA where one adds the gradient terms of the electron density to  $E_{xc}$ . This has led to generalized gradient approximation (GGA)[32, 63]

$$E_{xc}^{GGA} = \int \mu_{xc} \left( \rho^{\dagger}(\mathbf{r}), \nabla \rho^{\dagger}(\mathbf{r}), \rho^{\downarrow}(\mathbf{r}), \nabla \rho^{\downarrow}(\mathbf{r}) \right) \left[ \rho^{\dagger}(\mathbf{r}) + \rho^{\downarrow}(\mathbf{r}) \right] d^{3}\mathbf{r} . \qquad (2.8)$$

To solve the energy minimization problem Kohn and Sham proposed a method in which  $T_s$  is given by:

$$T_s = \sum_{i}^{N} \int \psi_i^*(\mathbf{r}) \left( -\frac{\hbar^2}{2m} \nabla^2 \right) \psi_i(\mathbf{r}) d^3 \mathbf{r}, \qquad (2.9)$$

where  $\psi_i(\mathbf{r})$  are the one-electron orbitals and the sum goes over the all occupied orbitals of an N-electron system. Minimization of the total energy  $E_{tot}$  with respect to charge density  $\rho(\mathbf{r})$  leads to the Kohn-Sham single particle equations:

$$\left[ -\frac{\hbar^2}{2m} \nabla^2 + V_C(\mathbf{r}) + V_{xc} \right] \psi_i(\mathbf{r}) = \epsilon_i \psi_i(\mathbf{r}), \qquad (2.10)$$

where  $V_C$  is the classical Coulomb potential and  $V_{xc}$  is the exchange-correlation potential.  $V_C + V_{xc} = V_{eff}$  is an effective single particle potential. The single particle Kohn-Sham Eqs. 2.10 has to be solved self consistently with the condition:

$$\rho(\mathbf{r}) = \sum_{i}^{N} |\psi_{i}(\mathbf{r})|^{2}. \tag{2.11}$$

It should be emphasized that the total energy  $E_{tot}$ :

$$E_{tot} \neq \sum_{i} \epsilon_{i}^{KS} \quad , \tag{2.12}$$

where  $\epsilon_i^{KS}$  are Khon-Sham single particle eigenvalues; certain corrections have to be made. [67]  $\epsilon_i^{KS}$  are not the true quasiparticle energy states seen in experiment. However, for broad band systems they provide a very good description of the physics except for band gaps and effective masses. [68] Band gaps are usually underestimated.

# 2.3.2 Full Relativistic Single Particle Dirac Equation

For systems containing heavy atoms, such as Pb and Bi, relativistic effects are very important and one should in principle use Dirac theory. In the single particle description, one has to solve the Dirac equation for an electron because the full relativistic effects applied to electronic structure are included in this equation. The Dirac Hamiltonian is given by [57]:

$$H_D = c\alpha. \mathbf{p} + (\beta - 1)mc^2 + V(r),$$
 (2.13)

where  $\alpha$  and  $\beta$  are  $4 \times 4$  matrices expressed as:

$$\alpha = \begin{pmatrix} 0 & \sigma \\ \sigma & 0 \end{pmatrix} \tag{2.14}$$

$$\beta = \begin{pmatrix} 0 & I \\ I & 0 \end{pmatrix} \tag{2.15}$$

with  $\sigma_x$ ,  $\sigma_y$ , and  $\sigma_z$  being the Pauli spin matrices. **p** is the four component momentum, m is the bare electron mass, c is the speed of light and V(r) is the effective single particle potential. The eigen vectors  $\Psi$  of the Dirac Hamiltonian can be written as four component spinors consisting of the two two-component spinors: large component  $\Phi$  and small component  $\chi$ .

$$\Psi = \begin{pmatrix} \Phi \\ \chi \end{pmatrix} \tag{2.16}$$

This gives a set of coupled equations for  $\Phi$  and  $\chi$ :

$$c(\sigma, \mathbf{p})\chi = (\epsilon - V)\Phi \tag{2.17}$$

$$c(\sigma, \mathbf{p})\Phi = (\epsilon - V + 2mc^2)\chi \tag{2.18}$$

Solving for  $\Phi$  the above two equations give the equation for the large component  $\Phi$ :

$$\frac{1}{2m}(\sigma, \mathbf{p}) \left( 1 + \frac{\epsilon - V}{2mc^2} \right)^{-1} (\sigma, \mathbf{p}) \Phi + V \Phi = \epsilon \Phi$$
 (2.19)

The above equation is exact.

#### 2.3.3 Scalar Relativistic Approximation

Eq. 2.19 is the exact Dirac equation. This equation serves as the basis for relativistic electronic structure calculations. [58, 59, 60] However, for valence electrons, where the relativistic effects are not usually strong, one can make the following approximation:

$$\left(1 + \frac{\epsilon - V}{2mc^2}\right)^{-1} \cong \left(1 - \frac{\epsilon - V}{2mc^2}\right) \tag{2.20}$$

and using the identities:

$$\mathbf{p}V = V\mathbf{p} - i\hbar\nabla V \tag{2.21}$$

$$(\sigma. \nabla V)(\sigma. \mathbf{p}) = (\nabla V. \mathbf{p}) + i\sigma. [\nabla, \mathbf{p}] \quad , \tag{2.22}$$

the Dirac Eq. 2.19 can be written as a linear second-order differential equation for  $\Phi$ . This is given by:

$$\left[ \left( 1 - \frac{\epsilon - V}{2mc^2} \right) \frac{\mathbf{p}^2}{2m} + V \right] \Phi - \frac{\hbar^2}{4m^2c^2} (\nabla V \nabla \Phi) + \frac{\hbar^2}{4m^2c^2} (\sigma [\nabla V, \mathbf{p}] \Phi) = \epsilon \Phi. \quad (2.23)$$

For a spherically symmetric potential V(r), Eq. 2.23 can be simplified further:

$$\left[\frac{\mathbf{p}^2}{2m} + V - \frac{\mathbf{p}^4}{8m^3c^2} - \frac{\hbar^2}{4m^2c^2}\frac{dV}{dr}\frac{\partial}{\partial r} + \frac{1}{2m^2c^2}\frac{dV}{dr}\frac{1}{r}(\mathbf{l}.\mathbf{s})\right]\Phi = \epsilon\Phi \quad , \quad (2.24)$$

where the first two terms represent the nonrelativistic Schrödinger Hamiltonian, the third is the mass velocity term, the fourth is the Darwin term, and the last term is the spin-orbit interaction (SOI). In the presence of the SOI term, j=1+s is the good quantum number. The four-component wave function is now written as:

$$\Psi = \begin{pmatrix} \Phi \\ \chi \end{pmatrix} = \begin{pmatrix} g(r)Y_{jl}^{jz} \\ if(r)Y_{jl}^{jz} \end{pmatrix}$$
 (2.25)

where g and f are the radial functions,  $Y_{jl}^{jz}$  is the r-independent eigen function of  $j^2$ ,  $j_z$ ,  $l^2$ , and  $s^2$  formed by the combination of the Pauli spinor with the spherical harmonics.

In practice one first solves Eq. 2.24 without the last term [57], which reduces to:

$$\left[\frac{\mathbf{p}^2}{2m} + V - \frac{\mathbf{p}^4}{8m^3c^2} - \frac{\hbar^2}{4m^2c^2}\frac{dV}{dr}\frac{\partial}{\partial r}\right]\Phi = \epsilon\Phi.$$
 (2.26)

Eq. 2.26 is called the scalar relativistic Schrödinger equation. Since there is no spin-orbit coupling in Eq. 2.26, I and s are individually good quantum numbers. The four-

component wave function  $\widetilde{\Psi}$  can be expressed in terms of radial functions  $(\widetilde{f}(r))$  and  $\widetilde{g}(r)$  and spherical harmonics,  $Y_{lm}$  as:

$$\widetilde{\Psi} = \begin{pmatrix} \widetilde{\Phi} \\ \widetilde{\chi} \end{pmatrix} = \begin{pmatrix} \widetilde{g}(r)Y_{lm} \\ -i\widetilde{f}(r)Y_{lm} \end{pmatrix} \chi_s , \qquad (2.27)$$

where  $\chi_s$  are the two component Pauli spinors  $\binom{1}{0}$ ,  $\binom{0}{1}$ . The scalar relativistic Eq. 2.26 is solved with this choice of  $\widetilde{\Phi}$ . The functions  $\widetilde{\Psi}$  are not eigenfunctions of the Dirac Hamiltonian  $H_D$  and their deviation from eigenfunctions is used to define the spin-orbit Hamiltonian  $H_{so}$ :

$$H_D\widetilde{\Psi} = \epsilon \widetilde{\Psi} + H_{so}\widetilde{\Psi} \,. \tag{2.28}$$

In the basis set of functions  $\tilde{\Phi}$ ,  $H_{so}$  has the form:

$$H_{so} = \frac{\hbar}{2Mc^2} \frac{dV}{dr} \frac{1}{r} \begin{pmatrix} l.s & 0\\ 0 & 0 \end{pmatrix}$$
 (2.29)

where M is the relativistic mass given by:

$$M = m - \frac{\epsilon - V}{2c^2} \,. \tag{2.30}$$

Spin-orbit interaction (SOI) effects are important, especially for heavier elements. To include SOI, one method is to double the entire basis set obtained while solving Eq. 2.26 to accommodate  $H_{so}$ . This approach is usually computationally expensive. The second variational method is an alternative approach, which does not require the doubling of the entire basis set. The spin up and down states are considered separately using the eigenvectors of the scalar relativistic calculation for only a finite number of states near

the Fermi energy. This reduces the number of basis sets involved in the calculation in the presence of SOI. The spin up and down states can be expressed as:

$$\widetilde{\Psi}^{\dagger} = \begin{pmatrix} \widetilde{g}^{\dagger}(r)Y_{lm} \\ -i\widetilde{f}^{\dagger}(r)Y_{lm} \end{pmatrix} \chi_{\uparrow} \qquad , \quad \chi_{\uparrow} = \begin{pmatrix} 1 \\ 0 \end{pmatrix}$$
 (2.31)

$$\widetilde{\Psi}^{\downarrow} = \begin{pmatrix} \widetilde{g}^{\downarrow}(r)Y_{lm} \\ -i\widetilde{f}^{\downarrow}(r)Y_{lm} \end{pmatrix} \chi_{\downarrow} \qquad , \quad \chi_{\downarrow} = \begin{pmatrix} 0 \\ 1 \end{pmatrix}$$
 (2.32)

The states given in Eq. 2.31, and 2.32 are used as new basis set for the expansion of the wave function  $\Phi$  in Eq. 2.24. The total Hamiltonian including SOI can be solved with less computational effort since the number of  $\widetilde{\Psi}^{\uparrow}$  and  $\widetilde{\Psi}^{\downarrow}$  states are usually much less than in the original eigenvalue problem. [20, 57]

#### 2.3.4 Method of calculations

Electronic structure calculations were performed using the self-consistent full-potential linearized augmented plane wave methods (FLAPW) [20] within DFT [31, 55], using GGA of Perdew, Burke and Ernzerhof [32] for the exchange and correlation potential. Since the method and the approximations are very well discussed in the literature, I will not discuss them here. As most of the systems of our interest contain the heavy atom (Pb) relativistic effects are very important. Relativistic effects are marginally important for Te, and not important for Se and Sn. The way these effects are included in the electronic structure code used to obtain the electronic structure (WIEN2K program) [37] is discussed very briefly below.

The core states are treated in a fully relativistic way (i.e solving the Dirac Eq.2.19).[76] The valence and local orbitals, which are defined within the atomic spheres are first obtained within the scalar relativistic approximation (see section 2.2.4). This

approximation does not include SOI but takes into account the effects of mass-velocity and Darwin corrections.[76] In the absence of SOI spin up and spin down eigen functions separate. In the presence of SOI, the spin up and spin down eigen functions mix and this is incorporated in a rather efficient way using a second variational method.[77, 78]

The linearized augmented plane wave (LAPW) method [37] which was used in most of my studies, is among the most accurate methods for performing electronic structure calculations for crystals. Before we describe the LAPW method it is helpful to discuss the augmented plane wave (APW) method first. In the region far away from the nuclei, the electrons are more or less 'free'. Free electrons are described by plane waves. Close to the nuclei, the electrons behave as if they were in a free atom, and they could be described more efficiently by atomic like functions. Space is therefore divided now in two regions: around each atom a sphere with radius  $R_{\alpha}$  is drawn (call it  $S_{\alpha}$ ). Such a sphere is often called a muffin tin sphere and the part of space occupied by the spheres is called the muffin tin region. The remaining space outside the spheres is called the interstitial region (call it I), see Fig. 2.3. One augmented plane wave (APW) used in the expansion of  $\psi_{\vec{k}}^n$  is defined as [37]:

$$\phi_{K}^{\vec{k}}(\vec{r}) = \begin{cases} \frac{1}{\sqrt{V}} e^{i(\vec{k}+\vec{K})\cdot\vec{r}} & \vec{r} \in I \\ \sum_{l,m} \left( A_{lm}^{\alpha,\vec{k}+\vec{K}} u_{l}^{\alpha}(r',E) \right) Y_{m}^{l}(\hat{r}') & \vec{r} \in S_{\alpha} \end{cases}$$
(2.33)

where  $\vec{K}$  are the reciprocal lattice vectors of the plane wave expansion,  $\vec{k}$  are wave vectors within the first Brillouin zone, V is the volume of the unit cell,  $Y_m^l(\hat{r}')$  are spherical harmonic functions referred to the center of the sphere located at  $\vec{R}_{\alpha}$ ,  $u_l^{\alpha}(r', E)$  are the regular solutions of the radial Schrödinger equation for energy E, and  $A_{lm}^{\alpha, \vec{k} + \vec{k}}$  are

the expansion coefficients that are determined by the matching and normalizing conditions for the wavefunction.

The problem with the APW method is that  $u_l^{\alpha}(r', E)$  has to be constructed at the yet unknown eigen energy  $E = \varepsilon_{\vec{k}}^n$  of the searched eigenstate. It would be helpful if we were able to recover  $u_l^{\alpha}(r', \varepsilon_{\vec{k}}^n)$  on the fly from known quantities. That is exactly what the *Linearized Augmented Plane Wave* method enables us to do. If we calculate  $u_l^{\alpha}$  at some energy  $E_0$  then we can make a Taylor expansion for energies not far away from it [37]:

$$u_l^{\alpha}(r', \varepsilon_{\vec{k}}^n) = u_l^{\alpha}(r', E_0) + (E_0 - \varepsilon_{\vec{k}}^n) \underbrace{\frac{\partial u_l^{\alpha}(r', E)}{\partial E}}_{\underline{u_l^{\alpha}(r', E_0)}} + O(E_0 - \varepsilon_{\vec{k}}^n)^2 (2.34)$$

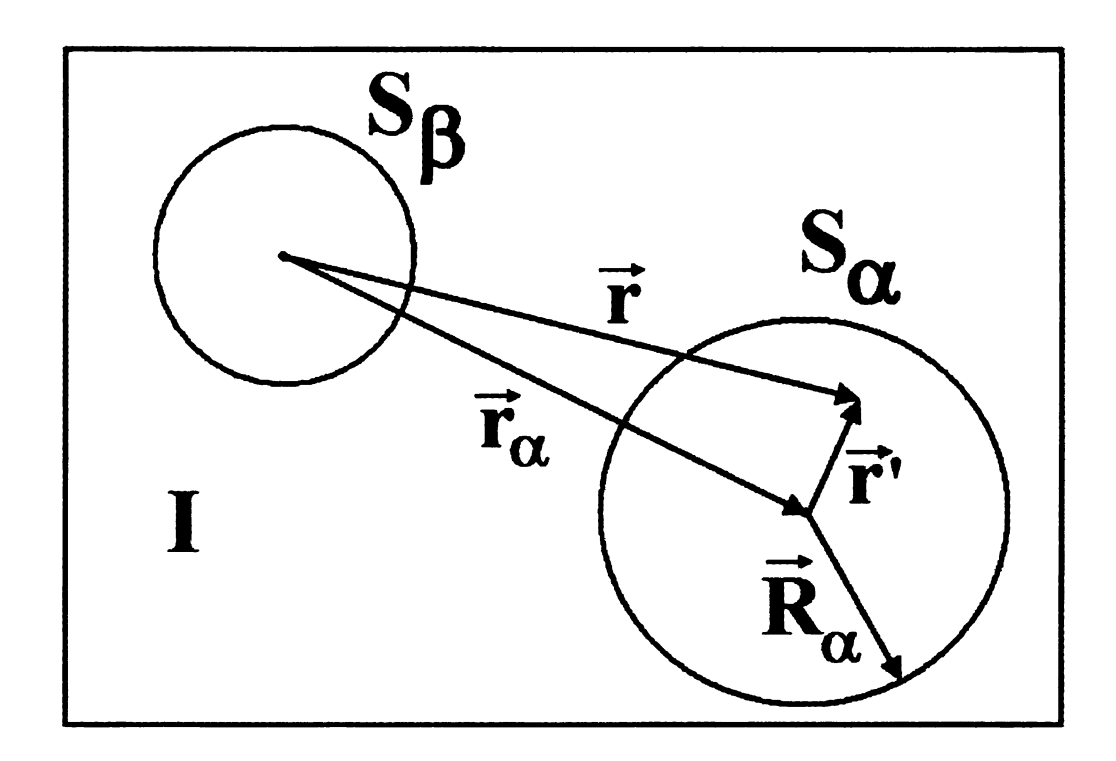


Figure 2.3 Division of a unit cell in *muffin tin* regions and the interstitial region, for a case with two atoms. The black dot is the origin of the axis system.

Substituting the first two terms of the expansion in the APW for a fixed  $E_0$ , gives the definition of an LAPW. This has a price: the energy difference  $\left(E_0 - \varepsilon_{\vec{k}}^n\right)$  is unknown, and hence a yet undetermined  $B_{lm}^{\alpha, \vec{k} + \vec{k}}$  has to be introduced [37]:

$$\phi_{K}^{\vec{k}}(\vec{r}) = \begin{cases} \frac{1}{\sqrt{V}} e^{i(\vec{k} + \vec{K}).\vec{r}} & \vec{r} \in I \\ \sum_{l,m} \left( A_{lm}^{\alpha, \vec{k} + \vec{K}} u_{l}^{\alpha}(r', E_{0}) + B_{lm}^{\alpha, \vec{k} + \vec{K}} \dot{u}_{l}^{\alpha}(r', E_{0}) \right) Y_{m}^{l}(\hat{r}') & \vec{r} \in S_{\alpha} \end{cases}$$
(2.35)

In order to determine both  $A_{lm}^{\alpha,\vec{k}+\vec{k}}$  and  $B_{lm}^{\alpha,\vec{k}+\vec{k}}$ , one requires that the function in the sphere matches the plane wave both in value and in slope at the sphere boundary.

An important parameter that goes into the electronic structure calculation in the LAPW method is the value of the atomic radius of each component. For multi-component systems the values of the atomic radii are chosen differently. In some cases the values of atomic radii are taken to be the same for all the atoms, and this value is chosen to fill the space between the atoms. In other cases different values are chosen for different atoms. The number of  $\vec{k}$  points used in the calculations of the self-consistent charge density is usually taken to be in the range 18 to 30, which corresponds to 400-600  $\vec{k}$  points in the Brillioun zone for cubic systems. The number of plane waves used in the interstitial region is characterized by a parameter  $RK_{max} = R_{ml}K_{max}$ , where  $R_{ml}$  is the smallest muffin tin radius and  $K_{max}$  is the maximum plane wave vector. Typically  $RK_{max}$  is chosen between 7 and 9, and for our calculations it was taken to be 8. Convergence of the self-consistent iterations are usually performed within 0.0001 Ry with cutoff -6.0 Ry between the valance and core states.

# 2.4 Supercell Method

A common approach to calculate defect energetics from first principles (i.e., starting from electronic degrees of freedom) is based on the supercell idea. In this method one confines the atoms defining the defect area of interest into an otherwise arbitrary box, which is then repeated infinitely in one or more spatial directions (see Fig.2.4). In other words, this box (the supercell) now becomes the new unit cell of the system, and periodic boundary conditions are applied at one or more of its boundaries. For a point-defect assembly in a three-dimensional solid, the system now becomes a three-dimensional periodic defect array. For a line defect (e.g., a dislocation) the result is a regular line-defect network. For a surface, the system becomes a sandwich of material slabs interlaced by vacuum regions. Typical sizes of the supercell in all electron calculations are nowadays 64 atoms or larger in a cubic system, and the increasing computational power has enabled supercells with hundreds of atoms. [69]

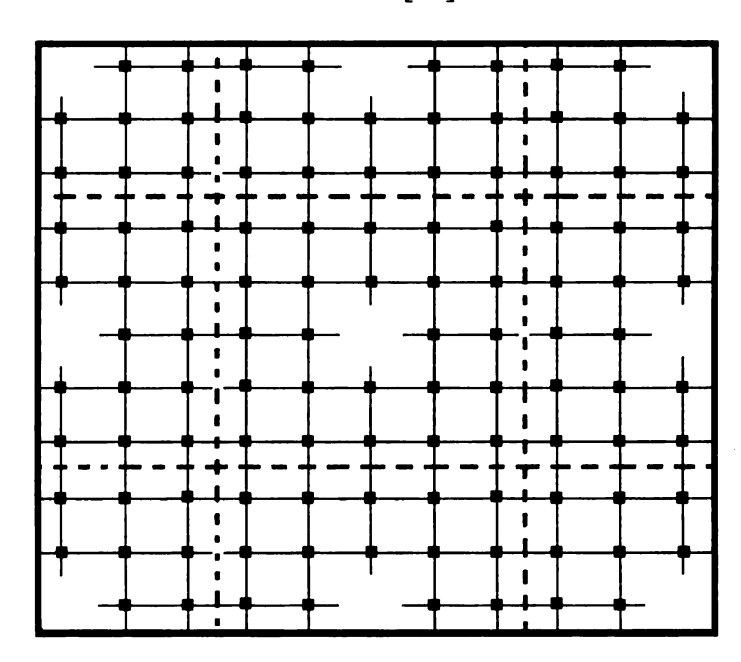


Figure 2.4 Schematic presentation of the supercell construction of lattice vacancy in a solid.

The great advantage of supercell calculations is that the periodic boundary conditions allow the utilization of many efficient techniques derived for the quantum physics of periodic systems. The wavevectors of the Brillouin zone (BZ) in the reciprocal space of the supercell are good quantum numbers, and the standard "band-structure methods" of periodic solids can be applied in full force. Particularly fast computation methods can be performed by using Fourier analysis (plane-wave basis sets), as they adopt naturally to periodic boundary conditions and offer spatially uniform resolution.

The supercell approach enables the full relaxation of the structure to minimize total energy, and the calculation of the formation and migration energies of defects in different charge states as a function of the Fermi-level position of the host semiconductor, and as a function of the chemical potentials of the atoms building up the material. Thus, the method can be conveniently adapted to describe such effects as host materials stoichiometry on the energetics of isolated defects in compound semiconductors [75]. From supercell calculations one can extract several useful physical properties, such as:

(1) the probabilities of certain types of defect to form under given chemical and thermodynamical conditions during the growth, (2) the basic nature (acceptor, donor, deep level) of the defect electronic states, (3) the migration and recombination barriers, (4) vibrational modes, hyperfine fields, positron-annihilation parameters and other ground state properties, and (5) within certain limitations, excited-state (for example optical) properties as well. The ground state properties are those most reliably accessible.

# 2.5 Issues with the Supercell Method in Defects Studies

The obvious drawback of the supercell methods for defect calculations is that the periodicity is artificial and can lead to spurious interactions between the defects. They have a finite density, and do not necessarily mimic the true physical situation with an aperiodic, very low density defect distribution. The supercell method, widely used and with demonstrated success in defect studies, requires a critical examination of the finite-size and periodicity effects.

The first consequence of the finite-size supercell approximation is the *broadening* of the defect-induced electronic levels to "defect bands", with a bandwidth of the order of 0.1 eV for 64-atom supercells. This translates into a difficulty in accurately placing the ionization levels. The one-electron Kohn-sham states associated with the defect are often assigned a position by averaging over the supercell Brillouin zone, or just values at the Brillouin zone origin ( the  $\Gamma$  point) as they exhibit the full symmetry of the defect. The defect-state dispersion usually has a smaller effect on the total energies that include summations and integrations of the Kohn-Sham states over the entire Brillouin zone. Thus, ionization levels determined from the total-energy differences is expected to be less sensitive to the defect-band dispersion. However, this is hard to prove systematically.

Another source of difficulty associated with supercell calculations is the accurate determination of the host crystal band edges (valence-band maximum, conduction-band minimum), which are the natural reference energies for the defect-induced gap states. In the defect-containing supercell, the band-edge states themselves are affected by the defect. The band-edge positions are often determined by aligning a chosen reference level between the defect-containing and perfect solid. For example, the effective potential in a

localized region far from the defect can be aligned with the potential in the same region in a perfect crystal. The calculated band-edge distances from the reference energy in a perfect crystal can then be used to align the band edges in the system containing the defect. Alternatively, one can consider a deeper, core-level energy of an atom as a local reference.

Another, more difficult problem arises with charged defects. In order to avoid divergences in electrostatic energies, a popular solution is to introduce a homogeneous neutralizing background charge to the supercell array, which enables the evaluation of electrostatic (Coulomb) energies. This, however, introduces an electrostatic interaction between the periodic charge distribution in the supercells and the background, which vanishes only in the limit of infinitely large supercells. The influence of their fictitious charge has to be subtracted in the end, and this is a highly nontrivial task.

Point defects induce lattice relaxation in the host lattice. The lattice-relaxation pattern is restrained by the supercell geometry. The argument, often used in supercell calculations, is that the ion displacement vanish near the borders of the supercell. However, this does not necessarily guarantee that the long-range ionic relaxations are correctly described, as the supercell symmetry itself may fix the positions of the boundary atoms. According to elastic continuum theory, the strain field at large distances from the point defect fall of as  $|r|^{-3}$  and the ionic displacements falls off as  $|r|^{-2}$ . The finite size of the supercell thus restricts also the ionic relaxations around the defect. The relaxation pattern is truncated midway between a defect and its nearest periodic replica. In the case of long-range relaxations this cutoff may be reflected dramatically close to the

defect, as was demonstrated by Puska et al. [79] by detailed calculations for vacancies in silicon.

Further comparison of the supercell to the finite-cluster and Green's function methods reveals the following. The supercell and Green's function methods have a well-defined electron chemical potential (they are coupled to a reservoir of electrons) where as the cluster method does not. This has consequences for the treatment of ionization levels, which is somewhat problematic for the cluster method. The finite-size effect is there in the cluster method as well, as the clusters can contain spurious surface-related effects. The Green's function method is mathematically elegant and in principle the best for isolated defects, but its computational implementation is difficult in view of the accuracy required for total electronic energies and derived quantities.

Finally, it is important to note that defect and impurity calculations should, as a rule, be carried out using the theoretical lattice constant, optimized for the bulk unit cell. This is crucial in order to avoid spurious elastic interactions with defects or impurities in the neighboring supercells. The purpose is to investigate properties of isolated defects or impurities in a dilute limit. If the volume of the defect-containing supercell is relaxed (in addition to relaxing the positions of the atoms near the defect), the calculation would in fact correspond to finding the lattice parameter of the system containing an ordered array of defects at high concentration. In spite of these limitations, the supercell method has been, extremely successful in predicting physical properties of defects in solids [74, 79], so we are going to use it in this thesis.

# **Electronic Structure of Defects in PbTe**

#### 3.1 General Introduction

A detailed microscopic understanding of the nature of the defect states in PbTe is an old but a challenging problem. Naively, one expects to see bound shallow defect states in the band gap (pinned to the valence band maximum or conduction band minimum) when a Pb or a Te atom is replaced by either a donor- or acceptor-like impurity or by a vacancy. However, it is known that, in narrow band-gap semiconductors like PbTe, one does not see these shallow defect states but deep defect states (DDS) which can be outside the band gap.[11-15]

One of the earlier attempts to understand the origin of deep defect states in PbTe was made by Lent et al.[13] For substitutional defects in PbTe, they presented a simple chemical theory for a large class of substitutional defects and vacancies in terms of the atomic energy levels and tight binding concepts. Unfortunately, these calculations did not take into account the potentials generated by the impurities in a self-consistent manner and, therefore, were only qualitative in their prediction. In fact, an even earlier attempt to understand the origin of vacancy-induced deep defect states in PbTe was made by Parada and Pratt.[14] They used a Slater-Koster model [110] and Wannier function basis constructed out of a finite number of PbTe bands. For Pb vacancies, they predicted defect

states outside the band gap and were able to explain the low temperature *n*- and *p*-type transport properties in nominally pure PbTe. The defect potential used in the Slater-Koster model was assumed to be a constant and was not calculated self-consistently. Therefore the precise positions of the defect states predicted by this calculation are not expected to be quantitatively reliable. The other major efforts in understanding the physics of deep defect states are for In-doped PbTe. Inhomogeneous mixed-valence models for In and other group III impurities (like Ga and Tl) have been proposed to explain several experimental data.[17] In these models, In impurities are assumed to exist in two valence states, one trivalent and the other monovalent, stabilized by strong electronic and ionic relaxations. My recent calculations have cast some doubts on the validity of this model.[18]

In this Chapter, I discuss the results of my calculations to understand the physics behind the formation of deep defect states in PbTe using self-consistent *ab initio* electronic structure calculations within density functional theory (DFT) and supercell models. Only a few *ab initio* studies in narrow band gap systems (such as PbTe, PbSe, etc.) have been made recently. One is by Bilc *et al.*[19] who have recently reported their results on Ag and Sb substitutional defects in PbTe using all-electron full-potential linearized augmented planewave (FP-LAPW) method.[20] Another is by Ahmad *et al.*[18] who looked at the In impurity problem. Similar calculations have been carried out by Edwards *et al.*[21] who looked at the Ge and Te vacancy and anti-site defects in GeTe. The purpose of my thesis project is to extend the previous studies of the defects in PbTe to different types of defects. The defects studied are: Pb and Te vacancies, Pb substituted by monovalent atoms (Na, K, Rb, Cs, Cu), divalent atoms (s-type Zn, Cd, Hg and p-type

Ge, Sn), or trivalent atoms (group III Ga, In, Tl, and group V As, Sb, Bi), and Te substituted by S, Se, or I. My main focus is to develop a systematic understanding of these defect states as one goes across or down the periodic table to select different impurity atoms. The results of this study have been recently reported.[18, 24, 50] The arrangement of this chapter is as follows. In Sec. 2, I discuss the electronic structure of PbTe. In Sec. 3, I describe the structural model and briefly review the method used to calculate the electronic structure (The details are already given in chapter 2). In Sec. 4, I present my results of calculations for Pb-site defects. In Sec. 5 results on Te-site defects are presented. In Sec. 6, I discuss the impurity-impurity interaction issue and its implications on the dilute defect limit. In Sec. 7, I discuss my theoretical results in the light of recent measurements of thermopower in several PbTe based compounds. Finally, a brief summary is given in Sec. 8.

#### 3.2 Electronic Structure of PbTe

The rock-salt structure semiconductors PbS, PbSe and PbTe are quite interesting, they show a series of electronic anomalies relative to the usual II-VI semiconductors (such as CdTe). For example, the direct gap occurs at the L point and the order of the band gap and valence band maximum energies in going from S to Te are anomalous  $(E_g[PbS] = 0.29 \text{ eV}, E_g[PbSe] = 0.17 \text{ eV}, E_g[PbTe] = 0.19 \text{ eV}$ , at T = 0K) [30]. The band gap pressure coefficient is also anomalous, it is negative. Because of these peculiarities and their practical applications, there have been many electronic structure calculations in these compounds [25, 26, 27, 28, 29, 30]. Wei and Zunger [28] have carried out extensive electronic structure calculations using local density approximation

(LDA) [31] as implemented through the linearized augmented plane-wave (LAPW) method [20]. They have argued that the above anomalous features can be ascribed to the presence of the Pb s-band below the top of the valance band, setting up coupling and level repulsion at the L point of the face centered cubic (fcc) Brillouin zone (Fig. 3.1). Albanesi et al [29] have calculated the frequency dependent dielectric constant of PbSe and PbTe using the electronic structure (obtained with LAPW) within both LDA and generalized gradient approximation (GGA) [32]. They found a large dielectric constant for PbTe in agreement with experiment. [33, 34]. Bilc et al have carried out extensive all electron LAPW calculations within both LDA and GGA. The band structure results show that PbTe has a direct band gap at the L point, but with a small gap value of ~ 0.09 eV at the experimental volume  $V_{exp}$  [23]. The volume optimization increases the gap to  $\sim 0.19$ eV in much better agreement with experiment. The GGA (LDA) optimal volume Vopt correspond to 5% increase (decrease). The Orbital analysis shows that Te and Pb p states strongly hybridize, suggesting covalent interaction between these two atoms. They have also computed the ionicity of Pb and Te atoms according to Bader's "Atoms in Molecules" theory [35]. The results show an ionic state of Pb<sup>+0.64</sup>Te<sup>-0.64</sup> which is much smaller than that of the pure ionic model Pb<sup>+2</sup>Te<sup>-2</sup>. Therefore in PbTe covalent interactions play an important role. The reduction in formal charges from 2(-2) to 0.64 (-0.64) is consistent with the large dielectric constant of PbTe.

# 3.3 Supercell Model to Calculate Defect Structure

Before we discuss the structural model used to study the impurity states, we would like to briefly describe the quaternary systems one constructs in developing

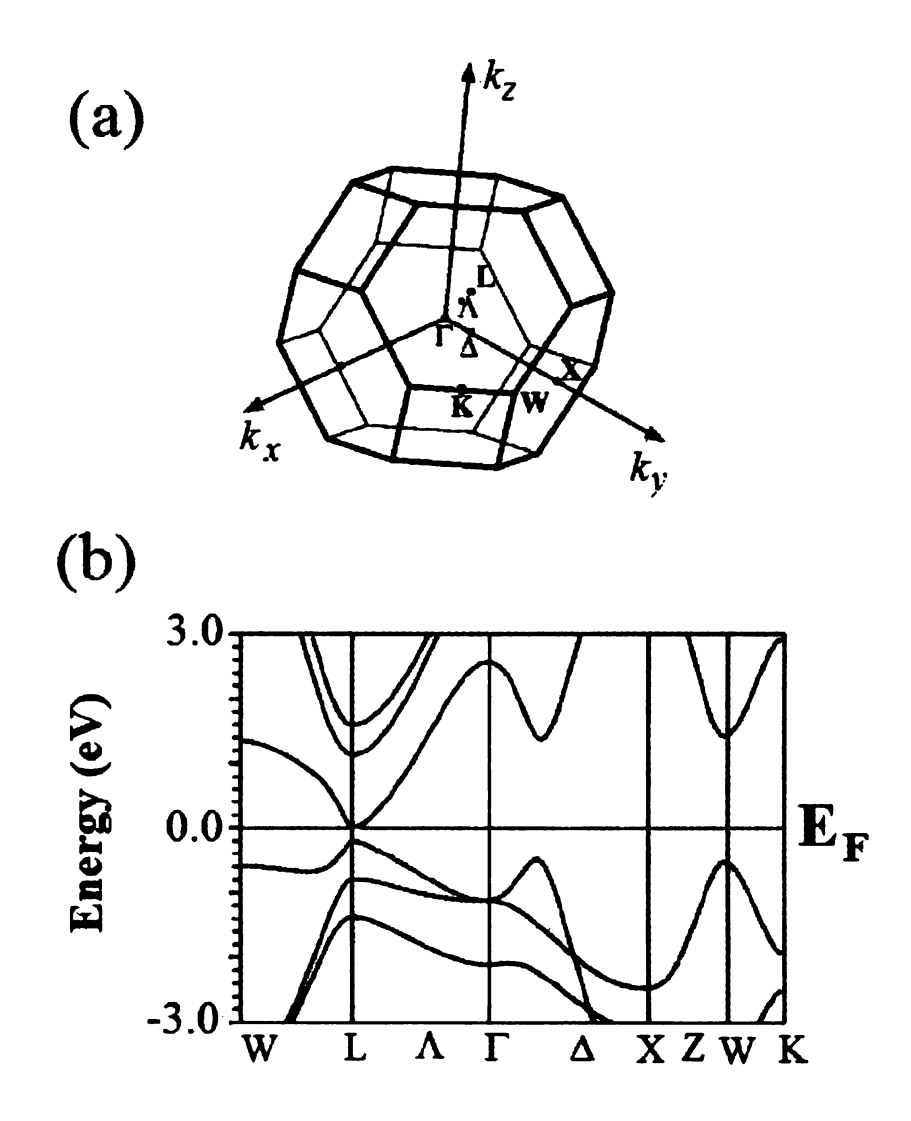


Figure 3.1 (a) fcc Brillouin zone of PbTe (b) Band structure of PbTe in fcc Brillouin zone at  $V_{opt}$ . [23]

thermoelectrics starting from the binary compound PbTe and replacing Pb atoms by other atoms. The new compounds are described by the formula  $RR'Pb_{2n-2}Te_{2n}$ , where R and R' are chosen to maintain charge neutrality. Here two divalent Pb atoms are replaced by one monovalent (R) and one trivalent (R') atom. If R is divalent then R' is also divalent (for example R=R'=Cd). The material is therefore charge compensated and most likely will maintain its semiconducting character. One then adjusts the concentrations of R and R' to

control the sign of the charge carriers. In a recent work, Bilc *et al.* [19] have discussed the electronic structures of a series of charge compensated AgSbPb<sub>2n-2</sub>Te<sub>2n</sub> compounds (n=6, 9, 16) and also charge uncompensated compounds AgPb<sub>2n-1</sub>Te<sub>2n</sub>, SbPb<sub>2n-1</sub>Te<sub>2n</sub> (n=16) where only one of the elements R or R' is present. They found resonant states overlapping conduction and valence bands caused by Sb and Ag impurities, respectively. In this chapter, we extend their results to a large class of defects, but focus on defects of one type (either R or R'), investigating the electronic structure of  $RPb_{2n-1}Te_{2n}$ . We also carry out similar calculations in compounds of the type  $MPb_{2n}Te_{2n-1}$ , where M is a defect at the Te site. Our aim is to explore systematically the impurity-induced changes in the electronic DOS as one goes down or across the periodic table.

We use a supercell model where the defects are periodically arranged in a PbTe lattice (see Sec. 2.4). This corresponds to the formula  $RPb_{2n-1}Te_{2n}$  or  $MPb_{2n}Te_{2n-1}$  as mentioned above. To increase the distance between the defects as much as possible (in order to reduce the interaction between them) without increasing the size of the supercell enormously we have chosen n=16. This corresponds to a unit cell containing 64 atoms with the minimum distance between two defects being ~13Å (see Fig. 3.2). Due to the large dielectric constant of the host PbTe, we expect long-range Coulomb effects to be strongly screened, thereby reducing the impurity-impurity interaction. However, short-range interactions are still present. Before describing the details of our calculations we would like to point out that there are some fundamental problems regarding the inadequacy of using the supercell model to calculate the energy of isolated defect states in semiconductors; [36] as discussed in Sec. 2.4. However, they are usually for extended "shallow" impurity states and for charged defects. Since most of the defect states in

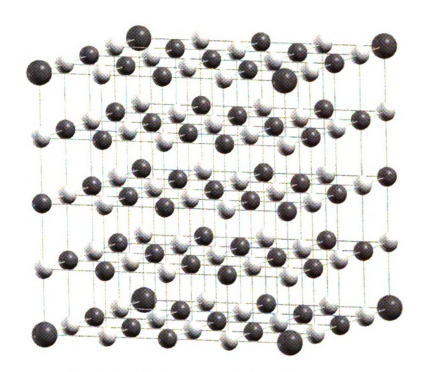


Figure 3.2 Supercell model of  $RPb_{31}Te_{32}$  where R is either a vacancy or an impurity atom. Small balls are for Pb and Te, large balls are for R.

narrow band-gap semiconductors of our interest are of localized "deep" type, we expect the supercell model to be reasonable. We discuss in details the supercell size dependence of the defect states in Sec. 6 of this chapter.

Electronic structure calculations were performed within DFT using all-electron FP-LAPW plus local orbital method [20] incorporated in WIEN2k. [37] We used the generalized-gradient approximation (GGA) [32] for the exchange and correlation potential. Scalar relativistic corrections were included and spin-orbit interaction (SOI) was implemented using a second variational procedure. [38] Convergence of the self-consistent iterations was performed using 20 k-points inside the reduced Brillouin zone to within 0.0001 Ry (1.36 meV) with a cutoff energy of -6.0 Ry separating the valence and the core states. For this initial survey, calculations were performed using the experimental

lattice constant of PbTe, which is 6.454Å, [39] and no relaxation (volume or internal) studies were carried out. For a few systems, we also carried out calculations using the projector augmented wave (PAW) [40] method incorporated in *Vienna Ab-initio Simulation Package* (VASP) [41] to compare with the FP-LAPW results and also to increase the impurities separation by going to larger supercells. The optimal lattice constant of PbTe obtained from volume optimization (which is 6.55 Å) was used in these PAW calculations, and ionic relaxations were performed. I should mention here that choosing between the experimental or optimal lattice constant should not change the basic physics of the impurities states, since the difference between these two values is rather small (~0.096Å).

#### 3.4 Pb-site Defects

Before presenting the results of the *ab initio* electronic structure calculations, we discuss some basic physics of the PbTe system. In this compound Pb and Te 6s and 5s states are quite deep and the conduction and valence bands are formed primarily out of 6p states of Pb and 5p states of Te respictively. The Pb-Te bonds have both covalent and ionic character. The removal of one Pb atom or replacing it by a monovalent cation leads to a local charge disturbance and alters the covalent bonding with the neighboring Te (denoted as Te2) p states. As a result, the valence band states get strongly perturbed. One expects acceptor-like states to appear near the top of the valence band. However, their precise positions can only be obtained after a detailed self-consistent calculation. Also, because of the local nature of the perturbation we expect the entire valence band region to be affected. In the case of the monovalent Ag impurity, one has, in addition, the filled d

states which interact with the Te p states and change the valence band. The Cd impurity, although divalent like Pb, has a 5s state that may give rise to new states near the bottom of the conduction band. Indium (In) and other trivalent sp atoms may also give rise to a bound s state below the valence band and therefore act more like a monovalent impurity than a trivalent one. It is important to emphasize that simple shallow impurity-state models [16] and Slater-Koster type models [110] that do not calculate the impurity potential self-consistently [13-15,17], are not capable of describing the short-range physics of these impurity states quantitatively. Only a careful self-consistent ab initio calculation is able to do so. In this section (3.4) I focus on the cationic site defects. This is because in several experimental systems of our interest, e.g., AgSbPb<sub>2n-2</sub>Te<sub>2n</sub> [7] and Na<sub>0.95</sub>Pb<sub>m</sub>SbTe<sub>m+2</sub>,[8] the Ag, Na and Sb atoms are located on the Pb-cation sites. The removal of one Pb atom (i.e., creation of one vacancy at the Pb site) or replacing it by another atom with different valence structure charge introduces a local charge disturbance and alters the bonding with the neighboring Te p states. Due to the longrange nature of the former and the short-range of the latter, we expect the entire valence and conduction band states to get perturbed in the presence of the impurity. Although anionic vacancies (discussed in Sec. 3.5) have been considered to play a significant role in the transport properties of PbTe, substitutional defects at the anionic sites have been less well-investigated in the past and there are plans for future investigation of these defects.

#### 3.4.1 Pb Vacancy in PbTe

The total DOS of PbTe with and without Pb vacancy and the difference between the two are shown in Fig. 3.3(a)-(c). These were calculated using 20 inequivalent k-points in the cubic Brillouin zone. For the sake of comparison, we shifted (upward) the DOS of PbTe by a small amount (~ 0.2 eV) so that the lower edge of the valence-band DOS of the systems with and without Pb vacancy matched. We found that the first peak below the valence band maximum (VBM) also matched after this shift. This small shift appears to be reasonable since with this shift the Te core 5s bands (not shown in Fig. 3.3) also matched perfectly. As we can see from Fig. 3.3(a)-(c), the entire valence-band and conduction-band DOS get modified by the presence of the Pb vacancy. It is important to note that the states near the bottom of both the valence and conduction band do not change appreciably in the presence of the Pb vacancy. Since transport properties are controlled by the states near the VBM and conduction band minimum (CBM), let us focus on the band gap region within an energy range of  $\pm$  0.5 eV about the center of the band gap. We see that there is very little change near the bottom of the conduction-band DOS whereas there is an increase in the DOS near the top of the valence band. We analyze this increase in more detail below. From Fig. 3.3(a), we can clearly see that the Fermi energy (at 0 eV) cuts through the valence band top and therfore Pb vacancies give rise to holes as expected.

To see which atoms contribute to the change in the DOS near the VBM, we show in Fig. 3.3(b) the difference in the partial DOS between PbTe with and without Pb vacancy. There are six nearest-neighbor Te atoms of the Pb vacancy (denoted as Te2) and

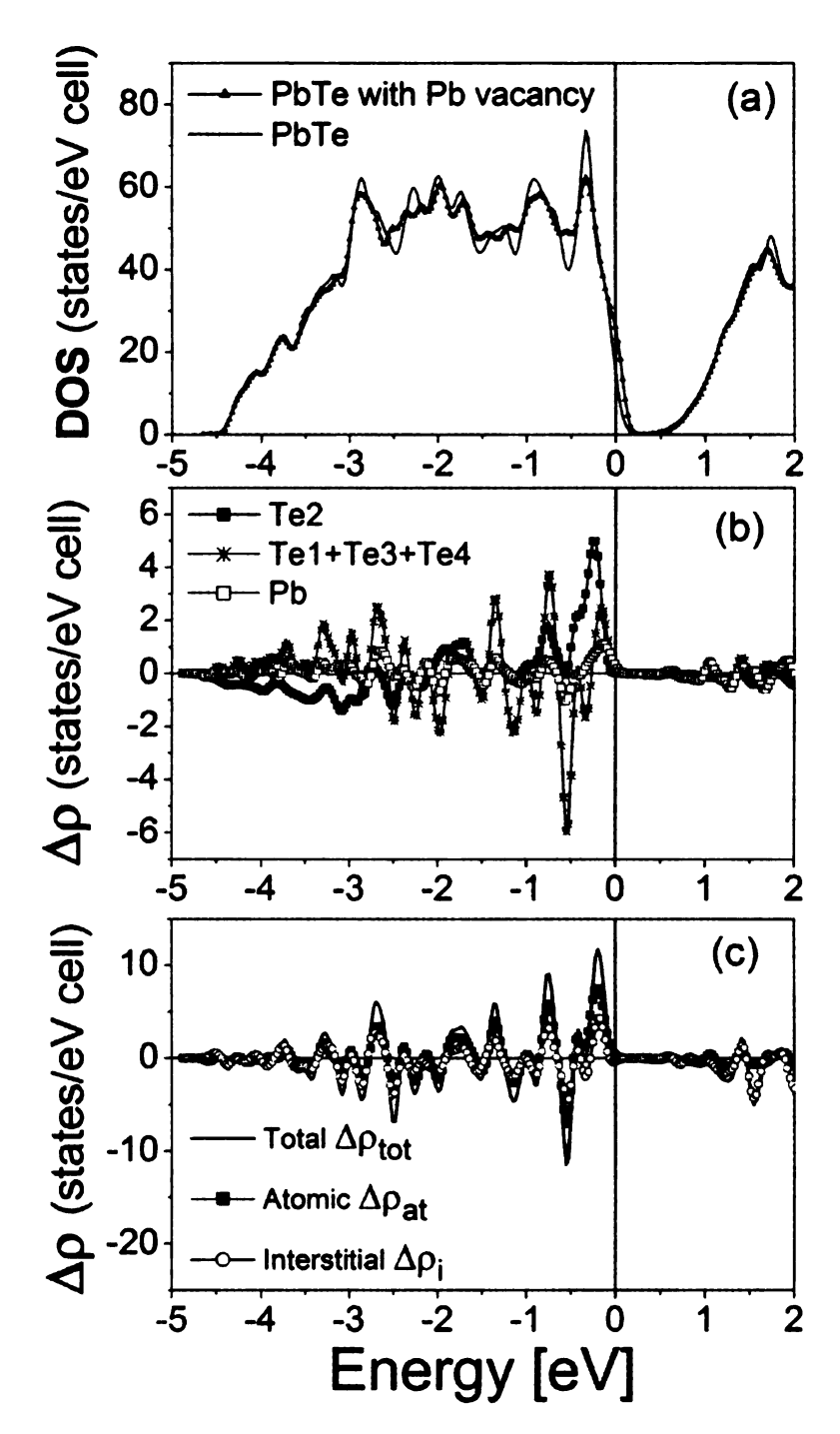


Figure 3.3 (a) The total DOS of PbTe with and without Pb vacancy, (b) the difference in the partial DOS between PbTe with and without Pb vacancy where the six nearest neighbor Te atoms of the Pb vacancy are denoted as Te2 and there are three other inequivalent Te atoms (denoted as Te1, Te3, and Te4), and (c) Atomic spheres ( $\Delta \rho_{at}$ ), and interstitial components  $\Delta \rho_i$  of  $\Delta \rho_{tot}$ . The energy origin in (b) and (c) is chosen to be the top of the valence band of PbTe; whereas the energy origin in (a) is the highest occupied Kohn-Sham single-particle state (which will be denoted as the Fermi energy) of the system with defect.

three other inequivalent Te atoms (denoted as Te1, Te3, and Te4). Among the Pb neighbors of the Pb vacancy, Pb2 is the Pb atom that bridges two Te2 atoms each being the nearest-neighbor of one of the defect sites. In one supercell there are three Pb2 atoms and twenty-eight other Pb atoms. Of the latter, there are four inequivalent (Pb3, Pb4, Pb5, Pb6) lead atoms. Clearly the major contribution to the DOS increase near the top of the valence band comes from the six nearest-neighbor Te2 atoms and we see that Te2 states in the lower half of the valence band get pushed towards the upper half. This transfer of the Te2 DOS is partially compensated by the downward shift of the DOS associated with the other atoms. Also other Te atoms do contribute a small amount to the increased DOS near the VBM.

It should be noted that, in FP-LAPW calculations, there is an appreciable DOS associated with charges outside the atomic spheres, i.e., in the interstitial space (as discussed in chapter 2). [37] In Fig. 3.3(c), we show the difference in the total DOS ( $\Delta \rho_{tot}$ ), DOS associated with the charges inside the atomic spheres ( $\Delta \rho_{at}$ ), and that associated with the interstitial space ( $\Delta \rho_i = \Delta \rho_{tot} - \Delta \rho_{at}$ ).  $\Delta \rho_i$  and  $\Delta \rho_{at}$  have almost the same energy dependence and are comparable in magnitude. We can interpret the peak in  $\Delta \rho_{tot}$  near the top of the valence band [Fig.3.3(c)] as a vacancy-induced resonant state. This should be significant in the hole-doped samples where these states will be involved in charge and energy transport. The fact that Pb2, Te1, Te3, and Te4 contribute very little to  $\Delta \rho_{tot}$  suggests that the vacancy-induced resonant states are well localized and hence weakly interacting with each other.

It is interesting to compare our results with those of Parada and Pratt.[14] They found that the perturbation due to a Pb vacancy was not strong enough to drive any levels

out of the Te p bands. The Pb s state associated with the vacancy site was driven about 3 eV above the bottom of the conduction band, hence of no significance for transport. A doubly degenerate state was driven out of the Te s band but only by about 1 eV, hence it was occupied by two Te s electrons. As a result, a Pb vacancy creates two holes in the Te p valence band and leads to p-type conduction. These findings are supported by our ab initio calculations. However, the subtle effects such as the DOS enhancement near the top of the Te p valence band which can affect the thermopower of holes was not found in this earlier study.

# 3.4.2 Monovalent impurities (Na, K, Rb, Cs, Cu, Ag) in PbTe

Now let us discuss the monovalent impurities. They should provide a weaker perturbation compared to the Pb vacancy because the nominal charge difference is 1. In Fig. 3.4, instead of giving the total DOS, we only show the difference ( $\Delta \rho_{tot}$ ). We find that K, Rb, Cs, Cu and Ag all show peaks near the top of the valence band, just like a vacancy. Na is anomalous, it does not seem to change the DOS near the valence band top, but shows an increase (as compared to other three alkalis) near -3.2 eV. The major difference between Cu, Ag and the alkalis is seen near the bottom of the valence band in the energy range (-2, -1) eV for Cu and (-4, -3) eV for Ag. This is due to the Cu and Ag d states hybridizing with the Te p bands. We will further discuss these results later in Sec. IV when we compare our theoretical results with experiment. We find that the valence s state of the alkalis are all above the valence band, hence all of them donate one electron to the system. In contrast to the suggestions made in Ref.13, we find that Cs behaves just like Na in this respect. We should note that even if the alkali atoms donate one electron.

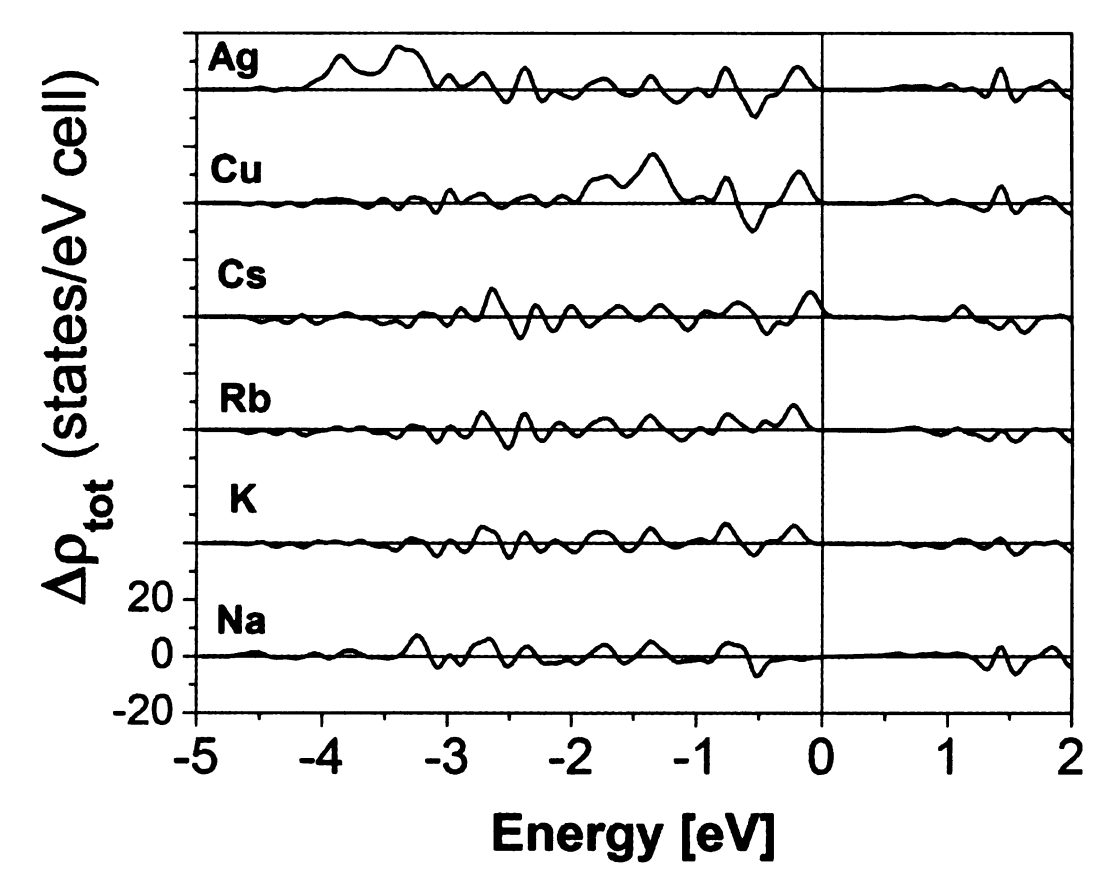


Figure 3.4 The difference in the total DOS ( $\Delta \rho_{tot}$ ) between PbTe with and without monovalent impurities: Na, K, Rb, Cs, Cu, and Ag. The energy origin (0 eV) is chosen to be at the top of the valence band of PbTe.

when they replace Pb (which is divalent), they give rise to one hole per impurity and should behave like accepter under ideal conditions.

# 3.4.3 Divalent impurity (Zn, Cd, Hg, Sn, Ge) in PbTe

There are two types of divalent impurities: s-type (Zn, Cd, and Hg) and p-type (Sn and Ge). The valence configurations of the s-type impurities are  $4s^2$  (Zn),  $5s^2$  (Cd) and  $6s^2$  (Hg); whereas those for the p-types are  $4p^2$  (Sn) and  $5p^2$  (Ge). The valence state of divalent Pb is of course  $6p^2$ . Our result for Zn, Cd and Hg are given in Fig. 3.5 and 3.6. We find that the s-type impurities introduce resonant states near the bottom of the PbTe conduction band and there are three major changes in the DOS: (i) an enhancement of the DOS near the bottom of the conduction band caused by a resonant state, (ii) a reduction in the DOS near the top of the valence band within an energy range ~0.25 eV, and (iii) an enhancement of the DOS near the bottom of the valence band [see Fig. 3.5 and Fig. 3.6(a)-(d)]. These three changes can be seen clearly if, for example, one looks at the Cd s character in Fig. 3.6(d). The Cd atom introduces an s-like state into the system. This state strongly hybridizes with the p orbitals of the six neighboring Te2 atoms and the bonding state appears at about -4 eV [see Fig. 3.6(c) and 3.6(d)]. The corresponding anti-bonding state appears as a resonant state near the conduction band bottom, reflecting the deep defect nature of these impurity states. The states near the top of the valence band (antibonding between Pb and Te2 p's) are depressed when Pb is replaced by Cd. Because of the resonant state near the bottom of the conduction band, we expect electron-doped Cd systems to exhibit large thermopower. Its experimental implication will be discussed later. In contrast to the s-type divalent impurities, the p-type impurities, Sn and Ge, do not alter the DOS near the band gap (see Fig. 3.7). They behave very much like Pb near the band gap region, which is understandable since Pb is also a p-type divalent atom.

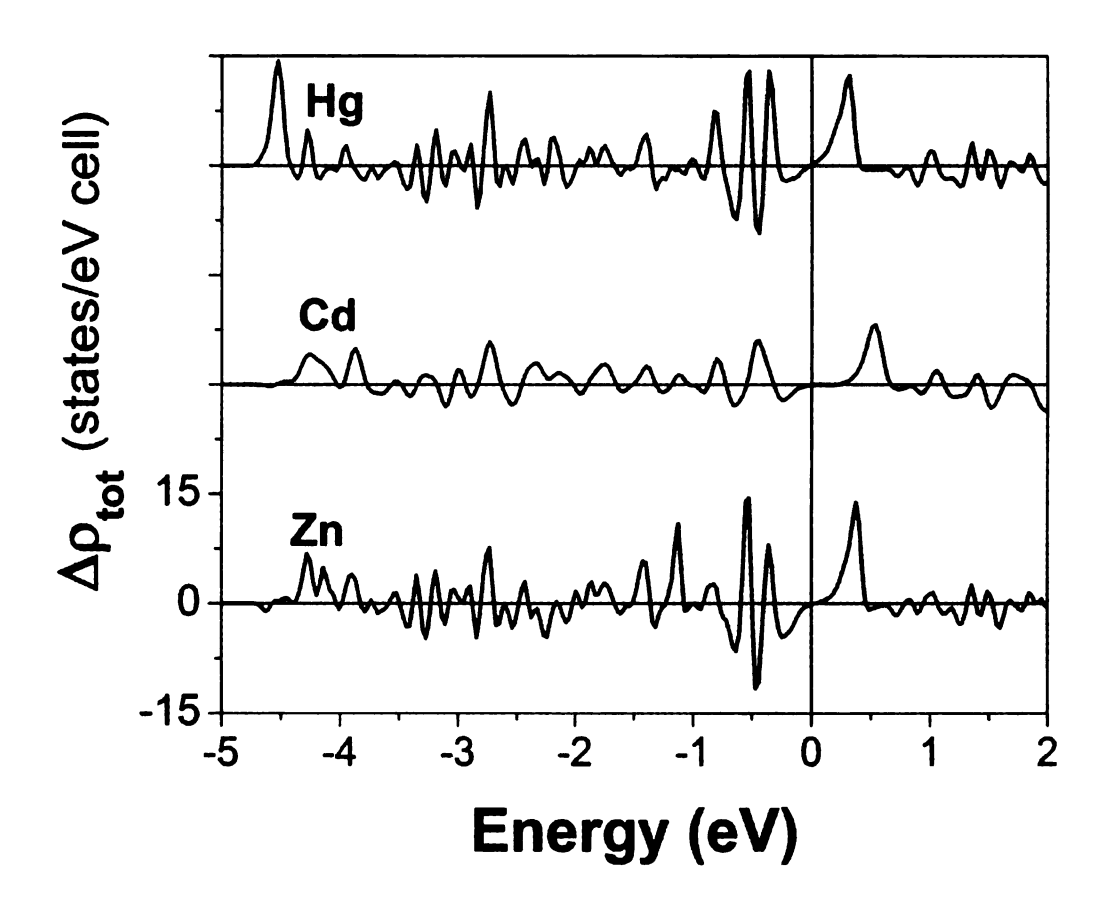


Figure 3.5 The difference in the total DOS ( $\Delta \rho_{tot}$ ) of PbTe with and without s-type divalent defects: Zn, Cd and Hg. The energy origin (0 eV) is chosen to be at the top of the valence band of PbTe.

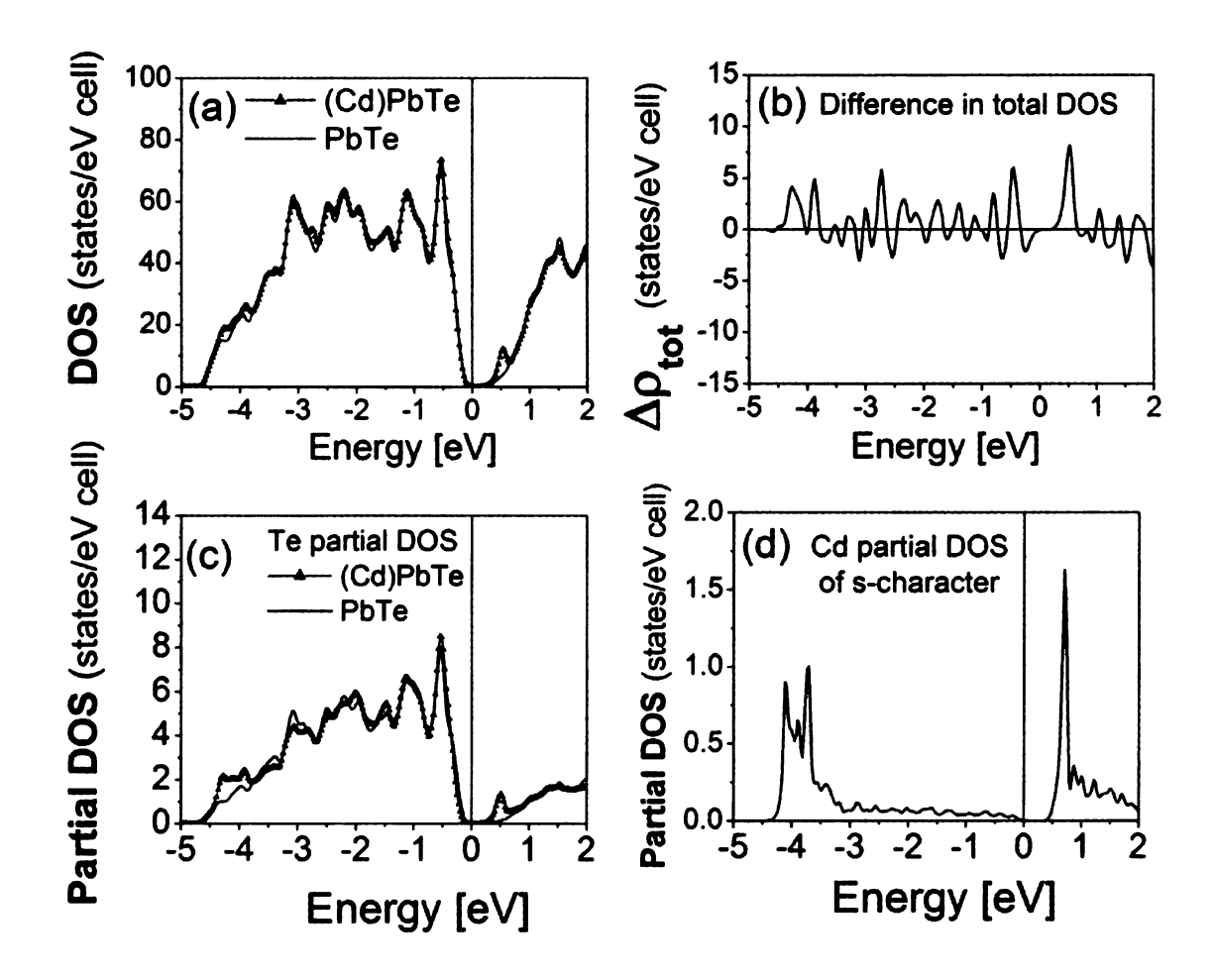


Figure 3.6 (a) The total DOS of PbTe with and without Cd impurity, (b) their difference  $\Delta p_{tot}$ , (c) partial DOS per Te associated with nearest neighbor Te atoms, and (d) Cd partial DOS of s-character. The Fermi energy of PbTe with Cd impurity is at the energy origin (0 eV).

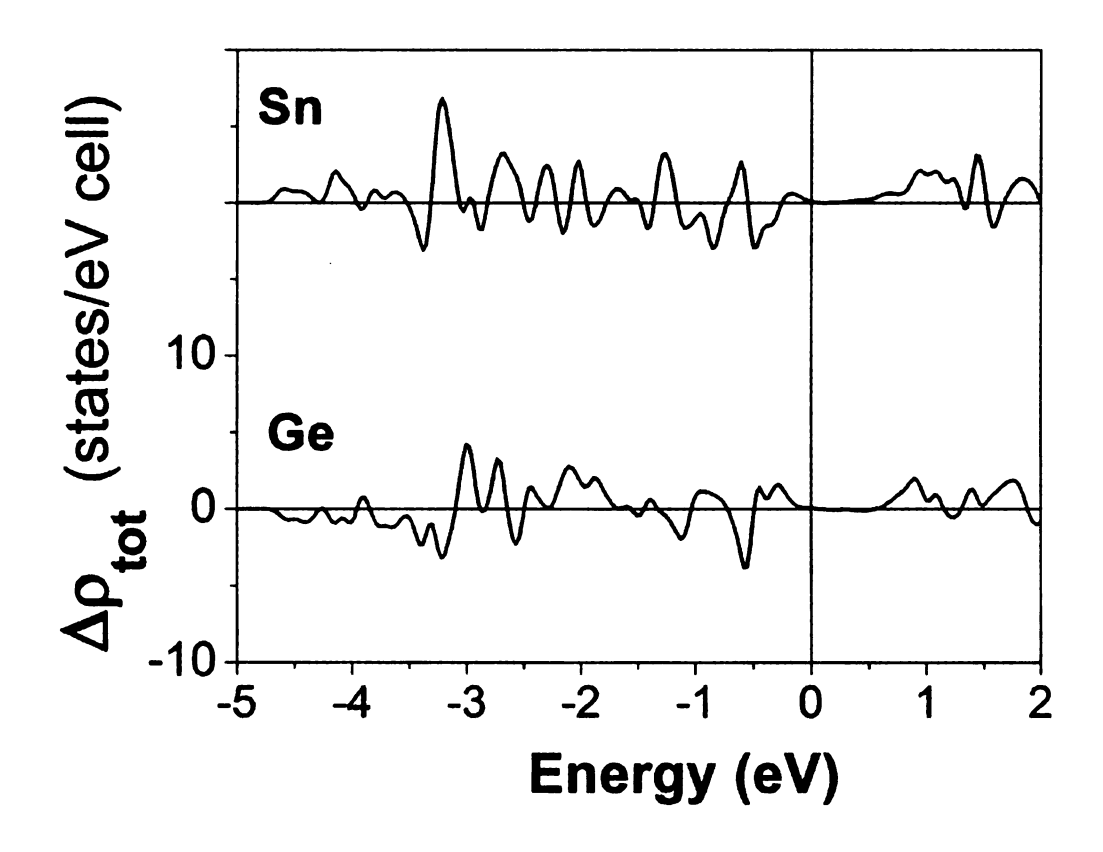


Figure 3.7 The difference in the total DOS ( $\Delta \rho_{tot}$ ) of PbTe with and without *p*-type divalent defects: Sn and Ge. The energy origin (0 eV) is chosen to be at the top of the valence band of PbTe.

#### 3.4.4 Trivalent impurity (Ga, In, Tl, As, Sb, Bi) in PbTe

Like the divalent case, we also have two types of trivalent impurities: group III (Ga, In, Tl) and group V (As, Sb, Bi). The valence configurations of the group III trivalent atoms are  $4s^2 4p^1$ ,  $5s^2 5p^1$  and  $6s^2 6p^1$  for Ga, In and Tl, respectively; whereas the valence configurations of the group V trivalent atoms are  $4p^3$ ,  $5p^3$  and  $6p^3$  for As, Sb and Bi, respectively.

Indium and other group III impurities (gallium and thallium) in IV-VI semiconductors have been known to exhibit anomalous behavior.[42, 43] For example they are n-type in PbTe and p-type in SnTe. When PbTe is doped with group III impurities, one observes the pinning of the Fermi energy and mixed-valence behavior. [17] The same impurity can be either donor or acceptor depending on the specific composition of the semiconductor. The Fermi-level stabilization within the band gap appears to be essential for understanding the unusual behavior of these systems and also for their practical application. Indium metal is nominally trivalent, and hence when In replaces a divalent Pb, one expects an n-type donor. This assumes that the number of states in the Te p band does not change when an In impurity is present. If the In s-state is strongly bound and lies below the valence p-band, then In will behave as an acceptor because it gives only one electron to the Te-p band instead of needed two. According to the current theoretical picture, these group III impurities exist in two valence states in the solid, one trivalent and the other monovalent (referred to as  $s^0p^3$  and  $s^2p^1$  states respectively where s refers to an impurity s-state and p refers to a band like p-state the precise relative of which is not known), an inhomogeneous mixed-valence picture. [44, 45] The divalent impurity state  $(s^1p^2)$  is an excited state. The trivalent and monovalent

states (two holes or two electrons in the impurity s-state) are degenerate and stabilized by the negative correlation energy [44, 45] as in the well-known negative-U Anderson model. [46] Thus half of the In impurities are trivalent (In<sup>3+</sup>) and the other half are monovalent (In<sup>1+</sup>). The Fermi level gets pinned between the empty and doubly occupied single particle defect states.

As I will show, my ab initio calculations give a different picture of the deep defect states associated with In and similar trivalent impurities in PbTe. In Fig. 3.8(a) and (b), we plot, respectively, the total density of states (DOS) for PbTe and InPb<sub>31</sub>Te<sub>32</sub> and the difference (after making a small relative rigid shift by 0.1 eV so that the Pb 6s core state and the highest peak in the valence band match). Clearly, we see a band of states split off below the valence-band minimum and a band of states split off above the valence-band maximum (VBM) and lying in the band gap region. The integrated DOS in both these bands of states is 2 (including spin degeneracy). The lower band is doubly occupied whereas the upper band is half full. The width of these two bands is  $\sim 0.25$  eV. We will refer to these bands as "localized" bands. What is most interesting is that the Fermi energy (at 0 eV) is at the middle of the upper "localized" band (the one in the gap). This can be easily understood if the Te-p valence band looses one state per/In impurity. Naively, one can say that the In 5s state is strongly bound and appears below the valence band minimum and is occupied by two In valence electrons. If the number of states in the valence band remained same as in PbTe, then the third In valence electron will go to this band, since Pb gives two electrons to fill the valence band in PbTe. The Fermi energy will be in the valence band giving 1 hole per In. The only way the Fermi energy can move to the upper "localized" band in the gap is if the valence band looses 1 state (2

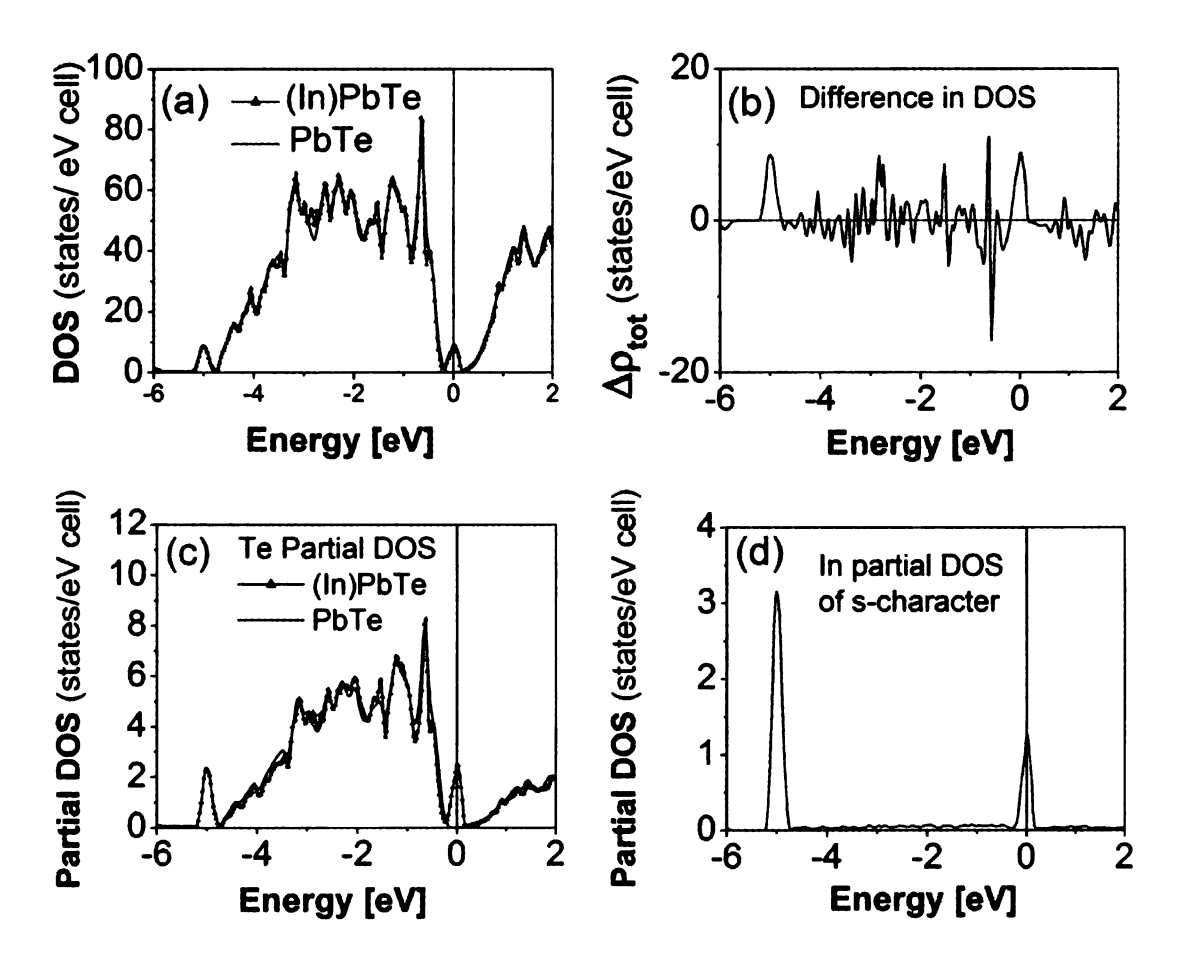


Figure 3.8 (a) The total DOS of PbTe with and without In impurity, (b) their difference  $\Delta \rho_{tot}$ , (c) partial DOS per Te associated with nearest neighbor Te atoms, and (d) In partial DOS of s-character. The Fermi energy of PbTe with In impurity is at the energy origin (0 eV).

including spin). This is precisely what happens, and the reason for the observed Fermi surface pinning in the band gap in In doped PbTe is a strong interaction between In and neighboring Te orbitals which removes one state from the valence band and gives rise to a new hybridized state in the gap, a classic example of a deep defect state (DDS) [11].

In order to understand the parentage of the two "localized" bands, we plot in Fig. 3.8(c) the partial DOS associated with Te atoms which are neighbors of In. Clearly, the Te p valence band of PbTe has changed dramatically in the presence of In. The two new "localized bands" have nearly similar Te p character. In Fig. 3.8(d), we show the In s character which contribute primarily to the "localized bands", the lower one has more In s-character. In addition, in FPLAPW calculations there is a substantial contribution to the charge density from the interstitial regions. The atomic radii have been chosen to be 1.53 Å for both In and Te and the distance between In and its nearest neighbor Te is 3.23 Å, leaving a substantial interstitial charge distribution. The upper "localized" band has more interstitial contribution, hence it is more delocalized. Thus the "localized" bands consist of strongly hybridized In s and Te p states. The lower one can be thought of bonding state between In s and neighboring Te p states and the upper one is the corresponding antibonding state.

Results for Ga and Tl atoms show that their deep defect states are resonant states near the top of the PbTe valence band (Fig. 3.9). The difference between In and the other two may explain the experimental anomalies seen in the case of In impurities in PbTe such as [17]. The resonant states at the top of the valence band for the Ga and Tl is caused by the overlap of the upper localized band of states with the states near the top of the valence band. We show, in Fig. 3.10 (a)-(d), the total and partial DOS of PbTe with

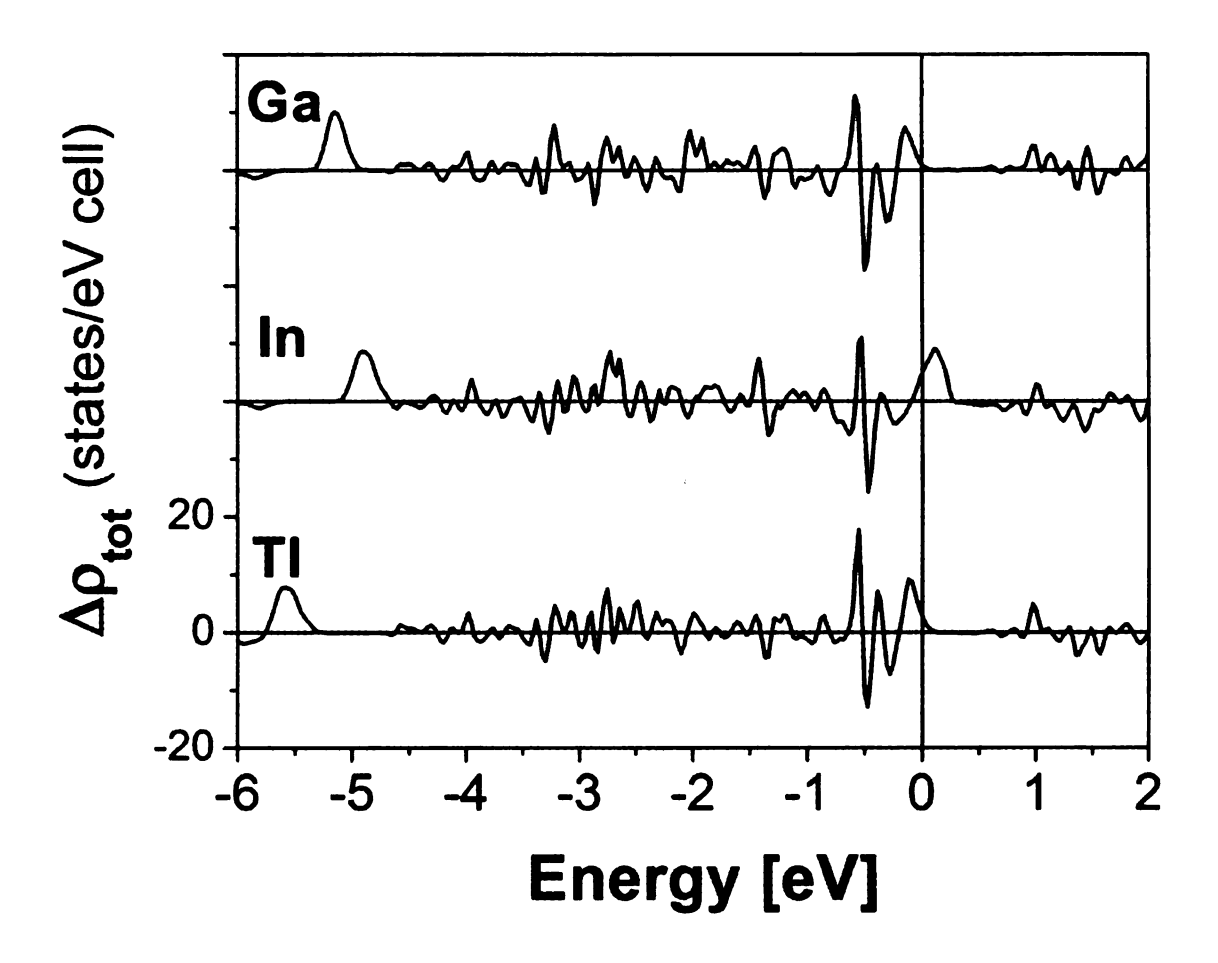


Figure 3.9 The difference in the total DOS ( $\Delta \rho_{tot}$ ) between PbTe with and without trivalent group III impurities: Ga, In, and Tl. The energy origin (0 eV) is chosen to be at the top of the valence band of PbTe.

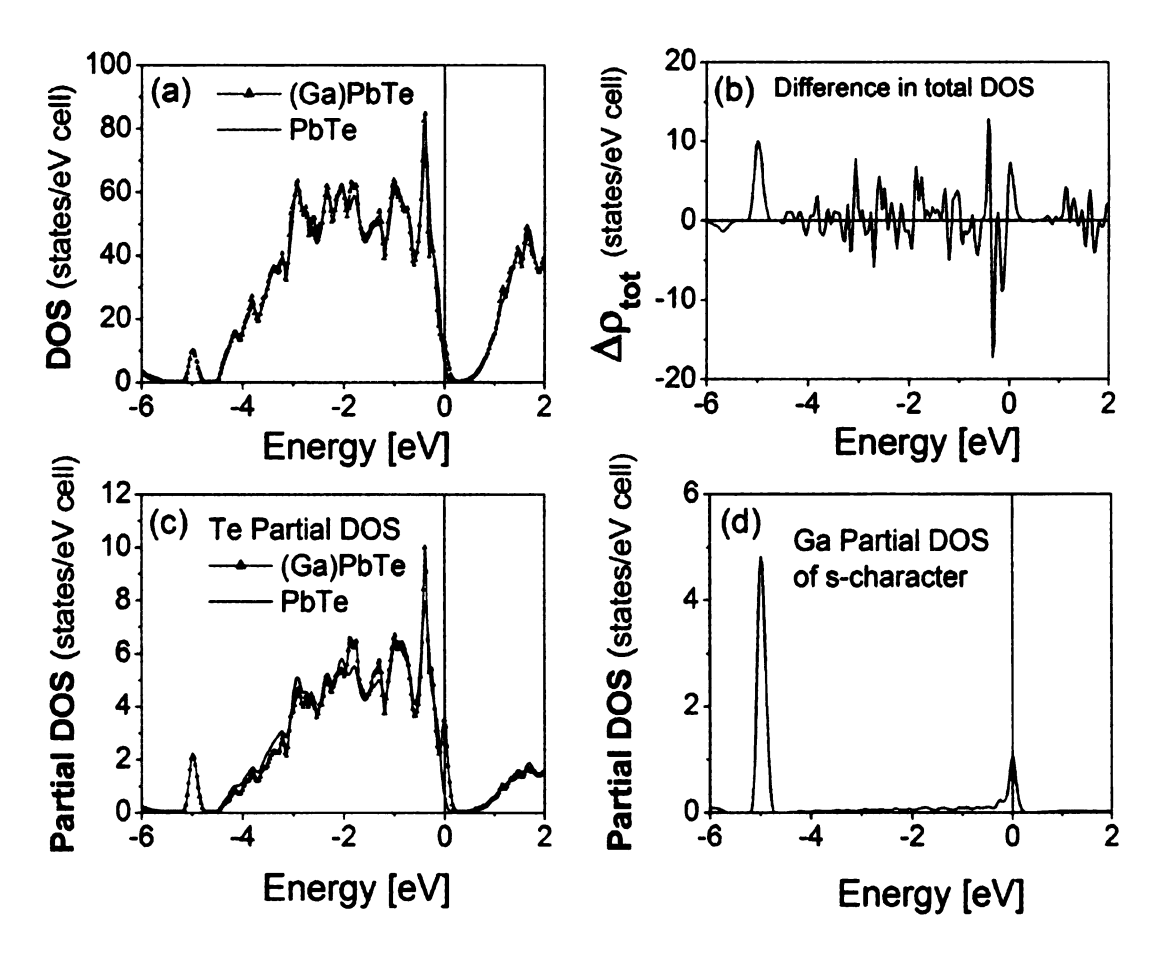


Figure 3.10 (a) The total DOS of PbTe with and without Ga impurity, (b) their difference  $\Delta \rho_{tot}$ , (c) partial DOS per Te associated with nearest neighbor Te atoms, and (d) Ga partial DOS of s character. The Fermi energy of PbTe with Ga impurity is at the energy origin (0 eV).

and without Ga impurity, the difference  $\Delta \rho_{tot}$ , and s character of the partial DOS of Ga impurity. Results for Tl impurity are similar except that the lower localized band (hyper deep state HDS) is further below the valence band minimum. The "hyper-deep" level at about -5.0 eV is predominantly impurity (Ga)-like whereas the resonant state centered around 0 eV is predominantly host (Te2)-like, which is consistent with the picture proposed by Hjalmarson *et al.*[48] The peak of the resonant state is about 0.25 eV below the VBM. This is consistent with the current understanding of the Tl-doped PbTe systems (see Ref. 17 and references therein). According to our calculations, Ga and Tl impurities should show rather similar behavior.

Results for group V impurities (As, Sb and Bi) show that they introduce resonant states near the bottom of the conduction band (see Fig. 3.11). In contrast to the group III impurities which have s and p valence electrons, the resonant states for these p valence electron impurities are rather broad, the sharpest structure being for As. In Fig. 3.12(a)-(d), we show the total and partial DOS of PbTe with the As impurity. The resonant state is a mixture of the p states of As and the p states of the neighboring Te2 atoms in almost equal proportions.

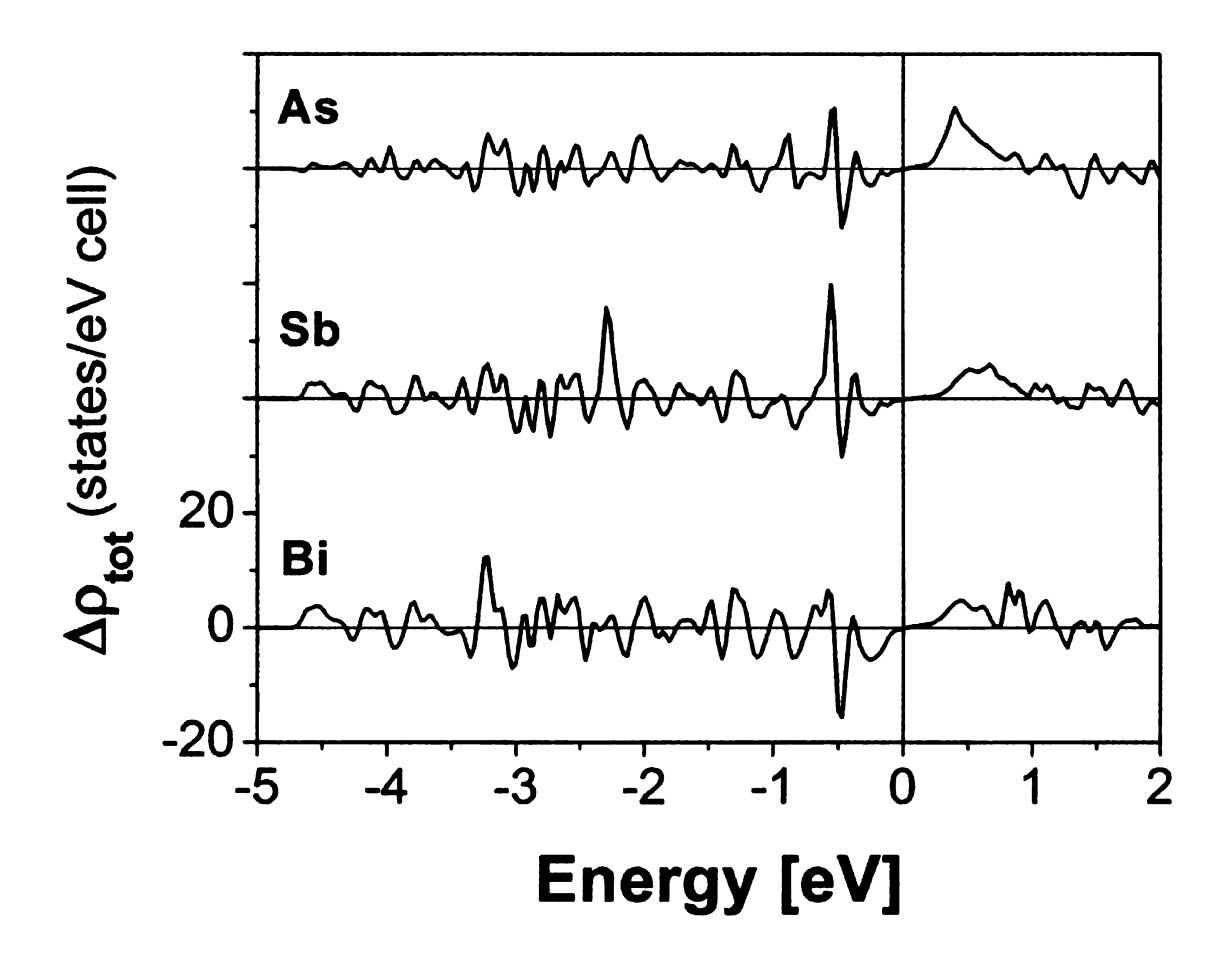


Figure 3.11 The difference in the total DOS ( $\Delta \rho_{tot}$ ) between PbTe with and without trivalent group V impurities: As, Sb, and Bi. The energy origin (0 eV) is chosen to be at the top of the valence band of PbTe.

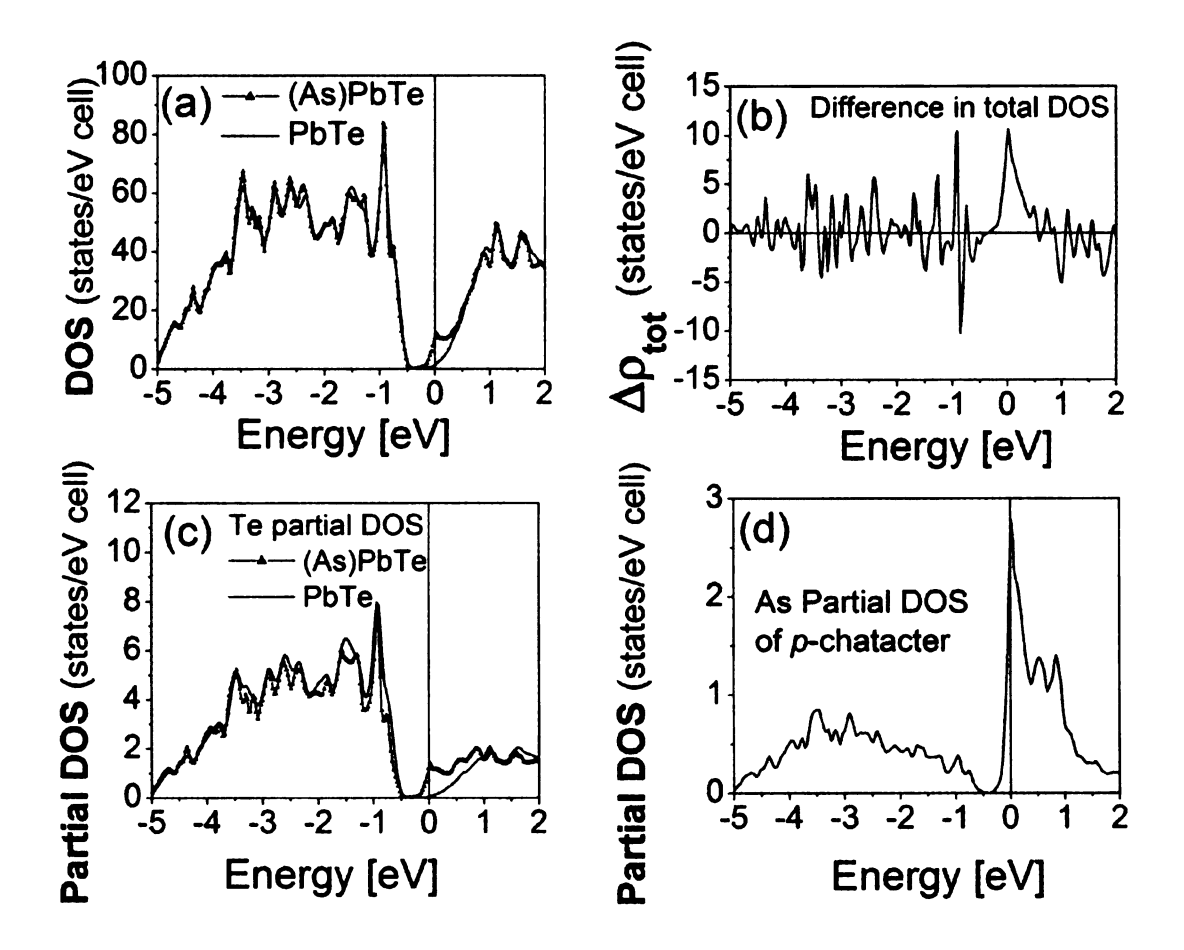


Figure 3.12 (a) The total DOS of PbTe with and without As impurity, (b) their difference  $\Delta \rho_{\text{tot}}$ , (c) partial DOS per Te associated with nearest neighbor Te atoms, and (d) As partial DOS of p character. The Fermi energy of PbTe with As impurity is at the energy origin (0 eV).

### 3.5 Te-site defects

As in the case of Pb-site defects, the removal of one Te atom (i.e., creation of one vacancy) or replacing it by another atom introduces a local charge disturbance and alters the covalent bonding with the neighboring Pb (denoted as Pb2) p states. As a result, we expect both the valence and conduction bands states to get strongly perturbed.

### 3.5.1 Te vacancy in PbTe

The total and partial DOS of PbTe with and without vacancy and the difference Δρ<sub>tot</sub> are shown in Fig. 3.13(a)-(c). For the sake of comparison, we shifted (downward) the DOS of PbTe with defect by  $\sim 0.455$  eV such that the core bands match perfectly. As we can see, the entire valence and conduction band DOS get perturbed by the vacancy. Since transport properties are controlled by the states near the Fermi energy (at 0 eV), let us focus on this region. As seen in Fig. 3.13(a)-(c), new states appear in the band gap region and near the bottom of the conduction band in the energy range -0.5 to 0 eV. Partial DOS analysis indicates that these states are predominantly of Pb p character [see Fig. 3.13(c)]. The valence band looses 6 states (including spin) per Te vacancy. These 6 states are occupied by 4 Te electrons and 2 Pb electrons. Removal of Te atom takes 4 valence electrons away leaving two Pb valence electrons. As a result, two Pb electrons occupy the new states mentioned above. The system then behaves like an n-doped system. Our picture is qualitatively consistent with that of Parada [15] who argued that each Te vacancy causes 4 states (8 states including spin) to be removed from the valence band and to move near the conduction band bottom. This picture includes the Te 5s core state. Since Te atom has 6 electrons, the extra two electrons (coming from Pb) occupying the 8 states in the valence band (in PbTe) have to move into the conduction band when a Te vacancy is present resulting in an *n*-type conduction. However, the detailed nature of the DOS near the bottom of the conduction band could not be obtained in earlier non-self consistent calculations.[15]

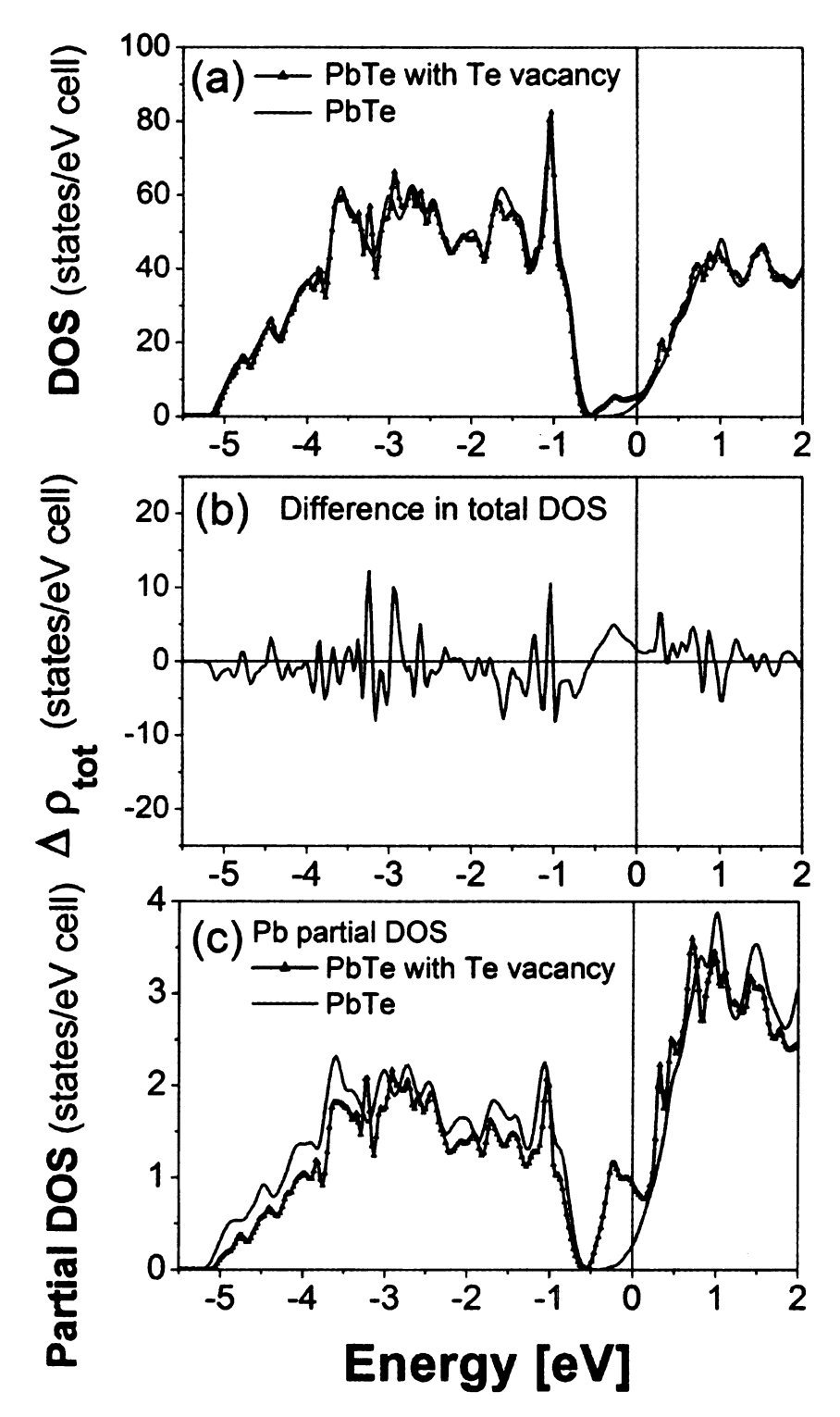


Figure 3.13 (a) The total DOS of PbTe with and without Te vacancy, (b) their difference  $\Delta \rho_{tot}$ , and (c) partial DOS per Pb associated with nearest neighbor Pb atoms. The Fermi energy of PbTe with Te vacancy is at the energy origin (0 eV).

### 3.5.2 S and Se impurities in PbTe

S and Se, like Te, need two electrons to fill their valence p shell. Thus one expects mainly the valence band to be perturbed when one replaces Te by S or Se and there should be a small perturbation of the conduction band (indirectly through changes in the hybridization effects). This is clearly seen in Fig. 3.14(a)-(c) and Fig. 3.15(a)-(c). The change in the valence-band DOS takes place over the entire valence-band energy range with a reduction in the DOS in the energy range of 0.5 eV from the top of the valence band. S and Se p states appear in the entire valence-band region peaking around 1.2-1.5 eV below the VBM [Fig. 3.14(d) and Fig. 3.15(d)]. The conduction band is hardly affected within about 1.0 eV from its minimum.

### 3.5.3 I impurity in PbTe

lodine (I) appears to act as an ideal donor in PbTe, in agreement with what is known about the halogen impurities in PbTe.[17, 49] It does not perturb the states either near the top of the valence band nor near the bottom of the conduction band as can be seen in Fig. 3.16(a)-(d). The major change in the DOS occurs near the bottom of the valence band around -5.0 eV (predominantly I p-character), near -1.1 eV and +1.0 eV due to changes in the Pb p hybridization effect. The Fermi energy is shifted to the conduction band making it an ideal n-type impurity (donor), consistent with experiments.

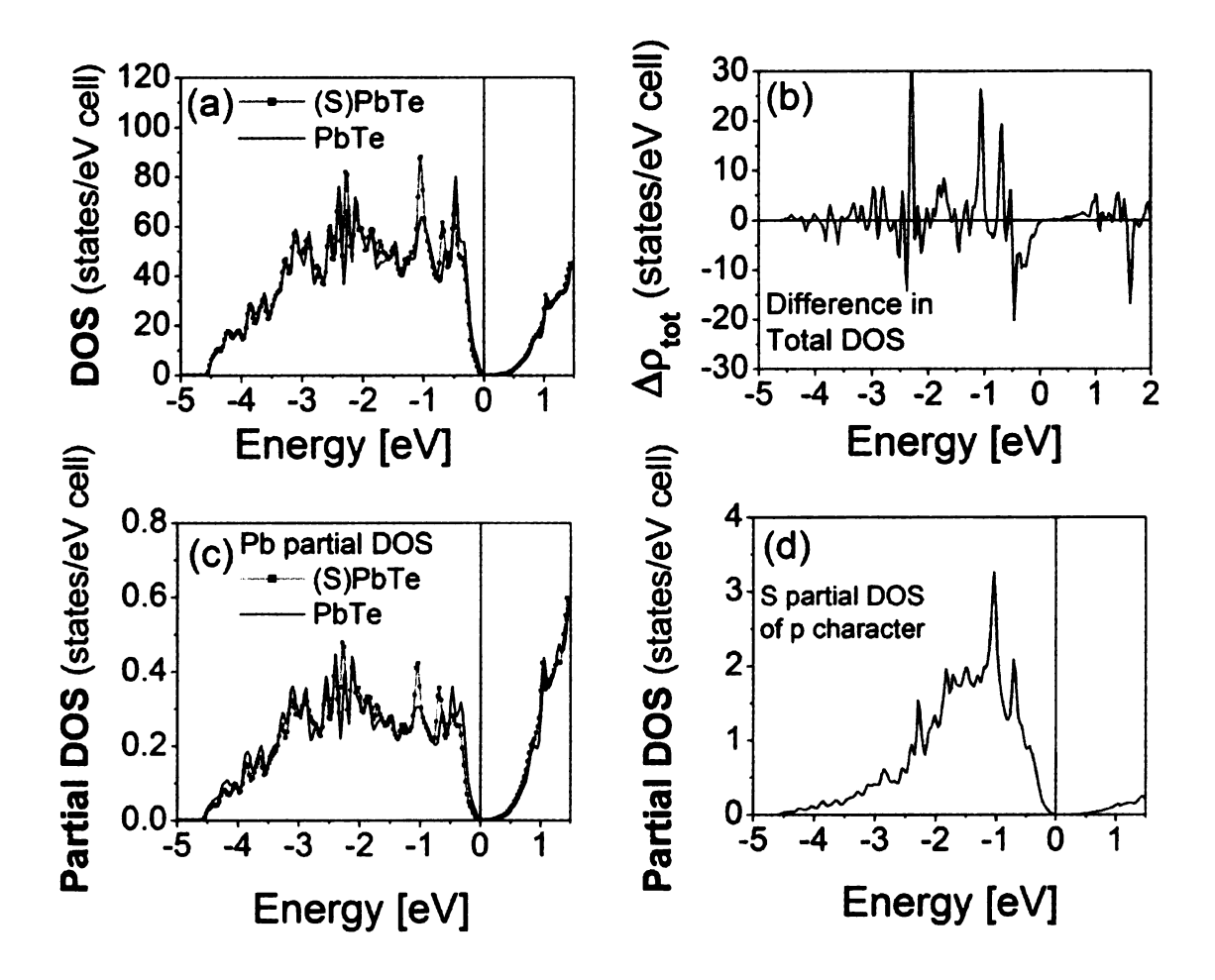


Figure 3.14 (a) The total DOS of PbTe with and without S impurity, (b) their difference  $\Delta \rho_{\text{tot}}$ , (c) partial DOS per Pb associated with nearest neighbor Pb atoms, and (d) S partial DOS of p character. The Fermi energy of PbTe with S impurity is at the energy origin (0 eV).

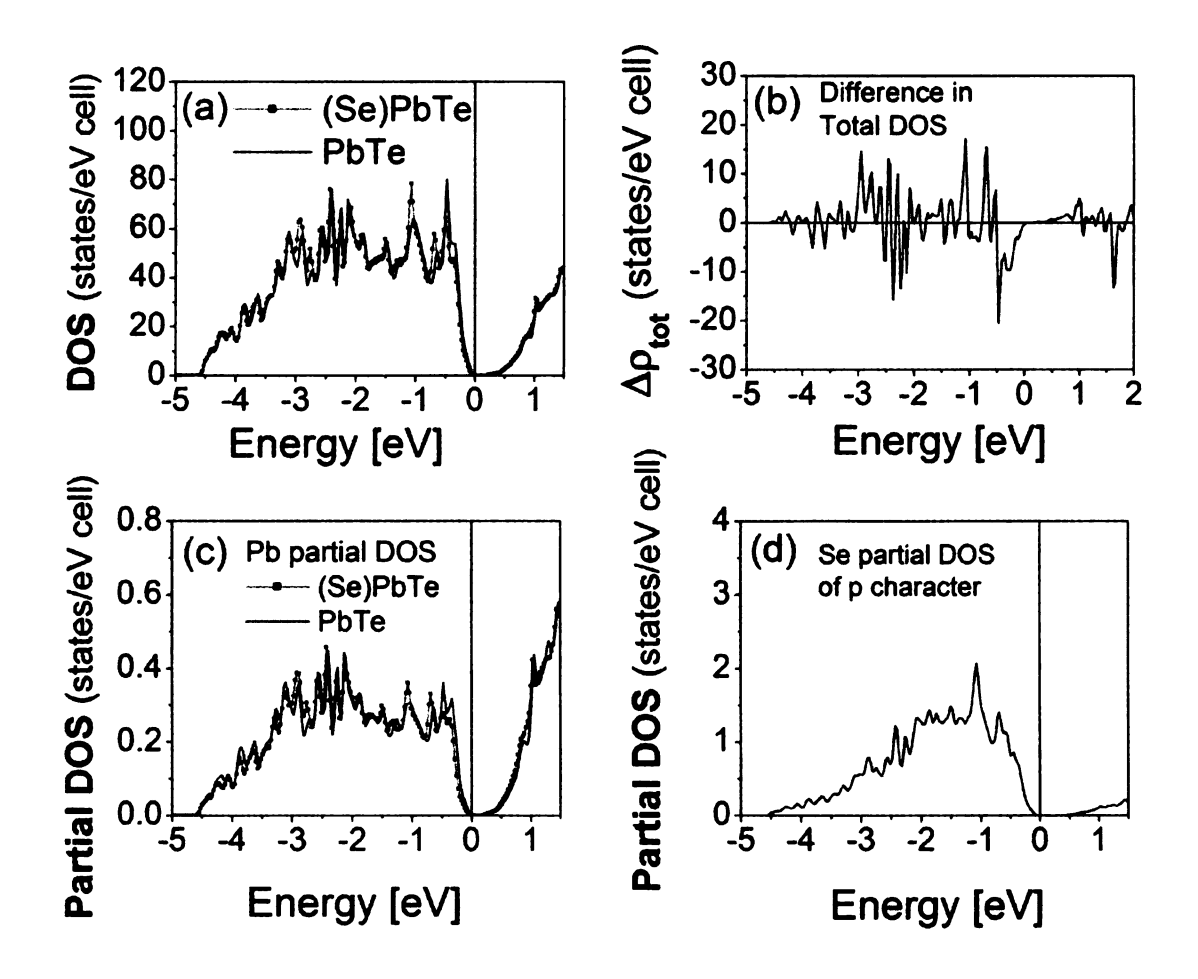


Figure 3.15 (a) The total DOS of PbTe with and without Se impurity, (b) their difference  $\Delta \rho_{tot}$ , (c) partial DOS per Pb associated with nearest neighbor Pb atoms, and (d) Se partial DOS of p character. The Fermi energy of PbTe with Se impurity is at the energy origin (0 eV).

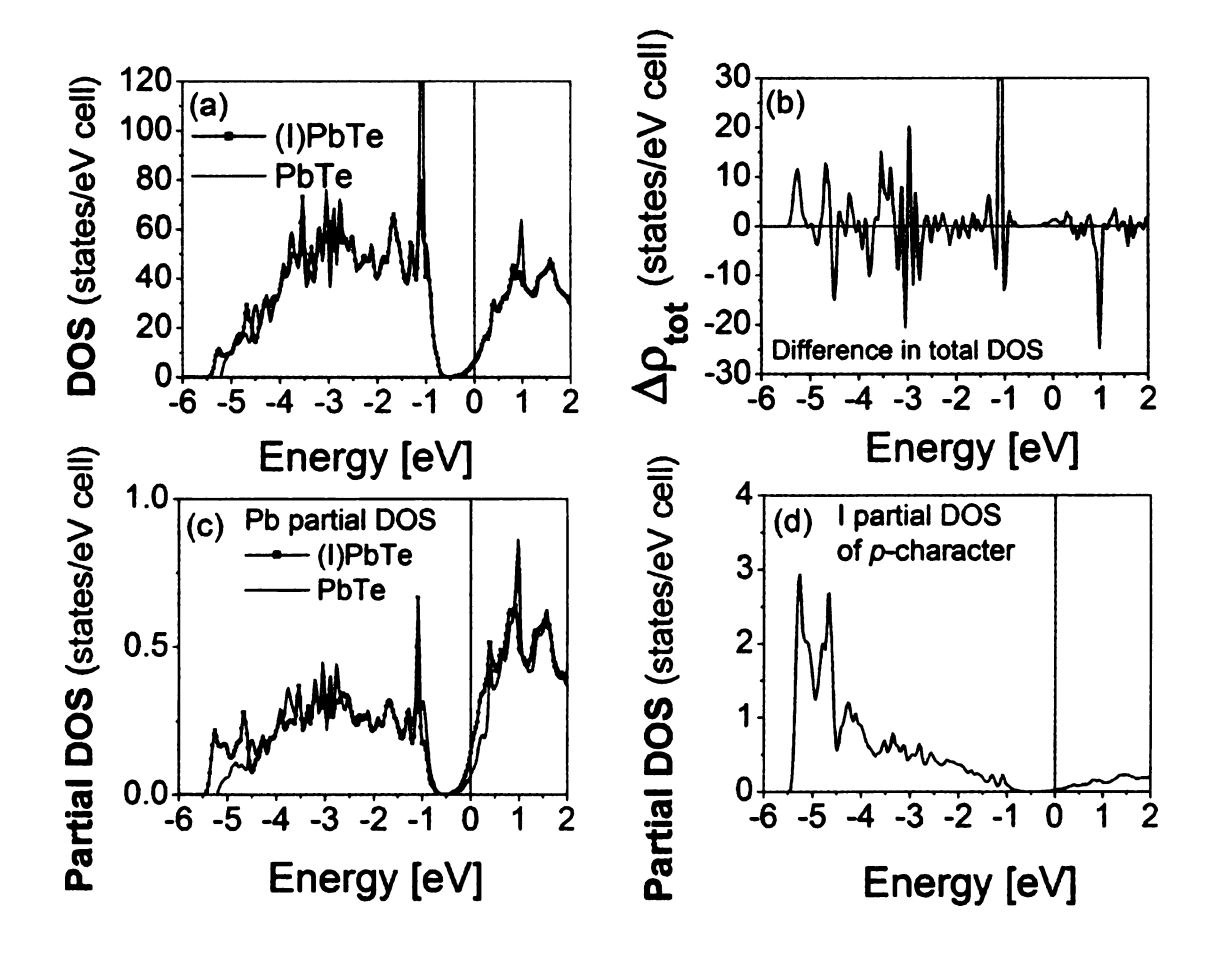


Figure 3.16 (a) The total DOS of PbTe with and without I impurity, (b) their difference  $\Delta \rho_{\text{tot}}$ , (c) partial DOS per Pb associated with nearest neighbor Pb atoms, (d) I partial DOS of p character. The Fermi energy of PbTe with I impurity is at the energy origin (0 eV).

### 3.6 Impurity-impurity interaction and the dilute defect limit

In the calculation of energy of the defect states using the supercell model containing 64 atoms, the defect-defect interaction appears to be appreciable, because the width of the so called localized bands in the In case, for example, is  $\sim 0.25 \text{eV}$ . It is therefore important to understand how much of the defect physics remains as one increases the distance between the impurities (when one goes to the dilute limit). Clearly the spectral weight of the impurity-induced changes in the DOS will scale with impurity concentration. In addition, we expect the impurity bandwidth to decrease. But the most significant question is how the position of the impurity band center changes relative to the conduction or valence band extrema. In order to see how the impurity-impurity interaction affects the DOS when two impurities are closer or farther than 13.16 Å, we have studied two different systems. One is In<sub>2</sub>Pb<sub>31</sub>Te<sub>32</sub>, i.e., two impurities in a (2x2x2) supercell, where one In is located at the corner and the other at the center of the supercell, the distance between two In impurities being 11.345 Å. The second is InPb<sub>107</sub>Te<sub>108</sub> with In located at the corner of a (3x3x3) cubic supercell, the distance between the two In impurities being 19.65 Å. For these two systems, we used the PAW [40] method since it is more computationally efficient than FP-LAPW [20] in handling large supercells like the (3x3x3) one containing 216 atoms. For the sake of clarity, we present here the results of calculations without the spin-orbit interaction (SOI).

In the case of In<sub>2</sub>Pb<sub>31</sub>Te<sub>32</sub>, the bandwidth of the hyper-deep defect state is the same as that of InPb<sub>31</sub>Te<sub>32</sub> (see Fig. 3.17) [50]. This can be understood using a symmetry argument. Since the impurity states have s-symmetry and the dominant contribution to the overlap between two impurity states comes through Te-p and Pb-p orbitals, one

expects the hopping amplitude between the two impurity states (in an effective tightbinding model) to be small due to the 90° relative arrangement of the overlap paths connecting the two impurities. In the case of InPb<sub>107</sub>Te<sub>108</sub>, our main results are summarized in Fig. 3.18 and Table 3.1 [50]. As we had expected, both the hyper-deep and deep defect states get narrower since the overlap between the In atoms becomes smaller. The bandwidths (as measured by E<sub>2</sub>-E<sub>1</sub>) change from 0.323 to 0.049 eV for the hyper-deep (a factor of 6.5 reduction) and from 0.654 to 0.120 eV for the deep defect state (a factor of 5.45 reduction). In order to see how the changes in the impurity separation affects their positions of the impurity band centers, we have used the bottom of the valence band (conduction band) as the reference point  $E_{0v}$  ( $E_{0c}$ ) for the hyper-deep (deep) defect states, since the valence and conduction bands are expected to be less sensitive to the size of the supercell than the impurity states. As seen in Table 3.1, E<sub>0v</sub> changes by only 0.001 eV and  $E_{0c}$  by 0.036 eV in going from (2x2x2) to (3x3x3) supercell; the energy separation between the hyper-deep level and  $E_{0v}$  (as measured by  $E_{av}$ - $E_{0v}$ ) increases from 0.425 to 0.449 eV, a rather small change of 0.024 eV (5.6% change); and the corresponding separation between the deep state and E<sub>0c</sub> (as measured by E<sub>av</sub>-E<sub>0c</sub>) increases from 0.511 to 0.525 eV, a yet smaller change of 0.014 eV (2.7%). We then speculate that if we increase the distance between the impurities further, the main effect will be to reduce the impurity bandwidths without further changing their positions (peaks) with respect to the band minima. Therefore we can use the results of smaller supercell calculations to discuss the qualitative physics.

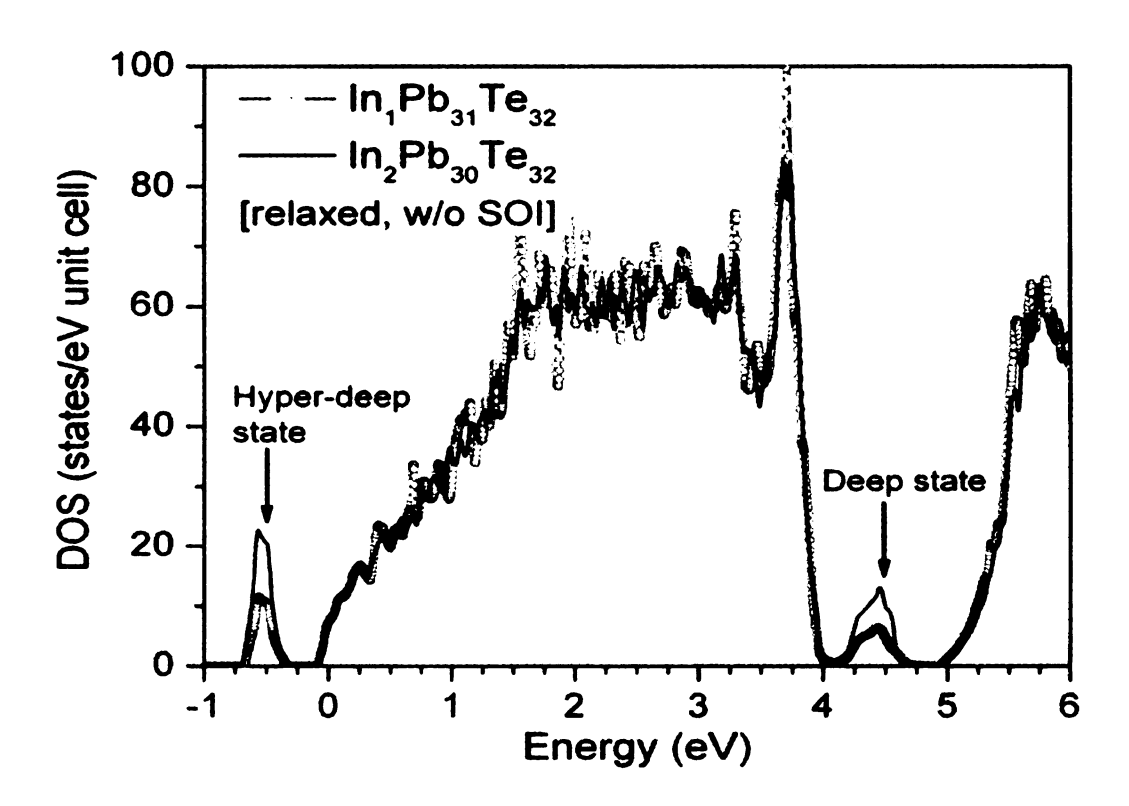


Figure 3.17 The total DOS of PbTe with In impurity obtained in PAW calculations using two different models: InPb<sub>31</sub>Te<sub>32</sub> with one In impurity at the corner, and In<sub>2</sub>Pb<sub>30</sub>Te<sub>32</sub> with one In at the corner and the other one at the center of a (2x2x2) supercell; the distance between the two In impurities being 13.1 Å and 11.345 Å, respectively. The two lines are almost identical except at ~-0.5 eV and ~4.5 eV where the integrated DOS of the deep and hyper-deep defect states of In<sub>2</sub>Pb<sub>30</sub>Te<sub>32</sub> are larger than those of InPb<sub>31</sub>Te<sub>32</sub> by a factor of 2. The Fermi energy is at the top of the upper localized band formed by the deep defect state. [50]

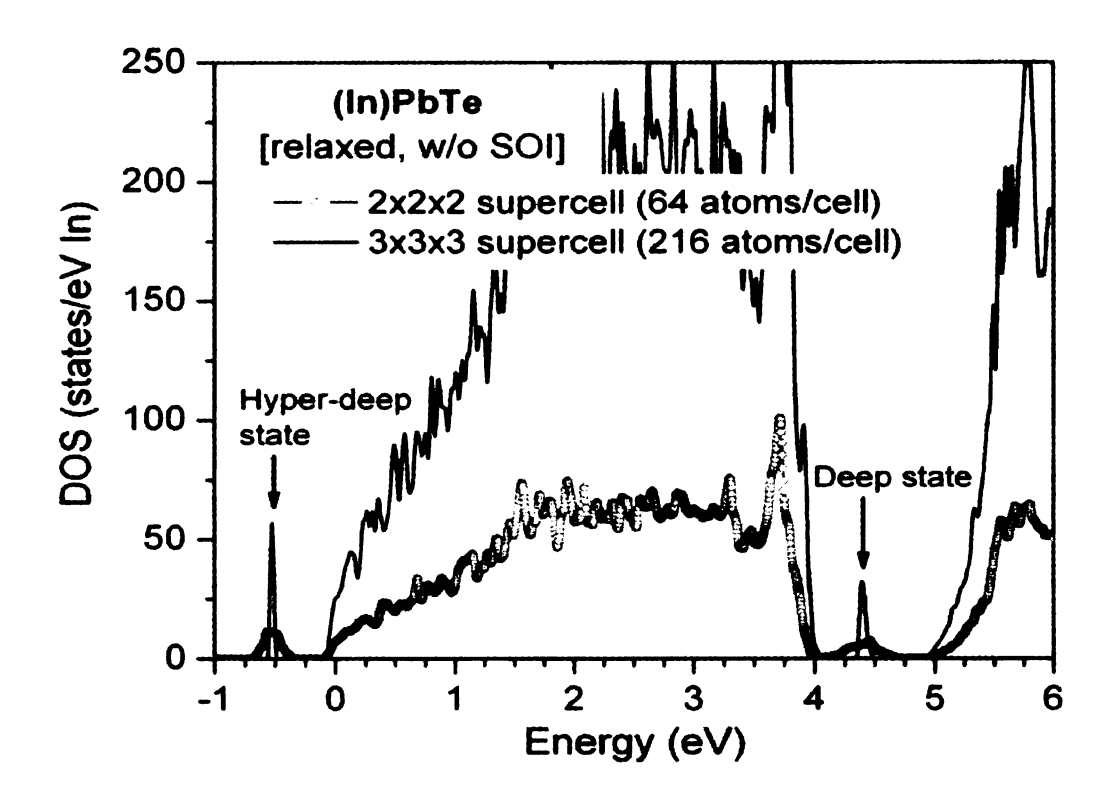


Figure 3.18 The total DOS of PbTe with In impurity obtained in PAW calculations using two different supercell sizes, (2x2x2) supercell [InPb<sub>31</sub>Te<sub>32</sub>] and (3x3x3) supercell [InPb<sub>107</sub>Te<sub>108</sub>]; the distance between the two In impurities being 13.1 Å and 19.65 Å, respectively. The Fermi energy is at the top of the upper localized band formed by the deep defect state. [50]

	(2x2x2) supercell		(3x3x3) supercell	
	Hyper-deep state	Deep state	Hyper-deep state	Deep state
E <sub>0v</sub> , E <sub>0c</sub>	-0.077	4.903	-0.076	4.939
$\mathbf{E_1}$	-0.340	4.065	-0.549	4.354
E <sub>2</sub>	-0.663	4.719	-0.500	4.474
$W=E_2-E_1$	0.323	0.654	0.049	0.120
$E_{av} = (E_2 + E_1)/2$	-0.502	4.392	-0.525	4.414

Table 3.1 Characteristics of the hyper-deep and deep defect states in PbTe with In impurity. Results obtained in PAW calculations using two different supercell sizes, (2x2x2) supercell (64 atoms/cell) and (3x3x3) supercell (216 atoms/cell).  $E_{0v}$  and  $E_{0c}$  are respectively at the bottom of the valence band (used as the reference for the hyper-deep states) and at the bottom of the conduction band (used as the reference for the deep states).  $E_1$  and  $E_2$  are respectively at the top and the bottom of the lower (upper) localized band formed by the hyper-deep (deep) defect state. W and  $E_{av}$  are respectively the width and the average position of the lower and upper localized bands. All these quantities are measured in eV.

## 3.7 Comparison with Experiments

One of the remarkable properties of the lead chalcogenide group of narrow band-gap semiconductors is that they have a range of non-stoichiometry accompanied by either Pb or Te vacancies. Our theoretical results predict that Pb vacancies produce *p*-type PbTe whereas Te vacancies produce *n*-type PbTe, which are consistent with the earlier model calculations.[14, 15] However, in contrast to these earlier semi-empirical or model studies, present *ab initio* calculations predict significant changes in the DOS near the band gap region, which should affect the transport properties quantitatively.

As regards monovalent impurities, Poudeu *et al.* [8] found that Na<sub>0.95</sub>Pb<sub>m</sub>SbTe<sub>m+2</sub> (m=20) was a *p*-type semiconductor with high thermoelectric FOM,  $ZT_{max}$  of ~ 1.7 at 650K. The observed *p*-type behavior is consistent with our *ab initio* calculations and what is known about Na and Li impurities in PbTe. To approach a Na concentration closer to that for m=20 compound (NaSbPb<sub>m</sub>Te<sub>m+2</sub>), we add one more Na atom at the middle of the 64 atom super cell. The calculation shows that the DOS in the region of the band gap does not change by this addition. Thus one can treat the Na<sub>0.95</sub>Pb<sub>20</sub>SbTe<sub>22</sub> as basically PbTe doped with holes. Its thermopower should therefore be positive.

The behavior of trivalent impurities such as In, Ga, Tl has been both interesting and puzzling. Gelbstein *et al.* [42] have recently argued that the thermoelectric property of In-doped PbTe can be understood in terms of the existence of deep-lying states generated by In-doping. We find that In not only introduces deep defect states in the band gap (perhaps overlap with the bottom of the conduction band) but also strongly reduces the DOS near the top of the valence band. This results in the reduction in the minority (hole) contribution to thermopower both due to DOS reduction and annihilation of the holes by electrons occupying the localized state in the gap. The net effect can be an increased *n*-type thermopower, as seen in [42].

As, Sb, and Bi give rise to resonant states near the bottom of the conduction band. Although this resonant state may not take part directly in transport properties because they are at least 0.5 above the band bottom, they indirectly affect the transport properties by increasing the DOS near the bottom of the conduction band. This was pointed out in Fig. 3.11 and Fig. 3.12. The increased DOS can in principle give rise to an increased thermopower in n-type systems. A simple calculation [51] of thermopower by assuming

energy-independent relaxation time showed that room temperature thermopower of AgSbPb<sub>2n-2</sub>Te<sub>2n</sub> could be large, as seen experimetally.[7] However, detailed calculations of transport coefficients taking into account the changes in band structure (caused by the Sb induced resonant states) and energy dependent scattering indicates that this enhancement of thermopower is not true in general but depends on the carrier concentration and temperature range studied.[52]

### 3.8 Summary

In summary, my ab initio electronic structure calculations in RPb<sub>2n-1</sub>Te<sub>2n</sub> (n=16), where R is a vacancy, or monovalent, divalent, or trivalent atom, show that when a Pb atom is substituted by R, the DOS gets perturbed over the entire valence and conduction bands. In addition, there are major changes in the DOS near the band gap region for most R. This should have significant impact on the transport properties of LAST-m compounds for m ≈ 18. We find that Na does not change the DOS within 0.5 eV of the band maxima; thus it is an ideal acceptor. In contrast, other alkali atoms and Ag and Cu give rise to an increase in the DOS near the top of the valence band and negligible change in the DOS near the bottom of the conduction band. Hg, Cd, Zn give rise to strong resonant state near the bottom of the conduction band and suppress the DOS near the top of the valence band (which is good for *n*-type thermoelectrics). Group V (As, Sb and Bi) impurities introduce resonant states near the bottom of the conduction band and should be good for n-type thermoelectrics. In contrast, the trivalent impurities (Ga, In, and Tl) either introduce bound states in the gap or resonant states near the top of the valence band.

Te vacancy also has a strong effect on the DOS of PbTe near the band gap region. New states appear in the band gap below the CBM, these states comprise primarily of the p states of Pb neighboring the vacancy. In contrast, the Pb vacancy increases the DOS near the top of the valence band but only by a small amount. Te vacancy should be n-type whereas Pb vacancy should be p-type. Iodine appears to be an ideal donor, it does not change the DOS of PbTe near the band gap, just shifts the Fermi energy to the conduction band. The divalent atoms S and Se also do not change the DOS near the CBM. There is however some depletion of the DOS near the VBM. These results should have important implications in the thermoelectric properties of, e.g., the n-type ternary compound PbTe<sub>1-x</sub>S<sub>x</sub>, [53] where one can synthesize mixed Te/S systems without appreciably affecting the conduction-band states and hence the n-type charge and energy transport.

# **Electronic Structure of Defects in SnTe**

### 4.1 General Introduction

Although the electronic structures of IV-VI semiconductors such as PbS, PbSe and PbTe [18, 19, 23, 28, 29] have been extensively studied in past using a large variety of methods (both empirical and ab initio), there is very little information about the electronic structure of SnTe using ab initio first principles electronic structure techniques excepting for only one calculations by Okoye [80]. Earlier non ab initio band structure calculations for SnTe have been carried out using many different techniques which include the empirical pseudopotential method [81, 82], the augmented plane wave method [83], the orthogonalized plane wave method [82] and the improved pseudopoential method [84]. All these calculations give results that show several common features but they differ in detail in comparison with experimental data.[80] Okoye has recently carried out an ab initio band structure calculation in SnTe using the full potential linearized augmented plane wave (FP-LAPW) method within the framework of the density functional theory (DFT). [80] His calculations have been performed with and without spin-orbit interaction (SOI); he found that the inclusion of SO coupling effects generally improved the agreement between the parameters studied (band gap, lattice constant, bulk modulus) and the experiment data. No defect structure

calculations in SnTe using *ab initio* methods have been done to our knowledge. In this Chapter, we discuss the results of our attempts to understand the physics behind the deep defect states formed by different types of defects in SnTe using self-consistent *ab initio* electronic structure calculations within DFT. The purpose of this work is to develop a systematic understanding of the defect states for different types of impurities (Sn and Te vacancies, substituting for Sn: Ag, Cd, In and Sb) and compare with those obtained in PbTe (Chapter 3). The arrangement of this chapter is as follows. In Sec. 2 I discuss the electronic structure of SnTe. In Sec. 3, the structural model and the method used to calculate the electronic structure are discussed briefly. In Sec. 4, I present the results for different type of impurities in SnTe. Finally, a brief summary is given in Sec. 5.

### 4.2 Electronic Structure of SnTe

SnTe crystallizes in the rock salt (NaCl) structure. The experimental lattice constant for SnTe is 6.327 Å. [85] SnTe has a direct minimum energy band gap of 0.23 eV [86], and as in PbTe the gap occurs at the L point in the face centered cubic (fcc) Brillouin Zone (Fig. 4.1). The theoretical band gap (with SOI and using GGA) is  $E_g = 0.212$  eV [80]. Orbital analysis shows that Te and Sn p states strongly hybridize, suggesting covalent interaction between these two atoms. The valance band has more Te p character whereas the conduction band has more Sn p character. The DOS of SnTe shows that the Sn s-band overlaps with the valance band, as shown in Fig. 4.2, unlike the Pb s-band in PbTe, which lies below the valence band minimum by  $\sim 0.8$  eV. This is due to the larger relativistic effects (Darwin and mass velocity correction) in Pb.

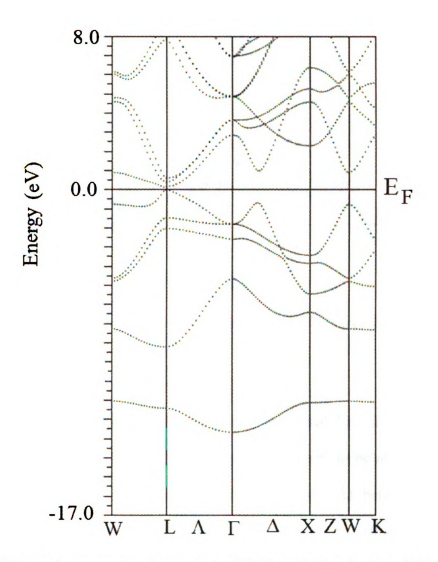


Figure 4.1 Electronic energy band structure of SnTe calculated using GGA including SOL[80]

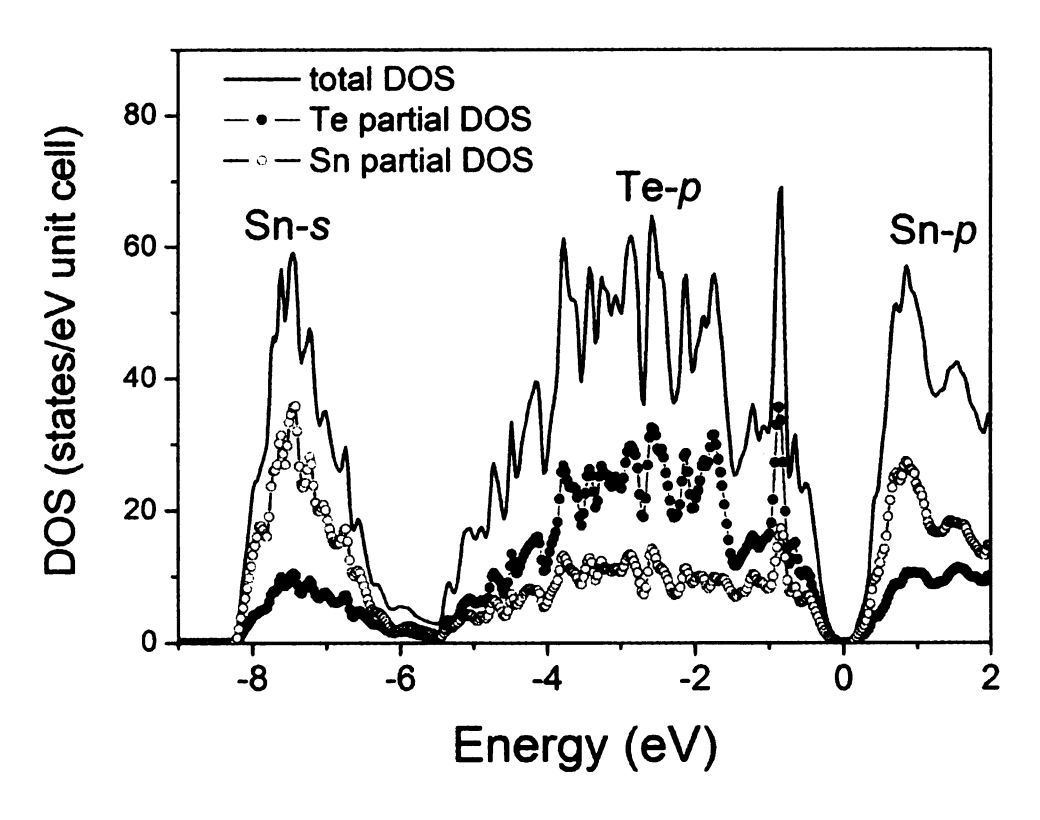


Figure 4.2 Total Density of state of SnTe calculated using GGA including SOI.

### 4.3 Defects in SnTe

To model the impurities and the vacancy we have used the 2x2x2 supercell model consisting of 64 atoms (see Fig. 3.2). We choose the defects to be at the origin of the supercell with separation of two lattice constants (12.654 Å) between the defects. Convergence of the self-consistent iterations was performed using 10 k-points inside the reduced cubic Brillouin zone (for cubic supercell) to within 0.0001 Ry (1.36 meV) with a cutoff -6.0 Ry between the valance and the core states. For all calculations we use the experimental lattice constant of SnTe.

The removal of a Sn atom (vacancy) or replacing it by a monovalent or trivalent cation introduces a local charge disturbance and alters the covalent bonding with the neighboring Te (denoted as Te2) p states. As a result the valence band and conduction

band states get strongly perturbed. One expects acceptor-like states to appear near the top of the valence band or donor like states near the bottom of the conduction band, whose precise positions can only be obtained after a detailed self consistent calculation. Also because of the local nature of the perturbation we expect the entire valence band and large part of the conduction band region to be affected. It is important to emphasize that simple shallow impurity state models may not be able to describe the short range physics of these impurity systems, as justified in PbTe case. Only a careful self consistent *ab initio* calculation will be able to do so.

### 4.3.1 Sn vacancy in SnTe

The total DOS with one Sn vacancy, without Sn vacancy and the difference between the two are shown in Fig. 4.3 (a,b). For the sake of comparison we shifted the DOS of the SnTe upward by  $\sim 0.25$  eV so the core bands Te-s band matched perfectly. As we can see the entire valence band and conduction band density of states (up to 2 eV) get modified in the presence of the vacancy. Since transport properties are controlled by the states near the top of the valence band and the bottom of the conduction band we will focus on the changes near band gap region within an energy range of  $\pm 0.5$  eV. We see that there is little change near the bottom of the conduction band DOS whereas there is an increase in the DOS near the top of the valence band. In order to see which atoms contribute near the top of the valence band DOS we show the difference in the projected DOS  $\Delta \rho = \rho$  (with defect)  $-\rho$  (SnTe) associated with six Te nearest neighbor neighbors of the vacancy in Fig 4.3 (c). The major contribution to the increase comes from the six nearest neighbor Te atoms and we see that Te states near the bottom part of the valence

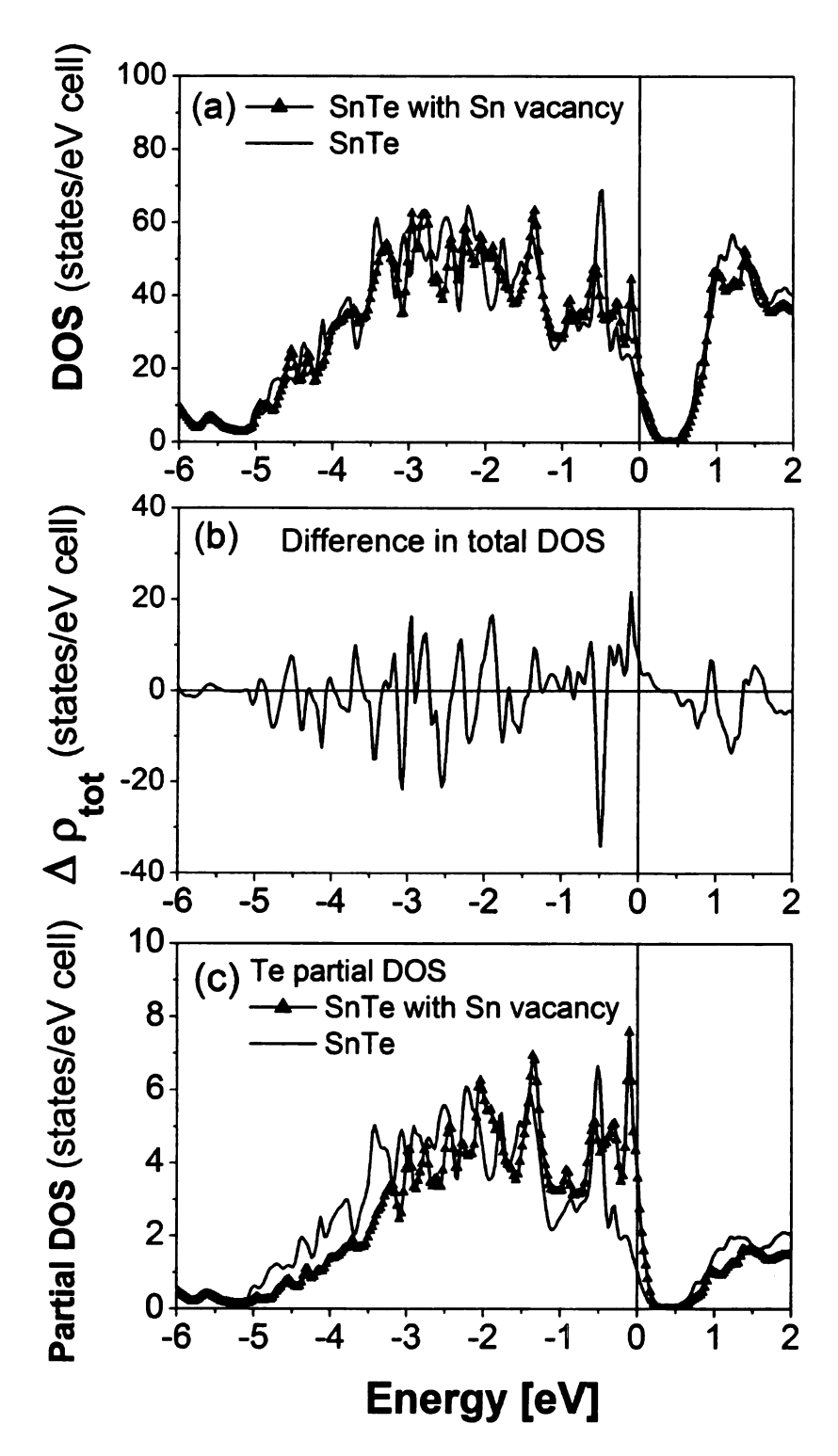


Figure 4.3 (a) The total DOS of SnTe with and without Sn vacancy, (b) their difference  $\Delta \rho_{tot}$ , and (c) partial DOS per Sn associated with nearest neighbor Te atoms. The Fermi energy of SnTe with Sn vacancy is at the energy origin (0 eV).

band get pushed towards the top. This shift is partially compensated by the DOS associated with the other atoms. Also other Sn and Te atoms do contribute to the increased DOS near the valence band maximum. From Fig. 4.3(a), we can clearly see that the Sn vacancies give rise to holes as expected. A comparison between the Sn vanacny in SnTe with Pb vanacny in PbTe, we can see that Sn vacancy perturbs the conduction bottom (reduction in the DOS in the energy range 0.5-1.0 eV), whereas Pb vacancy in PbTe does not perturb the conduction band (see Fig. 3.3).

### 4.3.2 Te vacancy in SnTe

The total and partial DOS of SnTe with and without Te vacancy and the difference  $\Delta p_{tot}$  are shown in Fig. 4.4(a)-(c). For the sake of comparison, we shifted downward the DOS of SnTe with defect by  $\sim 0.455$  eV such that the core bands match perfectly. As we can see, the entire valence and conduction band DOS get perturbed by the vacancy. New states appear in the band gap region and near the bottom of the conduction band in the energy range -0.5 to 0 eV but clser to the valence band maximum compared to PbTe case (see Fig. 3.13). Partial DOS analysis indicates that these states are predominantly of Sn p character [see Fig. 4.4(c)]. For each Te vacancy, the valence band looses 6 states (including spin). These 6 states are occupied by 4 Te electrons and 2 Sn electrons. Removal of Te atom takes 4 valence electrons away leaving two Sn valence electrons. As a result, two Sn electrons occupy the new states appearing above the valence band. The system then behaves like an n-doped system.

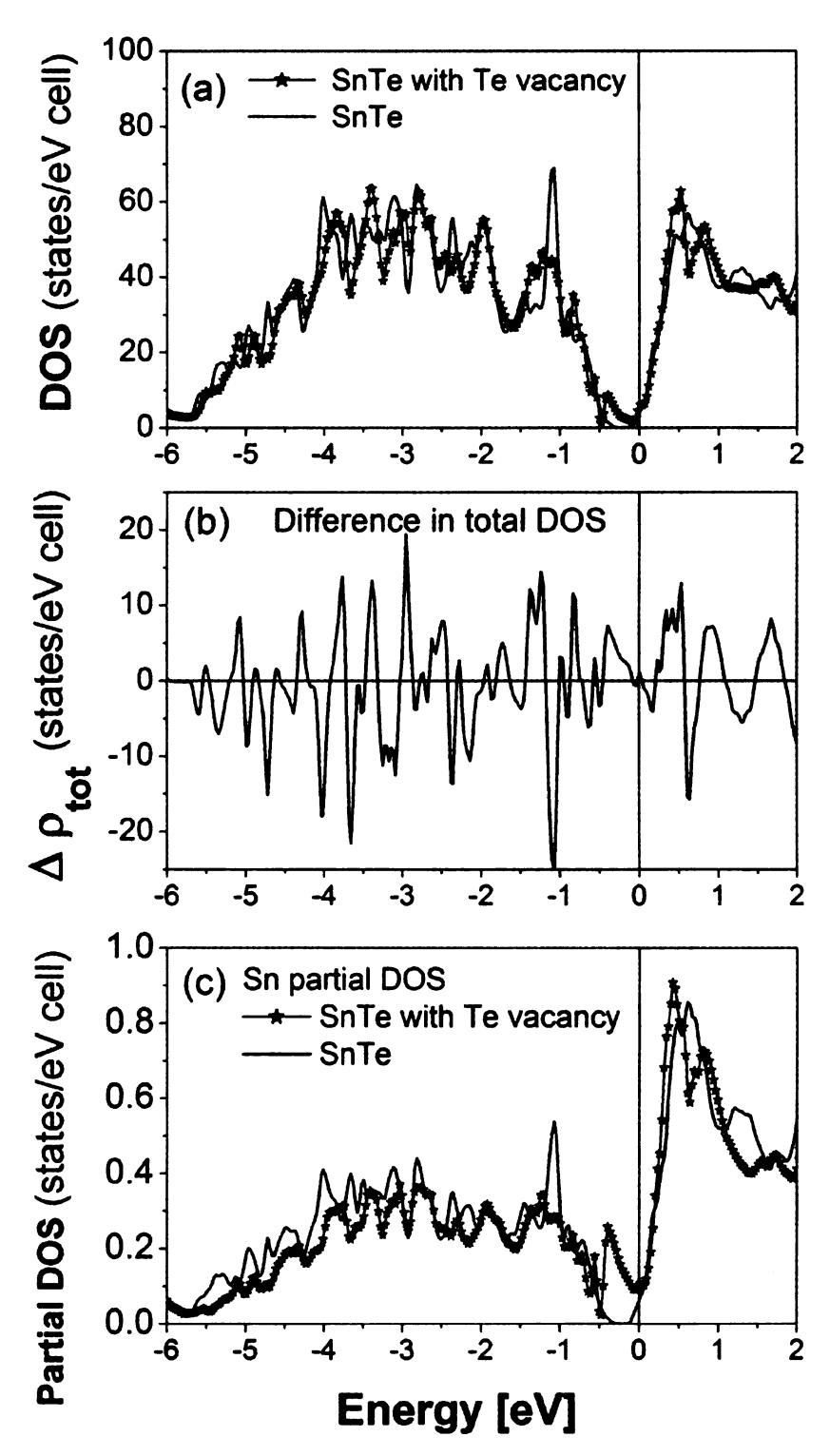


Figure 4.4 (a) The total DOS of SnTe with and without Te vacancy, (b) their difference  $\Delta \rho_{tot}$ , and (c) partial DOS per Te associated with nearest neighbor Sn atoms. The Fermi energy of SnTe with Te vacancy is at the energy origin (0 eV).

### 4.3.3 Ag impurity in SnTe

Ag is a monovalent impurity, it provides a weaker perturbation (changes the ionic charge by 1) compared to the Sn vacancy (change the ionic charge by 2). In Fig. 4.5 (a,b), we plot the total density of states (DOS) for  $Sn_{32}Te_{32}$  and  $AgSn_{31}Te_{32}$  and their difference (after making a small relative rigid shift by -0.326 eV so that the Te s core band match perfectly). We find that Ag impurity perturbs the valence band states, within energy range (-4 to -3 eV), due its core d states hybridizing with the Te p bands. The difference in the total DOS with and without Ag impurity shows a small peak near the top of the valance band (similar to PbTe- see Fig. 3.4). Since the s state of the Ag is above the valance band, Ag donates one electron when it replaces Sn (which is divalent), it gives rise to one hole per impurity and hence acts as an acceptor.

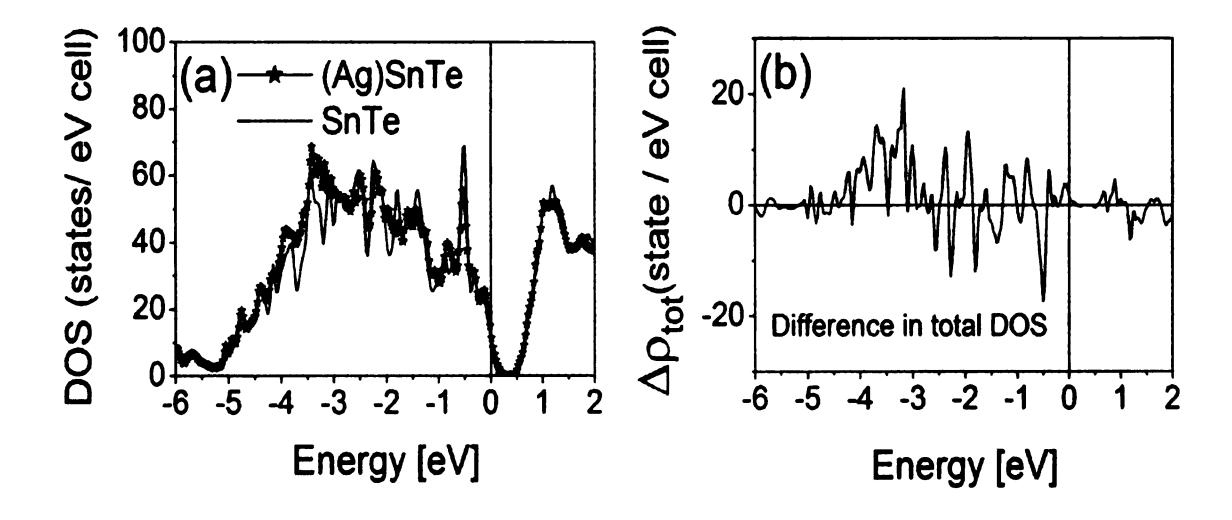


Figure 4.5 (a) The total DOS of SnTe with and without Ag impurity, (b) their difference  $\Delta \rho_{\text{tot}}$ . The Fermi energy of SnTe with Ag impurity is at the energy origin (0 eV).

### 4.3.4 Cd impurity in SnTe

Cd is a divalent impurity, the valence configurations of Cd is  $5s^2$  whereas the valence state of divalent Sn is  $5p^2$ . Naively, one can say when Cd replaces Sn, one expects the Fermi energy position to be unchanged (as in the case of SnTe), if the number of states in the valence band remains the same as in SnTe. Our ab initio calculations give a completely different picture when Cd substitutes for Sn in SnTe. In Fig. 4.6(a)-(d), we show the total and partial DOS of SnTe with Cd impurity. The Fermi energy lies in the conduction band. The only way the Fermi energy can move to the conduction band is if the valence and the Sn s bands loses 2 state (4 including spin) to the conduction band. This is precisely what happens, and the reason for the observed Fermi energy in the conduction band in Cd doped SnTe is a strong interaction between Cd and neighboring Te orbitals which removes one state from the valence band and gives rise to a new hybridized state near the bottom of the conduction band. The integrated DOS of the valence and Sn s bands show a loss of 2 states (4 including spin). One of these two states is from missing Sn  $5s^2$  state (two electrons) and the other state moves to the conduction band giving rise to a new hybridized state near the bottom of the conduction band. Because of the resonant state near the bottom of the conduction band, we expect electrondoped Cd systems to exhibit large thermopower. Cd in PbTe, as discussed in chapter 3, also shows resonant states near the bottom of the conduction but in contrast to SnTe the Fermi energy in PbTe remains in the gap, below the resonant state. This difference is intriguing and more careful calculations are needed to understand the physics behind the major difference of Cd defect in PbTe and SnTe.

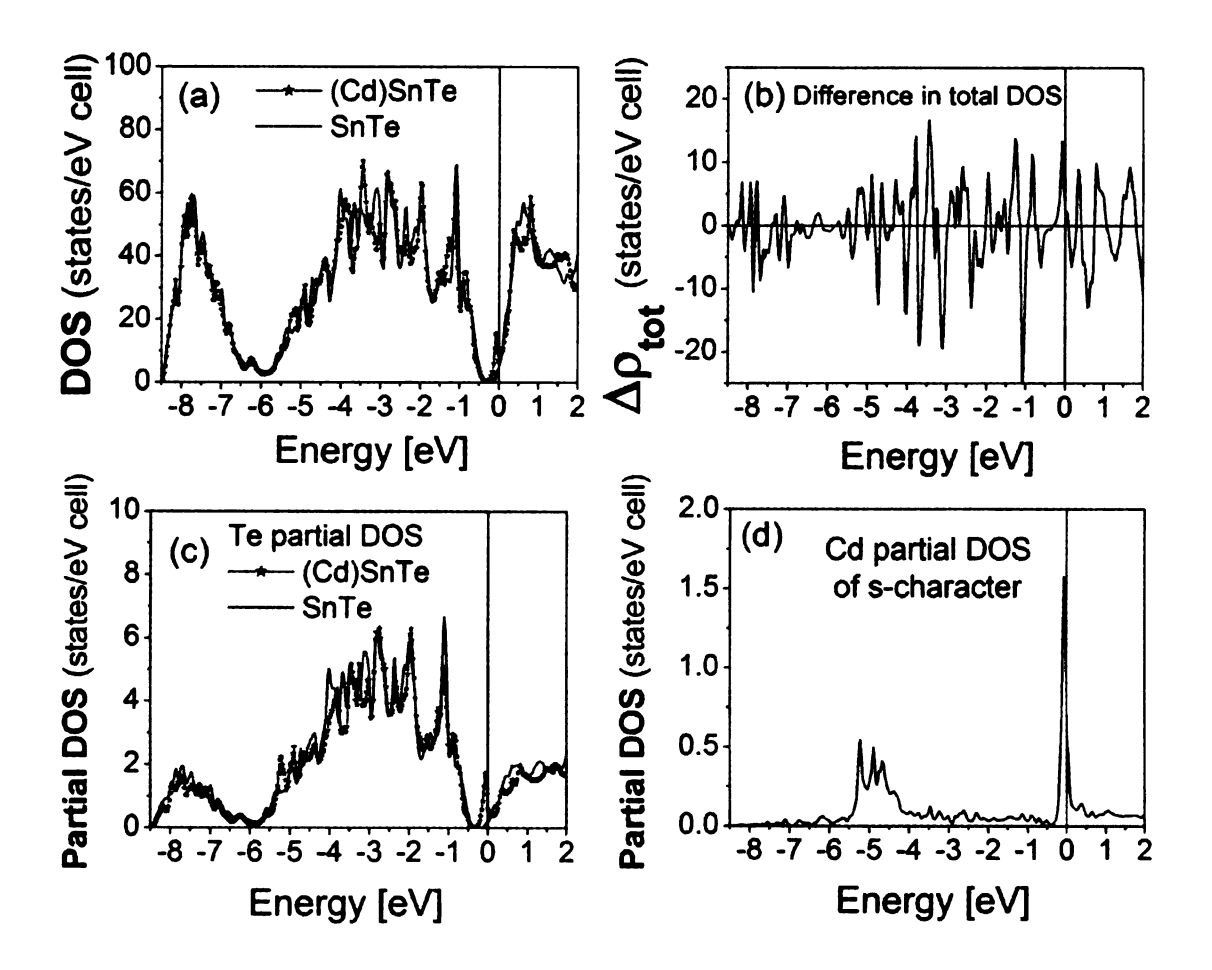


Figure 4.6 (a) The total DOS of SnTe with and without Cd impurity, (b) their difference  $\Delta p_{tot}$ , (c) partial DOS per Te associated with nearest neighbor Te atoms, and (d) Cd partial DOS of s-character. The Fermi energy of SnTe with Cd impurity is at the energy origin (0 eV).

### 4.3.5 Sb impurity in SnTe

Sb is a trivalent impurity, the valence configurations of the Sb is  $5p^3$ , The valence state of divalent Sn is  $5p^2$ . Results for Sb impurity show broad resonant states (width  $\sim 1$  eV) near the bottom of the SnTe conduction band. In Fig. 4.7(a)-(d), we show the total and partial DOS of SnTe with the Sb impurity. The resonant state is a mixture of the p-states of Sb and the p states of the neighboring Te2 atoms in almost equal proportions. The Sb impurity act as donor.

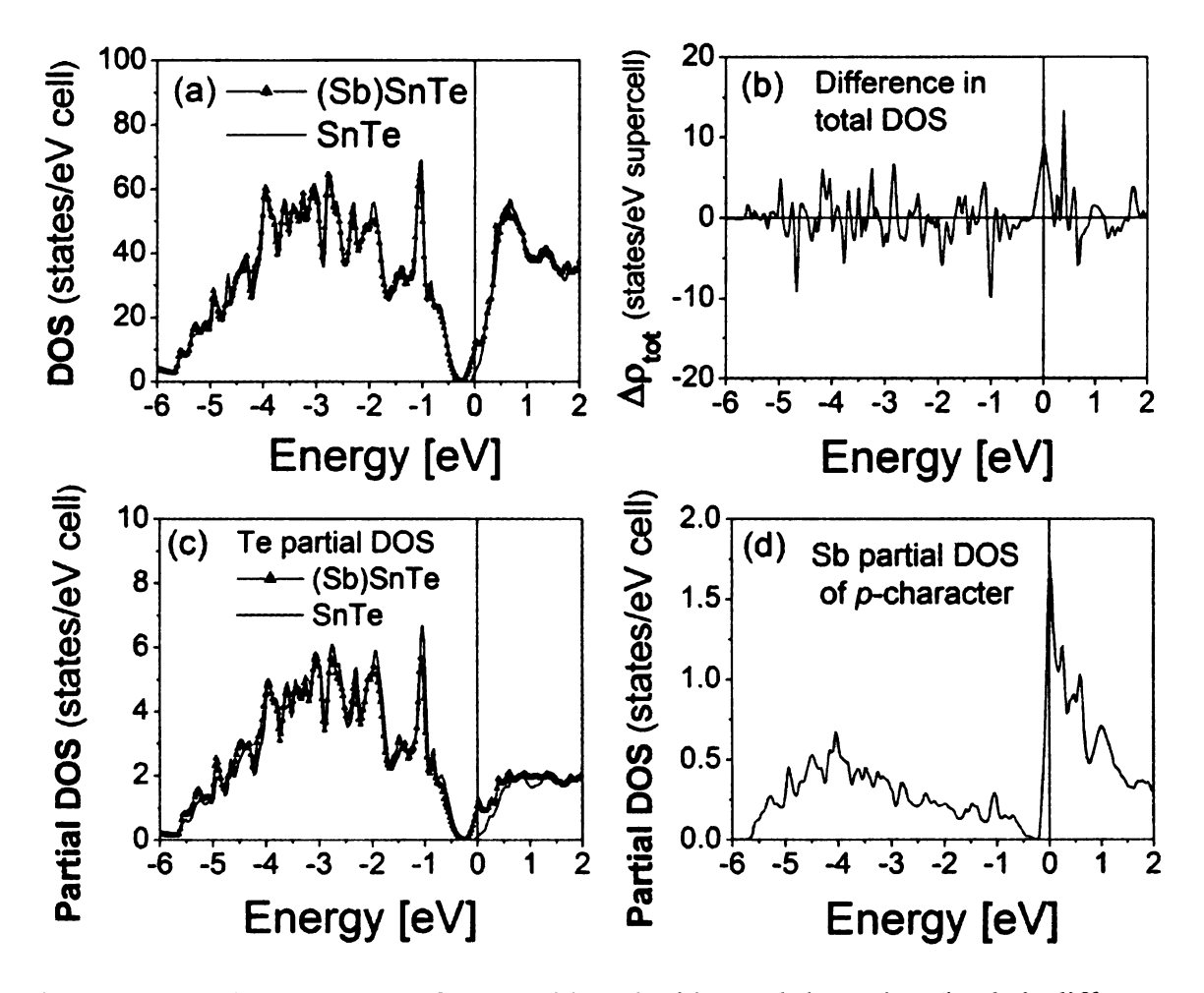


Figure 4.7 (a) The total DOS of SnTe with and without Sb impurity, (b) their difference  $\Delta \rho_{\text{tot}}$ , (c) partial DOS per Te associated with nearest neighbor Te atoms, and (d) Sb partial DOS of *p*-character. The Fermi energy of SnTe with Sb impurity is at the energy origin (0 eV).

### 4.3.6 In impurity in SnTe

Indium impurity in IV-VI semiconductors have been known to exhibit anomalous behavior.[42, 43] For example it act as n-type in PbTe and p-type in SnTe. We discussed in details in the previous chapter, the anomalous behavior of In impurity in PbTe and we presented a new picture in order to understand these anomalous behavior. Indium metal is nominally trivalent, and hence when In replaces a divalent Sn, one expects an n-type donor. This assumes that the number of states in the Te-p band does not change when an In impurity is present. If the In s-state is strongly bound and lies below the valence pband, then In will behave as an acceptor because it gives only one electron to the Te-p band instead of needed two. Results for In impurity in SnTe shows that the deep defect states are resonant states near the top of the SnTe valence band (act as p-type). In contrast, in PbTe these states lie in the band-gap region and can act as n-type by thermally exciting an electron from the DDS to the conduction band. This difference in the position of the deep defect states between SnTe and the PbTe is extremely subtle but explains the experimental anomalies seen in the case of In impurities (act as n-type in PbTe and p-type in SnTe). These subtle differences can only be seen in a fully self consistent ab initio study. We find that the orbital nature of the resonant state near the top of the valence band is a hybridization of the s states of the In with the p state of the neighboring six Te atoms. We show, in Fig. 4.8 (a)-(d), the total and partial DOS of SnTe with and without In impurity, the difference  $\Delta \rho_{tot}$ , and s character of the partial DOS of In impurity. These general features are very similar to those for In in PbTe.

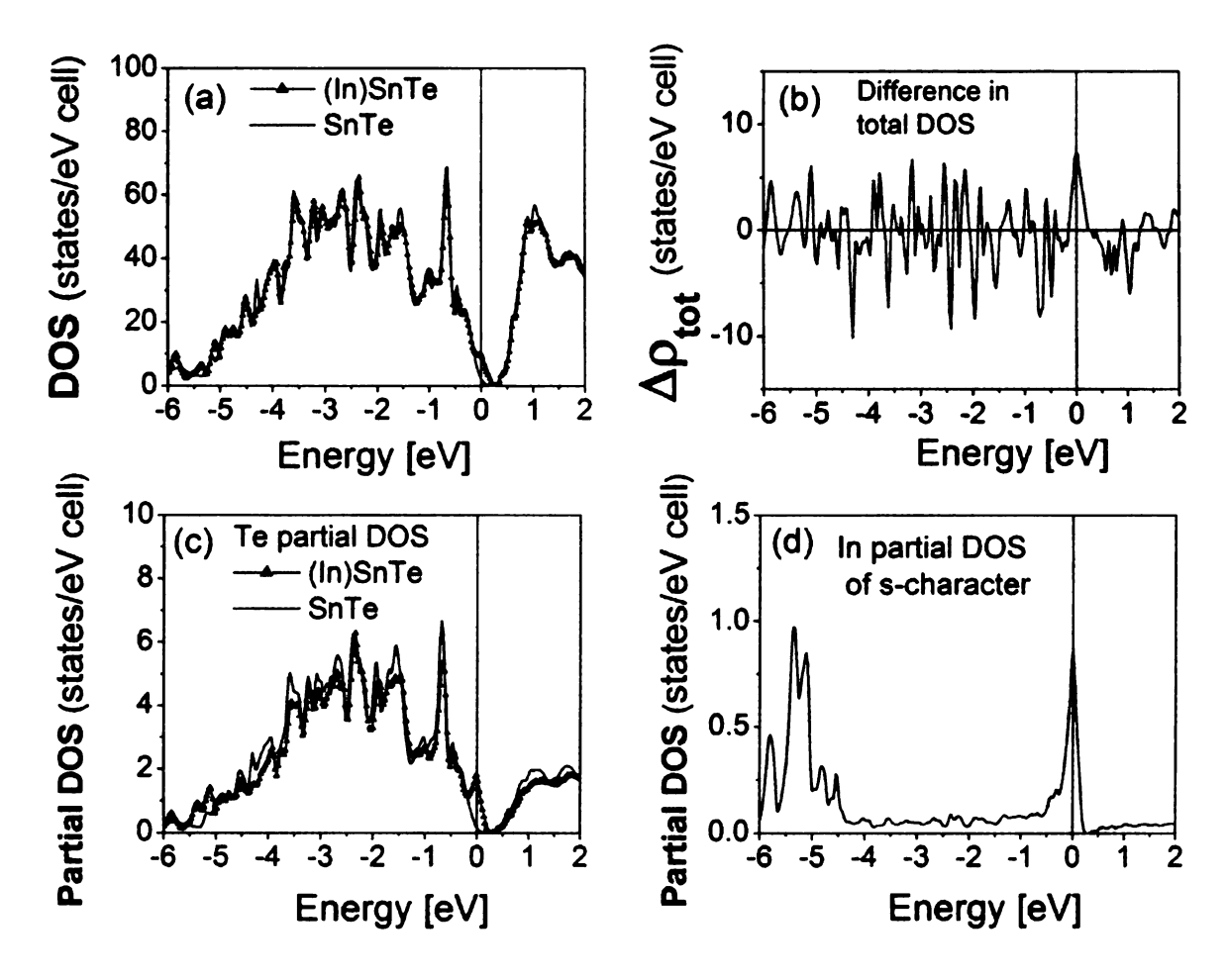


Figure 4.8 (a) The total DOS of SnTe with and without In impurity, (b) their difference  $\Delta \rho_{\text{tot}}$ , (c) partial DOS per Te associated with nearest neighbor Te atoms, and (d) In partial DOS of s-character. The Fermi energy of SnTe with In impurity is at the energy origin (0 eV).

# 4.4 Summary

In summary my *ab initio* electronic structure calculations in  $RSn_{2n-1}Te_{2n}$ , n=16, R = a vacancy, Ag, Cd, Sb, and In show that when a Sn atom is substituted by R, the DOS of the valence and conduction bands get strongly perturbed. There are significant changes near the band gap region. Sn vacancy causes very little change near the bottom of the conduction band DOS whereas there is an increase in the DOS near the top of the valence band. Te vacancy on the other hand creates new states in the band gap region and near the

bottom of the conduction band. Ag impurities perturb the valence band states due to the Ag d-states hybridizing with the Te p bands. The difference in the total DOS with and without Ag impurity shows a small peak near the top of the valance band. Sb impurity shows resonant states near the bottom of the SnTe conduction band. Results for In impurity shows that, unlike PbTe, the deep defect states in SnTe are resonant states near the top of the valence band. In PbTe these deep defect states lie in the band-gap region (act as n-type). This fundamental difference in the position of the deep defect states in SnTe and PbTe explains the experimental anomalies seen in the case of In impurities (act as n-type in PbTe and p-type in SnTe).[13, 87]

# Energy and Temperature dependence of relaxation time and Wiedemann-Franz law in PbTe

### 5.1 General Introduction

As discussed in Chapter 1, the efficiency of thermoelectric (TE) energy conversion depends on the transport coefficients of the constituent materials through the figure of merit (FOM)  $ZT = \sigma S^2 T/(\kappa_l + \kappa_{el,J})$  where  $\sigma$  is the electrical conductivity and S is the thermopower (Seebeck coefficient) [9]. The quantity in the denominator is the thermal conductivity; it is given by the sum of contributions from the electronic carriers at constant electrical current  $\vec{J}(\kappa_{el,J})$  and the lattice contribution  $\kappa_l$ . Z has units of inverse temperature, so it is generally quoted as ZT, with T the absolute operating temperature of the TE device [9]. TE devices are usually made from narrow band gap semiconductors.

Several calculations of the transport coefficients of PbTe and related systems have been reported over the years [52, 95, 102, 104, 105]. These calculations have been performed using Boltzmann transport equation [123] within the energy-dependent relaxation time ( $\tau$ ) approximation and the nonparabolic Kane model for energy dispersion  $\varepsilon_{\vec{k}}$  vs  $\vec{k}$ . [133] The energy and temperature dependence of different scattering mechanisms were incorporated in these calculations. Depending on the temperature, different scattering mechanisms (from impurities, acoustic and optical phonons) contribute to the

relaxation time. These earlier works did not explore the relationship between the energy and temperature dependence of the effective relaxation rate and the T-dependence of  $\sigma$ ,  $\kappa_{el,J}$  and  $\kappa_{el,E}$ . Also the validity of using WF law [123] to estimate electronic thermal conductivity at high temperatures has been questioned in the literature [104], but it is still widely used to estimate the lattice thermal conductivity from the total experimental thermal conductivity. The lattice thermal conductivities estimated this way are turning out to be very small, well below the so called alloy limit. [136] This reduction has been attributed to the enhanced phonon scattering from the nanostructures present in the samples. Thus to have a more definite picture one must critically examine the use of WF law. Furthermore the difference between constant  $\vec{J}$  and constant  $\vec{E}$  electronic thermal conductivities in PbTe has not been addressed properly although the fact that the experimentally measured electronic thermal conductivity  $\kappa_{el}$  appearing in the expression for ZT is  $\kappa_{el,J} \equiv L\sigma T$ , and the modified Lorentz number L is different from  $L_0$  is well known. [104, 122]

In this chapter we address these issues by focusing on (1) a careful analysis of the energy and T dependence of  $\tau$  to develop a simple scaling form, (2) understanding the relation between the energy dependence of  $\tau$  and the T dependence of  $\sigma$ , S, and the power factor  $(\sigma S^2)$ , and (3) finding out the difference between  $\kappa_{el,J}$  and  $\kappa_{el,E}$  and to reexamine the validity of WF law  $\kappa_{el} \equiv \kappa_{el,E} = L_0 \sigma T$ , where the Lorentz number  $L_0 = 2.45 \times 10^{-8} W\Omega/K$ .

The arrangement of this chapter is as follows. In Sec. 2, I describe the transport coefficients using the Boltzmann transport equation and define the transport function. In Sec. 3, I briefly review the non-parabolic Kane model for the energy band dispersion. In

Sec. 4, I describe the transport coefficients calculated using in the Kane model. In Sec. 5, I describe the total relaxation time and different scattering mechanisms contributing to this quantity in PbTe. In Sec. 6, I discuss the total thermal conductivity  $\kappa$  and the different types of electronic contributions. In Sec. 7, I present and discuss our results and finally, I give a brief summary in Sec. 8.

## 5.2 Transport Coefficients using the Boltzmann Transport Equation

The charge carriers in a metal or a semiconductor move under an applied external field and temperature gradient. We consider the situation where the carriers are accelerated by the fields, but lose their extra energy and momentum by scattering from lattice waves (phonons) and impurities. A standard method used to deal with this problem is to use Boltzmann transport equation. [123] This equation states that in a steady state situation, at any point in space  $\vec{r}$  and for any value of the electronic wave vector  $\vec{k}$ , the net rate of change of  $f_{\vec{k}}(\vec{r},t)$  is zero, where  $f_{\vec{k}}(\vec{r},t)$  is the probability that an electron (hole) of wave vector  $\vec{k}$  is at point  $\vec{r}$  in the crystal. Then:

$$\left[\frac{\partial f_{\vec{k}}}{\partial t}\right]_{diff} + \left[\frac{\partial f_{\vec{k}}}{\partial t}\right]_{field} + \left[\frac{\partial f_{\vec{k}}}{\partial t}\right]_{scatt} = 0 , \qquad (5.1)$$

where the different contributions to the change are due to diffusion, external fields and scattering. Eq. 5.1 is valid for the steady-state, not for equilibrium  $\left(f_{\vec{k}}(\vec{r},t)=f_{\vec{k}}^{0}(\vec{r})\right)$  which holds in the absence of external fields,  $f_{\vec{k}}^{0}(\vec{r})$  is the equilibrium single particle Fermi distribution function, where  $\vec{r}$  dependence comes through the local temperature  $T(\vec{r})$ . It is given by:

$$f_{\vec{k}}^{0}(\vec{r}) = \frac{1}{exp\left(\frac{\varepsilon_{\vec{k}} - \mu}{k_{B}T(\vec{r})}\right) + 1},$$
(5.2)

where  $\varepsilon_{\vec{k}}$  is the energy,  $\mu$  is the chemical potential,  $k_B$  is the Boltzmann constant. For simplicity we will ignore the spin index and assume that each state  $\vec{k}$  is two-fold spin degenerate since we do not consider magneto transport.

Assuming Liouville's theorem of the invariance of volume occupied in phase space, one finds that the number of carriers in the neighborhood of  $\vec{r}$  at time t is equal to those in neighborhood of  $\vec{r} - t\vec{v}_{\vec{k}}$  at time zero:

$$f_{\vec{k}}(\vec{r},t) = f_{\vec{k}}(\vec{r} - t\vec{v}_{\vec{k}},0). \tag{5.3}$$

The rate of change of the distribution function due to diffusion can then be written as:

$$\left[\frac{\partial f_{\vec{k}}}{\partial t}\right]_{diff} = -\frac{\partial \vec{r}}{\partial t}\frac{\partial f_{\vec{k}}}{\partial \vec{r}(T)} = -\vec{v}_{\vec{k}}\frac{\partial f_{\vec{k}}}{\partial T}\nabla T, \qquad (5.4)$$

using the definition of Fermi distribution function the derivative with respect to temperature in Eq. 5.4 can be rewritten as:

$$\frac{\partial f_{\vec{k}}}{\partial T} = \frac{exp\left(\frac{\varepsilon_{\vec{k}} - \mu}{k_B T}\right)}{\left[exp\left(\frac{\varepsilon_{\vec{k}} - \mu}{k_B T}\right) + 1\right]^2} \frac{\varepsilon_{\vec{k}} - \mu}{k_B T^2} = \left(-\frac{\partial f_{\vec{k}}}{\partial \varepsilon_{\vec{k}}}\right) \frac{\varepsilon_{\vec{k}} - \mu}{T} , \qquad (5.5)$$

and then the rate of change of the distribution function due to diffusion is given by:

$$\left[\frac{\partial f_{\vec{k}}}{\partial t}\right]_{diff} = \left(-\frac{\partial f_{\vec{k}}}{\partial \varepsilon_{\vec{k}}}\right) \frac{\varepsilon_{\vec{k}} - \mu}{T} \vec{v}_{\vec{k}} (-\nabla T). \tag{5.6}$$

By analogy to Eq. 5.3 we can apply Liouville's theorem in  $\vec{k}$ -space:

$$f_{\vec{k}}(\vec{r},t) = f_{\vec{k}-\vec{k}t}(\vec{r},0),$$
 (5.7)

considering only electric field  $\vec{E}$  as the external field, the time rate of change of Bloch wave vector  $\vec{k}$  is given by:

$$\hbar \dot{\vec{k}} = e \vec{E} \quad . \tag{5.8}$$

The velocity of the electron in the state  $\vec{k}$  is given by:

$$\hbar \vec{v}_{\vec{k}} = \frac{\partial \varepsilon_{\vec{k}}}{\partial \vec{k}} \,. \tag{5.9}$$

In Eq. 5.8 and 5.9, e is electronic charge, m is free electron mass, and  $\hbar = h/2\pi$  with h being the Planck constant. The rate of change of the distribution function due to the field can be written as:

$$\left[\frac{\partial f_{\vec{k}}}{\partial t}\right]_{field} = -\frac{\partial \vec{k}}{\partial t}\frac{\partial f_{\vec{k}}}{\partial \vec{k}} = -\dot{\vec{k}}\frac{\partial f_{\vec{k}}}{\partial \varepsilon_{\vec{k}}}\frac{\partial \varepsilon_{\vec{k}}}{\partial \vec{k}} = -\frac{e\vec{E}}{\hbar}\frac{\partial f_{\vec{k}}}{\partial \varepsilon_{\vec{k}}}\hbar\vec{v}_{\vec{k}} = e\left(-\frac{\partial f_{\vec{k}}}{\partial \varepsilon_{\vec{k}}}\right)\vec{v}_{\vec{k}}\vec{E}. \quad (5.10)$$

The effect of scattering on the change in the distribution function is more complicated. In this thesis the relaxation time approximation was considered. In the relaxation time approximation the rate of change of the distribution function due scattering is given by:

$$\left[\frac{\partial f_{\vec{k}}}{\partial t}\right]_{scatt.} = -\frac{f_{\vec{k}} - f_{\vec{k}}^0}{\tau_{\vec{k}}} = -\frac{g_{\vec{k}}}{\tau_{\vec{k}}},\tag{5.11}$$

where  $g_{\vec{k}}$  is the difference between the steady-state and equilibrium distribution functions, and  $\tau_{\vec{k}}$  is the relaxation time.

Using the Eq. 5.6, 5.10, and 5.11, the Boltzmann transport equation (Eq. 5.1) can be written as:

$$g_{\vec{k}} = e\left(-\frac{\partial f_{\vec{k}}}{\partial \varepsilon_{\vec{k}}}\right) \vec{v}_{\vec{k}} \tau_{\vec{k}} \vec{E} + \left(-\frac{\partial f_{\vec{k}}}{\partial \varepsilon_{\vec{k}}}\right) \frac{\varepsilon_{\vec{k}} - \mu}{T} \vec{v}_{\vec{k}} \tau_{\vec{k}} (-\nabla T). \tag{5.12}$$

In order to find the expressions for electrical conductivity tensor  $\vec{\sigma}$  and thermopower tensor  $\vec{S}$ , the microscopic and macroscopic Ohm's laws have to be used,

which relate the current density to the applied electric field and temperature gradient. The microscopic Ohm's law is given by:

$$\vec{J} = \frac{1}{V} \sum_{\vec{k}} e f_{\vec{k}} \vec{v}_{\vec{k}} = \frac{1}{V} \sum_{\vec{k}} e g_{\vec{k}} \vec{v}_{\vec{k}} , \qquad (5.13)$$

since

$$\sum_{\vec{k}} e f_{\vec{k}}^0 \vec{v}_{\vec{k}} = 0 \quad , \tag{5.14}$$

where V is the volume of the crystal in real space. From Eq. 5.12 and Eq. 5.13, the current density can be expressed as:

$$\vec{J} = \frac{1}{V} \sum_{\vec{k}} e^2 \left( -\frac{\partial f_{\vec{k}}}{\partial \varepsilon_{\vec{k}}} \right) \tau_{\vec{k}} \vec{v}_{\vec{k}} \vec{v}_{\vec{k}} \vec{E} + \frac{1}{V} \sum_{\vec{k}} e \left( -\frac{\partial f_{\vec{k}}}{\partial \varepsilon_{\vec{k}}} \right) \frac{\varepsilon_{\vec{k}} - \mu}{T} \tau_{\vec{k}} \vec{v}_{\vec{k}} \vec{v}_{\vec{k}} (-\nabla T), \quad (5.15)$$

$$\vec{J} = \frac{1}{V} \sum_{\vec{k}} e^2 \left( -\frac{\partial f_{\vec{k}}}{\partial \varepsilon_{\vec{k}}} \right) \tau_{\vec{k}} \vec{v}_{\vec{k}} \vec{v}_{\vec{k}} \left( \vec{E} + \frac{1}{eT} \frac{\sum_{\vec{k}} \left( -\frac{\partial f_{\vec{k}}}{\partial \varepsilon_{\vec{k}}} \right) (\varepsilon_{\vec{k}} - \mu) \tau_{\vec{k}} \vec{v}_{\vec{k}} \vec{v}_{\vec{k}}}{\sum_{\vec{k}} \left( -\frac{\partial f_{\vec{k}}}{\partial \varepsilon_{\vec{k}}} \right) \tau_{\vec{k}} \vec{v}_{\vec{k}} \vec{v}_{\vec{k}}} (-\nabla T) \right)$$
(5.16)

The macroscopic Ohm's law in the presence of an external electric field  $\vec{E}$  and temperature gradient  $\nabla T$  is given by:

$$\vec{j} = \vec{\sigma}\vec{E} + \vec{\sigma}\vec{S}(-\nabla T) = \vec{\sigma}(\vec{E} + \vec{S}(-\nabla T)). \tag{5.17}$$

Direct comparison of the two Ohm's laws in Eq. 5.16 and 5.17 gives the expressions for the electrical conductivity and thermopower tensor:

$$\vec{\sigma} = \frac{e^2}{V} \sum_{\vec{k}} \left( -\frac{\partial f_{\vec{k}}}{\partial \varepsilon_{\vec{k}}} \right) \tau_{\vec{k}} \vec{v}_{\vec{k}} \vec{v}_{\vec{k}} , \qquad (5.18)$$

$$\vec{S} = (\vec{\sigma})^{-1} \vec{A} \quad , \tag{5.19}$$

where  $\vec{A}$  is given by:

$$\vec{A} = \frac{e}{VT} \sum_{\vec{k}} \left( -\frac{\partial f_{\vec{k}}}{\partial \varepsilon_{\vec{k}}} \right) \left( \varepsilon_{\vec{k}} - \mu \right) \tau_{\vec{k}} \vec{v}_{\vec{k}} \vec{v}_{\vec{k}}. \tag{5.20}$$

Analogous to the current density equations, the heat current density equations for  $\vec{J}_Q$  can be written as:

$$\vec{J}_Q = \frac{1}{V} \sum_{\vec{k}} f_{\vec{k}} (\varepsilon_{\vec{k}} - \mu) \vec{v}_{\vec{k}} = \frac{1}{V} \sum_{\vec{k}} g_{\vec{k}} (\varepsilon_{\vec{k}} - \mu) \vec{v}_{\vec{k}} , \qquad (5.21)$$

$$\vec{J}_Q \equiv \vec{\sigma} \, \vec{S} \, T \vec{E} + \vec{\kappa}_{el,E} (-\nabla T) \quad , \tag{5.22}$$

where  $\vec{k}_{el,E}$  is the electronic thermal conductivity tensor at constant  $\vec{E}$  field (evaluated at  $\vec{E}=0$ ). Direct comparison of the two heat current density equations gives the expression for the electronic thermal conductivity tensor at constant  $\vec{E}$  field ( $\vec{E}=0$ ):

$$\vec{\kappa}_{el,E} = \frac{1}{VT} \sum_{\vec{k}} \left( -\frac{\partial f_{\vec{k}}}{\partial \varepsilon_{\vec{k}}} \right) \left( \varepsilon_{\vec{k}} - \mu \right)^2 \tau_{\vec{k}} \vec{v}_{\vec{k}} \vec{v}_{\vec{k}} . \tag{5.23}$$

At constant current density  $\vec{J}$  ( $\vec{J} = 0$ ) (Eq. 5.17), the heat density  $\vec{J}_Q$  is given by:

$$\vec{J}_Q \equiv \left[ \vec{\kappa}_{el,E} - \vec{\sigma} (\vec{S})^2 T \right] (-\nabla T) . \tag{5.24}$$

The electronic thermal conductivity at constant current density  $\vec{J}$  (evaluated at  $\vec{J} = 0$ )  $\vec{\kappa}_{el,J}$ , is given by:

$$\vec{\kappa}_{el,I} = \vec{\kappa}_{el,E} - \vec{\sigma}(\vec{S})^2 T . \tag{5.25}$$

Normally in metals and highly degenerate semiconductors the second term on the right hand side of Eq. 5.25 is quite small and  $\vec{\kappa}_{el,J} \approx \vec{\kappa}_{el,E}$ . But as we will see later, for semiconductors of current interest they can differ dramatically.

# 5.3 Nonparabolic Kane Model for Energy Dispersion

In this section I will briefly describe the Kane model for the band structure of PbTe valid near the band extrema which occur at the L point of the fcc Brillouin Zone (BZ), see Fig. 3.1. In narrow band-gap semiconductors (i.e., lead chalcogenides) the energy region of interest of an electron as measured from the band edge is comparable to the band gap  $E_g$ . Because of this, the dependence of the energy on crystal momentum is non-parabolic and the effective masses are functions of energy. The nonparabolic Kane model was introduced [133] to describe the deviations from the quadratic dependence of energy on the crystal momentum. In this model, the longitudinal effective mass  $m_l$  and the transverse effective mass  $m_l$  depend only on the interaction between the lowest conduction band and the highest valence band and the contributions of the other bands are assumed to be small. Here longitudinal and transverse are defined parallel and perpendicular to the vector joining the center of the BZ to the L point (see Fig. 3.1). From now on we will confine ourselves to the conduction band and electron type transport. For a simple parabolic model the energy dispersion can be expressed as:

$$\varepsilon_{\vec{k}} = \frac{\hbar^2}{2} \left( \frac{2k_t^2}{m_t} + \frac{k_l^2}{m_l} \right),\tag{5.26}$$

where  $\varepsilon_{\vec{k}}$  is the energy, and  $k_l$  and  $k_t$  are the magnitudes of the longitudinal and transverse components of  $\vec{k}$ , measured from the band extrema. In the Kane model the energy dispersion is given by:

$$\varepsilon_{\vec{k}} \left( 1 + \frac{\varepsilon_{\vec{k}}}{E_g} \right) = \frac{\hbar^2}{2} \left( \frac{2k_t^2}{m_t} + \frac{k_l^2}{m_l} \right), \tag{5.27}$$

In this model the effective masses and the mass anisotropy coefficient of electrons and holes are equal. The constant energy surfaces are ellipsoids, and  $m_l$  and  $m_t$  have the same energy dependence.

# 5.4 Transport Coefficients in the Kane Model

In order to calculate the transport coefficients we have to compute different quantities appearing in Eqs. 5.18, 5.19, and 5.23, which include the carrier velocity  $\vec{v}_{\vec{k}}$  and the relaxation time  $\tau_{\vec{k}}$ . For the sake of completeness we will derive the expression for the transport coefficient following the methods used by Ravich *et. al.* [125] and work of Bilc *et. al.* [52] For this, we change the discrete sums over  $\vec{k}$  into integrals, the carrier velocity  $\vec{v}_{\vec{k}}$  is calculated using the Kane model for energy dispersion, and the relaxation time expressions for different scattering mechanisms are obtained within Kane model. These expressions are given in the section 5.5. [106, 107, 124, 125]

PbTe systems have cubic symmetry. Therefore, the components  $\sigma_{\mu\nu}$  and  $S_{\mu\nu}$  of the electrical conductivity and thermopower tensors can be expressed as:

$$\sigma_{\mu\nu} = \delta_{\mu\nu}\sigma,\tag{5.28}$$

$$S_{\mu\nu} = \delta_{\mu\nu} S,\tag{5.29}$$

where  $\sigma$  and S are related to the trace of  $\overrightarrow{\sigma}$  and  $\overrightarrow{S}$  tensors and they are given by:

$$\sigma = \frac{1}{3} Tr \vec{\sigma} \,, \tag{5.30}$$

$$S = \frac{1}{3}Tr\vec{S}\,, ag{5.31}$$

For cubic system,  $Tr\vec{\sigma}$  and  $Tr\vec{S}$  are related to  $\vec{v}_{\vec{k}}\vec{v}_{\vec{k}} = \vec{v}_{\vec{k}}^2$  terms.

The Kane model energy (Eq. 5.27) contains two types of effective masses and in order to simplify the calculations the fallowing substitutions can be made:

$$k_t^2 = \frac{m_t}{m_d'} k_t'^2 \,, \tag{5.32}$$

$$k_l^2 = \frac{m_l}{m_d'} k_l'^2, (5.33)$$

where  $m'_d$  is a scaling mass parameter (see Eq. 5.57 for its definition)

Using the new variables  $k'_{l}$  and  $k'_{t}$ , Eq. 5.27 can be written as:

$$\varepsilon_{k'} \left( 1 + \frac{\varepsilon_{k'}}{E_g} \right) = \frac{\hbar^2}{2m'_d} \left( 2k'_t{}^2 + k'_l{}^2 \right) \equiv \frac{\hbar^2}{2m'_d} k'^2. \tag{5.34}$$

In terms of the new variable  $\vec{k}'$  the expressions for  $\vec{\sigma}$  and  $\vec{S}$  are:

$$\vec{\sigma} = \frac{e^2}{V} \sum_{\vec{k}_{\prime}} \left( -\frac{\partial f_{\vec{k}_{\prime}}}{\partial \varepsilon_{\vec{k}_{\prime}}} \right) \tau_{\vec{k}_{\prime}} \vec{v}_{\vec{k}_{\prime}} \vec{v}_{\vec{k}_{\prime}}, \qquad (5.35)$$

$$\vec{S} = (\vec{\sigma})^{-1} \vec{A}, \tag{5.36}$$

where  $\vec{A}$  is given by:

$$\vec{A} = \frac{e}{VT} \sum_{\vec{k}'} \left( -\frac{\partial f_{\vec{k}'}}{\partial \varepsilon_{\vec{k}'}} \right) \left( \varepsilon_{\vec{k}'} - \mu \right) \tau_{\vec{k}'} \vec{v}_{\vec{k}'} \vec{v}_{\vec{k}'}. \tag{5.37}$$

Changing the sums into integrals, Eq. 5.36 for thermopower becomes:

$$\vec{S} = \frac{1}{eT} \frac{\int_0^\infty \left( -\frac{\partial f_{\vec{k}'}}{\partial \varepsilon_{\vec{k}'}} \right) (\varepsilon_{\vec{k}'} - \mu) \tau_{\vec{k}'} \vec{v}_{\vec{k}'} \vec{v}_{\vec{k}'} d^3 \vec{k}'}{\int_0^\infty \left( -\frac{\partial f_{\vec{k}'}}{\partial \varepsilon_{\vec{k}'}} \right) \tau_{\vec{k}'} \vec{v}_{\vec{k}'} \vec{v}_{\vec{k}'} d^3 \vec{k}'}$$
(5.38)

Using Eq. 5.34, the infinitesimal unit volume in reciprocal space  $d^3\vec{k}'$  can be expressed as:

$$d^{3}\vec{k}' = 4\pi k'^{2}dk' = 4\pi \frac{2^{\frac{1}{2}}m_{d}^{\frac{3}{2}}}{\hbar^{3}} \left[\varepsilon \left(1 + \frac{\varepsilon}{E_{g}}\right)\right]^{\frac{1}{2}} \left(1 + \frac{2\varepsilon}{E_{g}}\right) d\varepsilon, \qquad (5.39)$$

where we have dropped the suffix for the carrier energy  $\varepsilon_{\vec{k}}$ . The carrier velocity in Eq. 5.9 is given by:

$$\hbar \vec{v}_{\vec{k}'} = \frac{1}{\hbar} \frac{\partial \varepsilon_{\vec{k}'}}{\partial \vec{k}'} = \frac{\hbar}{m_d'} \frac{\vec{k}'}{1 + \frac{2\varepsilon}{E_g}}.$$
 (5.40)

Using the above equation, the  $v_{\vec{k}}^2 = \vec{v}_{\vec{k}}$ ,  $\vec{v}_{\vec{k}}$ , term in the transport equations can be expressed as:

$$v_{\vec{k}'}^2 = \frac{2}{m_d'} \frac{\varepsilon \left(1 + \frac{\varepsilon}{E_g}\right)}{\left(1 + \frac{2\varepsilon}{E_g}\right)^2} \ . \tag{5.41}$$

Substituting Eq. 5.39 and 5.41 into Eq. 5.38 and using Eqs. 5.28 and 5.31, the thermopower along any one of the cubic axis  $S_{xx}(S_{xx}=S)$  becomes:

$$\vec{S} = \frac{1}{eT} \frac{\int_0^\infty \left(-\frac{\partial f}{\partial \varepsilon}\right) (\varepsilon - \mu) \left[\varepsilon \left(1 + \frac{\varepsilon}{E_g}\right)\right]^{\frac{3}{2}} \left(1 + \frac{2\varepsilon}{E_g}\right)^{-1} \tau_{\varepsilon} d\varepsilon}{\int_0^\infty \left(-\frac{\partial f}{\partial \varepsilon}\right) \left[\varepsilon \left(1 + \frac{\varepsilon}{E_g}\right)\right]^{\frac{3}{2}} \left(1 + \frac{2\varepsilon}{E_g}\right)} \tau_{\varepsilon} d\varepsilon$$
(5.42)

where the relaxation time  $\tau_{\varepsilon}$  depends on energy. Since S depends on the ratio of the two integrals (Eq. 5.38) the spin and band degeneracy ( $\gamma$ ) factors (see the following paragraph for a definition) cancel out in Eq. 5.38 and 5.42.

Taking into account the spin degeneracy and the band degeneracy  $\gamma$ , the expression for the electrical conductivity  $\vec{\sigma}$  can be rewritten as:

$$\vec{\sigma} = \frac{2\gamma e^2}{V} \sum_{\vec{k}_{\prime}} \left( -\frac{\partial f_{\vec{k}_{\prime}}}{\partial \varepsilon_{\vec{k}_{\prime}}} \right) \tau_{\vec{k}_{\prime}} \vec{v}_{\vec{k}_{\prime}} \vec{v}_{\vec{k}_{\prime}} = \frac{2\gamma e^2}{V} \frac{V}{(2\pi)^3} \int_0^{\infty} \left( -\frac{\partial f_{\vec{k}_{\prime}}}{\partial \varepsilon_{\vec{k}_{\prime}}} \right) \tau_{\vec{k}_{\prime}} \vec{v}_{\vec{k}_{\prime}} \vec{v}_{\vec{k}_{\prime}} d^3 \vec{k}' \quad , \quad (5.43)$$

and using Eq. 5.39 and 5.41,  $Tr \vec{\sigma}$  can be expressed as:

$$Tr \, \vec{\sigma} = 2\gamma e^2 \frac{(2m_d')^{\frac{1}{2}}}{\pi^2 \hbar^3} \int_0^\infty \left( -\frac{\partial f}{\partial \varepsilon} \right) \left[ \varepsilon \left( 1 + \frac{\varepsilon}{E_g} \right) \right]^{\frac{3}{2}} \left( 1 + \frac{2\varepsilon}{E_g} \right)^{-1} \tau_{\varepsilon} \, d\varepsilon. \tag{5.44}$$

Again for cubic system the conductivity along any one of the cubic axis  $\sigma_{xx}(\sigma_{xx} = \sigma)$  is given by:

$$\sigma = \frac{2}{3} \gamma e^2 \frac{(2m_d')^{\frac{1}{2}}}{\pi^2 \hbar^3} \int_0^\infty \left( -\frac{\partial f}{\partial \varepsilon} \right) \left[ \varepsilon \left( 1 + \frac{\varepsilon}{E_g} \right) \right]^{\frac{3}{2}} \left( 1 + \frac{2\varepsilon}{E_g} \right)^{-1} \tau_{\varepsilon} \, d\varepsilon . \tag{5.45}$$

The expression for the electronic thermal conductivity at constant  $\vec{E}$  field ( $\vec{E} = 0$ )  $\vec{\kappa}_{el,E}$  can be rewritten as:

$$\vec{\kappa}_{el,E} = \frac{2\gamma}{VT} \sum_{\vec{k}'} \left( -\frac{\partial f_{\vec{k}'}}{\partial \varepsilon_{\vec{k}'}} \right) \left( \varepsilon_{\vec{k}'} - \mu \right)^2 \tau_{\vec{k}'} \vec{v}_{\vec{k}'} \vec{v}_{\vec{k}'} , \qquad (5.46)$$

$$\vec{\kappa}_{el,E} = \frac{2\gamma}{VT} \frac{V}{(2\pi)^3} \int_0^\infty \left( -\frac{\partial f_{\vec{k}}}{\partial \varepsilon_{\vec{k}}} \right) \left( \varepsilon_{\vec{k}}, -\mu \right)^2 \tau_{\vec{k}}, \vec{v}_{\vec{k}}, \vec{v}_{\vec{k}}, d^3 \vec{k}', \tag{5.47}$$

and using Eq. 5.39 and 5.41,  $Tr \vec{\kappa}_{el,E}$  can be expressed as:

$$Tr \, \vec{\kappa}_{el,E} = \frac{2\gamma}{T} \frac{(2m_d')^{\frac{1}{2}}}{\pi^2 \hbar^3} \int_0^\infty \left( -\frac{\partial f}{\partial \varepsilon} \right) (\varepsilon - \mu)^2 \left[ \varepsilon \left( 1 + \frac{\varepsilon}{E_g} \right) \right]^{\frac{3}{2}} \left( 1 + \frac{2\varepsilon}{E_g} \right)^{-1} \tau_{\varepsilon} \, d\varepsilon \,\, , (5.48)$$

the electronic thermal conductivity at constant  $\vec{E}$  field  $(\vec{E}=0)$   $\vec{\kappa}_{el,E}$  along the x-axis  $(\vec{\kappa}_{el,E})_{xx} \left( (\vec{\kappa}_{el,E})_{xx} = \kappa_{el,E} \right)$  becomes:

$$\kappa_{el,E} = \frac{2\gamma}{3T} \frac{(2m_d')^{\frac{1}{2}}}{\pi^2 \hbar^3} \int_0^\infty \left(-\frac{\partial f}{\partial \varepsilon}\right) (\varepsilon - \mu)^2 \left[\varepsilon \left(1 + \frac{\varepsilon}{E_g}\right)\right]^{\frac{3}{2}} \left(1 + \frac{2\varepsilon}{E_g}\right)^{-1} \tau_{\varepsilon} d\varepsilon . \quad (5.49)$$

The three transport coefficients for the cubic system can be expressed in terms of a single transport function  $\Sigma(\varepsilon)$ :

$$\sigma = e^2 \int_0^\infty \left( -\frac{\partial f}{\partial \varepsilon} \right) \Sigma(\varepsilon) \, d\varepsilon \quad , \tag{5.50}$$

$$S = \frac{e}{T\sigma} \int_0^\infty \left( -\frac{\partial f}{\partial \varepsilon} \right) \Sigma(\varepsilon) \left( \varepsilon - \mu \right) d\varepsilon \quad , \tag{5.51}$$

$$\kappa_{el,E} = \frac{1}{T} \int_0^\infty \left( -\frac{\partial f}{\partial \varepsilon} \right) \Sigma(\varepsilon) (\varepsilon - \mu)^2 d\varepsilon , \qquad (5.52)$$

where  $\Sigma(\varepsilon) = D(\varepsilon)v_{\varepsilon}^2\tau_{\varepsilon}$ , and  $D(\varepsilon)$  is the density of states, defined as  $D(\varepsilon) = \sum_{\vec{k},\sigma} \delta(\varepsilon - \varepsilon_{\vec{k},\sigma})$ .

The concentration of carriers n can be written as:

$$n = \frac{2\gamma}{V} \sum_{\vec{k}'} f_{\vec{k}'} = \frac{2\gamma}{V} \int \frac{d^3 \vec{k}'}{exp\left(\frac{\varepsilon_{\vec{k}'} - \mu}{k_B T}\right) + 1} , \qquad (5.53)$$

and using Eq. 5.53 the concentration n can be expressed as:

$$n = \frac{2^{\frac{1}{2}}}{\pi^2 \hbar^3} \gamma m'_{d}^{\frac{3}{2}} \int_{0}^{\infty} \frac{\left[\varepsilon \left(1 + \frac{\varepsilon}{E_g}\right)\right]^{\frac{1}{2}} \left(1 + \frac{2\varepsilon}{E_g}\right) d\varepsilon}{\exp\left(\frac{\varepsilon - \mu}{k_B T}\right) + 1} \,. \tag{5.54}$$

The expression  $\gamma m'_d^{3/2}$  is defined as:

$$m_d^{3/2} = \gamma m_d^{3/2} , (5.55)$$

where  $m_d$  is called density of state effective mass because it takes into account the degeneracy of the conduction band. The relation between scaling mass parameter  $(m'_d)$ , the density of state effective mass  $m_d$  and longitudinal and transverse effective masses  $(m_l, m_t)$  can now be deduced using the Eqs. 5.32, 5.33 and the following equation:

$$d^{3}\vec{k} = d^{3}\vec{k}', (5.56)$$

which sets the equality between the infinitesimal volumes in reciprocal space. Using this we find the scaling mass parameter  $m'_d = (m_l m_t^2)^{1/3}$ . From Eq. 5.55, we therefore obtain:

$$m_d = \gamma^{2/3} m'_d = \gamma^{2/3} (m_l m_t^2)^{1/3}$$

#### 5.5 Relaxation Time in the Kane Model

Different scattering mechanisms of charge carriers in lead chalcogenides have been extensively discussed in many papers [106, 107, 124, 125]. It is found that the dominant scattering mechanism contributing to  $\tau$  are from point defects and thermal phonons. Their relative contributions to the scattering processes are summarized below.

At low temperatures (liquid helium), charge carriers are scattered mostly by charged vacancies. At low densities  $n \le 5 \times 10^{18} \ cm^{-3}$ , scattering by Coulomb potential of the vacancies dominates, whereas for high carrier densities  $n \ge 10^{19} \ cm^{-3}$ , the Coulomb potential gets screened out and scattering by the short range potential of vacancies dominates. As the temperature increases, the relative importance of the charged vacancies decreases and scattering by thermal phonons increases. For temperatures above 300 K, scattering by acoustic phonons and optical phonons (both polar and deformation potential coupling) contribute mostly to the relaxation time. The expressions for the dominant contributions to the relaxation time within the Kane model were first worked out by Ravich and collaborators and later extended by Zayachuck and Freik *et al.* [106, 107, 124, 125]. They are available in the literature. Therefore we give here only the final expressions for different scattering mechanisms, discuss the fundamental parameters involved, and analyze their relative significance for PbTe systems.

(i) Deformation potential of acoustic phonons  $(\tau_a)$ 

$$\tau_a = \frac{\tau_{0,a}(T) \left(\varepsilon + \frac{\varepsilon^2}{E_g}\right)^{-\frac{1}{2}}}{\left(1 + 2\frac{\varepsilon}{E_g}\right) [(1 - A)^2 - B]} , \qquad (5.58)$$

$$A = \frac{\frac{\varepsilon}{E_g} (1 - K_a)}{\left(1 + 2\frac{\varepsilon}{E_g}\right)} , \qquad (5.59)$$

$$B = \frac{8\frac{\varepsilon}{E_g} \left(1 + \frac{\varepsilon}{E_g}\right) K_a}{3\left(1 + 2\frac{\varepsilon}{E_g}\right)^2} , \qquad (5.60)$$

$$\tau_{0,a}(T) = \frac{2\pi\hbar^4 C_l}{E_{ac}^2 K_B T (2m_{d0})^{\frac{3}{2}}},$$
(5.61)

where  $E_{ac}$  is the acoustic deformation potential coupling constant for the conduction band,  $C_l$  is a combination of elastic constants,  $K_a$  is the ratio of the acoustic deformation potential coupling constants for the valence and conduction bands  $K_a = E_{av}/E_{ac}$  with the values  $K_a = 1$  for *n*-type PbTe and  $K_a = 1.5$  for *p*-type PbTe, and  $m_{d0}$  is the density of states effective mass for a single ellipsoid ( $\gamma = 1$ ), i.e.  $m_{d0} = m'_d$ .

## (ii) Deformation potential of optical phonons $(\tau_o)$

$$\tau_o = \frac{\tau_{0,o}(T) \left(\varepsilon + \frac{\varepsilon^2}{E_g}\right)^{-\frac{1}{2}}}{\left(1 + 2\frac{\varepsilon}{E_g}\right) [(1 - A)^2 - B]} , \qquad (5.62)$$

$$A = \frac{\frac{\varepsilon}{E_g} (1 - K_o)}{\left(1 + 2\frac{\varepsilon}{E_g}\right)},$$
(5.63)

$$B = \frac{8\frac{\varepsilon}{E_g} \left(1 + \frac{\varepsilon}{E_g}\right) K_o}{3\left(1 + 2\frac{\varepsilon}{E_g}\right)^2} , \qquad (5.64)$$

$$\tau_{0,o}(T) = \frac{2\hbar^2 a^2 \rho (\hbar \omega_0)^2}{\pi E_{0c}^2 K_B T (2m_{d0})^{\frac{3}{2}}},$$
(5.65)

where a is the PbTe lattice constant,  $\rho$  is the PbTe density,  $\omega_0$  is the frequency of the optical phonons,  $K_o$  is the ratio of the optical deformation potential coupling constants for valance and conduction bands,  $K_o = E_{ov}/E_{oc}$ , which are taken to be the same as for the acoustic phonons,  $K_a$ .

(iii) Polar scattering by optical phonons  $(\tau_{po})$ 

$$\tau_{po} = \frac{\left(\varepsilon + \frac{\varepsilon^2}{E_g}\right)^{\frac{1}{2}} F^{-1}}{e^2 (2m_{d0})^{\frac{1}{2}} K_B T (\epsilon_{\infty}^{-1} - \epsilon_0^{-1}) \left(1 + 2\frac{\varepsilon}{E_g}\right)},$$
 (5.66)

$$F = 1 - \delta \ln(1 + \delta^{-1}) - \frac{2\frac{\varepsilon}{E_g} \left(1 + \frac{\varepsilon}{E_g}\right)}{\left(1 + 2\frac{\varepsilon}{E_g}\right)^2} \left[1 - 2\delta + 2\delta^2 \ln(1 + \delta^{-1})\right], \tag{5.67}$$

$$\delta = (2kr_0)^{-2} \,, \tag{5.68}$$

where  $\epsilon_0$  and  $\epsilon_\infty$  are the static and high frequency dielectric constants, k is the carrier wave vector and  $r_0$  is the screening length of the optical phonons. The parameters k and  $r_0$  are given by:

$$k^2 = \frac{2m_{d0}\left(\varepsilon + \frac{\varepsilon^2}{E_g}\right)}{\hbar^2} , \qquad (5.69)$$

$$r_0^{-2} = \frac{2^{\frac{5}{2}} e^2 m_d^{\frac{3}{2}}}{\pi \hbar^3 \epsilon_{\infty}} \binom{0}{L_1^{\frac{1}{2}}}, \tag{5.70}$$

where  ${}^{n}L_{l}^{m}$  is the generalized Fermi integral:

$${}^{n}L_{l}^{m}(\mu, E_{g}) = \int_{0}^{\infty} \left(-\frac{\partial f}{\partial \varepsilon}\right) \varepsilon^{n} \left[\varepsilon \left(1 + \frac{\varepsilon}{E_{g}}\right)\right]^{m} \left(1 + \frac{2\varepsilon}{E_{g}}\right)^{l} d\varepsilon. \tag{5.71}$$

(iv) Short range deformation potential of vacancies  $(\tau_{\nu})$ 

$$\tau_{\nu} = \frac{\tau_{0,\nu}(T) \left(\varepsilon + \frac{\varepsilon^2}{E_g}\right)^{-\frac{1}{2}}}{\left(1 + 2\frac{\varepsilon}{E_g}\right) [(1 - A)^2 - B]} , \qquad (5.72)$$

$$A = \frac{\frac{\varepsilon}{E_g} (1 - K_v)}{\left(1 + 2\frac{\varepsilon}{E_g}\right)} , \qquad (5.73)$$

$$B = \frac{8\frac{\varepsilon}{E_g} \left(1 + \frac{\varepsilon}{E_g}\right) K_{\nu}}{3\left(1 + 2\frac{\varepsilon}{E_g}\right)^2} , \qquad (5.74)$$

$$\tau_{0,\nu}(T) = \frac{\pi \hbar^4}{U_{\nu c}^2 m_{d0} (2m_{d0})^{\frac{1}{2}} N_{\nu}} , \qquad (5.75)$$

where  $N_{\nu}$  is the vacancy density,  $K_{\nu}$  is the ratio of the short range deformation potential coupling constants of vacancies for valence and conduction bands,  $K_{\nu} = U_{\nu\nu}/U_{\nu c}$  which are taken to be the same as for acoustic phonons,  $K_a$ .

# (v) Coulomb potential of vacancies $(\tau_c)$

$$\tau_{c} = \frac{\varepsilon_{0}^{2} (2m_{d0})^{\frac{1}{2}} \left(\varepsilon + \frac{\varepsilon^{2}}{E_{g}}\right)^{\frac{3}{2}}}{\pi (Ze^{2})^{2} N_{v} [ln(1+\xi) - \xi/(1+\xi)] \left(1 + 2\frac{\varepsilon}{E_{g}}\right)},$$
(5.76)

$$\xi = (2kr_v)^{-2} \tag{5.77}$$

where Ze is the vacancy charge, and  $r_v$  is the screening radius of the vacancy potential given by:

$$r_{\nu}^{-2} = \frac{4\pi e^2}{\epsilon_0} D(\mu), \tag{5.78}$$

$$D(\mu) = \frac{2^{\frac{1}{2}} (m_{d0})^{\frac{3}{2}}}{\pi^2 \hbar^3} \left(\mu - \frac{\mu^2}{E_g}\right)^{\frac{1}{2}} \left(1 + 2\frac{\mu}{E_g}\right), \tag{5.79}$$

 $D(\mu)$  being the density of states at the chemical potential.

The total scattering relaxation time ( $\tau_{\varepsilon} \equiv \tau_{tot}$ ) is expressed as:

$$\frac{1}{\tau_{tot}} = \frac{1}{\tau_a} + \frac{1}{\tau_o} + \frac{1}{\tau_{po}} + \frac{1}{\tau_v} + \frac{1}{\tau_c}.$$
 (5.80)

The parameters used to calculate the relaxation time were taken from Ref. [106] where the transport data were fitted in the temperature range 300K < T < 900K. They are given in Table 5.1. Experimentally, one finds that the energy gap  $E_g$  and the density of states effective mass  $m_d$  are temperature dependent. [126] This comes from strong electron-phonon coupling. Following the work of Bilc et. al. [52], we have incorporated the T-dependent  $E_g$  and  $m_d$  using the experimental data in all our calculations. It turns out that the temperature dependence of  $m_d$  is very important to get a good agreement between theoretical and measured values of the transport coefficients  $\sigma$  and S [52]. Experimentally, it is found that  $E_g$  increases linearly with temperature for  $T \le 400K$  and above 400K, it remains constant. The temperature dependence of the band gap  $E_g$ [126] can be approximately given as

$$E_g = 0.19 + (0.42 \times 10^{-3})T$$
 for  $T \le 400 K$ , (5.81)

$$E_g = 0.358$$
 for  $T > 400 K$ . (5.82)

The temperature dependence of the density of states effective mass  $m_d$  comes primarily through the temperature dependence of the transverse effective mass  $m_t$  and this is taken from experiment [127],

$$\frac{m_t}{m} = 0.02459 + (8.659341 \times 10^{-5})T, \tag{5.83}$$

where m is the bare electron mass.

Parameter	Unit of measurement	Value	
$m_l/m$		0.24	
$\epsilon_0$		400	
$oldsymbol{\epsilon}_{\infty}$		32.6	
$C_{l}$	$N/m^2$	$0.71 \times 10^{11}$	
$\hbar\omega_0$	eV	0.0136	
а	Å	6.461	
ho	g/cm <sup>3</sup>	8.24	
Z		0.14	
$E_{ac}$	eV	15	
$N_{ u}$	cm <sup>-3</sup>	2.5×10 <sup>19</sup>	
$E_{oc}$	eV	15	
$U_{ u c}$	Erg cm <sup>3</sup>	3×10 <sup>-34</sup>	
$K_a$ , $K_o$ , $K_v$ for $n$ -type		1.0	
$K_a$ , $K_o$ , $K_v$ for $p$ -type		1.5	

Table 5.1 Parameters used to calculate the relaxation times for PbTe. [52, 106]

Before discussing the detail results of our present study we make a few brief comments on the work of Bhandari and Rowe [104] and Bilc et al. [52] Bhandari et al. considered the deformation potential of acoustic phonon as the dominant scattering mechanism ( $\tau_a$ ) at room temperature although they claimed that scattering by polar optical modes was not insignificant. On the otherhand, Bilc et al. [52] focused on the high temperature transport coefficients (but only  $\sigma$  and S) and included all the scattering contributions. The latter authors did not explicitly explore the energy and T-dependence of the relaxation time and how they contributed to the T-dependence of  $\sigma$  and S. In this thesis we do so.

In Table 5.2, we give the contribution of each scattering mechanism to the scattering rate for different temperatures ( $T \ge 300K$ ) and different carrier energy  $\varepsilon$ . Scattering by acoustic phonons and optical phonons (both polar and deformation

potential coupling) make significant contributions at temperatures above 300 K, whereas the contribution of the short range deformation potential of vacancies ( $\tau_v$ ) and Coulomb potential of vacancies ( $\tau_c$ ) at ( $T \geq 300K$ ) are weak and insignificant. At low energy ( $\varepsilon \ll 0.10 \text{ eV}$ ), the polar scattering by optical phonons ( $\tau_{po}$ ) dominates the scattering mechanism, whereas in the energy range ( $0.05 \geq \varepsilon \geq 0.30$ ) scattering by acoustic phonons and optical phonons (both polar and deformation potential coupling) are comparable. At high energy ( $\varepsilon > 0.30 \text{ eV}$ ), the acoustic phonon scattering is the dominant scattering mechanism. At constant temperature, the contribution of the scattering by the deformation potential of acoustic ( $\tau_a$ ) and optical ( $\tau_o$ ) phonons increase with increasing energy  $\varepsilon$ ; in contrast the contribution of polar scattering by optical phonons ( $\tau_{po}$ ) decreases with increasing energy  $\varepsilon$ .

In Fig. 5.1, we plot the inverse scattering relaxation time associated with the three dominant scattering mechanisms ( $\tau_a$ ,  $\tau_o$  and  $\tau_{po}$ ) as a function of carrier energy  $\varepsilon$ , at different T (300K, 600K, and 900K) for electron carrier density  $n = 5 \times 10^{19} \ cm^{-3}$ . The chemical potential  $\mu$  was calculated for each T using Eq. 5.54 (T-dependence of  $\mu$  will be discussed latter in section 5.7). Also, we have drawn ( $-\partial f_0/\partial \varepsilon$ ) about the  $\mu$ -values, in order to see the range of energy  $\varepsilon$  that contribute to the transport coefficients (as discussed before is Sec. 5.4) and hence check the scattering mechanisms that contribute in this range. We can see from Fig 5.1 that, in energy range ( $0 < \varepsilon < 0.3$ ), it is not appropriate to ignore the deformation potential ( $1/\tau_o$ ) and polar ( $1/\tau_{po}$ ) scattering by optical phonons to get a proper understanding of the transport coefficients and subsequent comparison with experiment (see Ref. 52). At room temperature T = 300K where  $\mu = 0.146$  eV,  $\tau_a$  and  $\tau_{po}$  are comparable and  $\tau_o$  is not insignificant.

	$1/ au_a$ (10 <sup>11</sup> sec <sup>-1</sup> )	$1/ au_o$ $(10^{11}\mathrm{sec}^{-1})$	$1/ au_{po}$ (10 <sup>11</sup> sec <sup>-1</sup> )	$1/\tau_v \ (10^{11}  {\rm sec}^{-1})$	$1/ au_C \ (10^{11}  { m sec}^{-1})$	ε (eV)
300 K	14.90	7.12	75.70	0.996	0.25	
600 K	45.10	21.50	198.00	1.51	0.22	0.02
900 K	129.00	61.70	315.00	2.88	0.09	
300 K	36.60	17.50	56.60	2.44	0.02	
600 K	109.00	51.80	136.00	3.62	0.02	0.10
900 K	246.00	118.00	221.00	5.48	0.02	
300 K	63.60	30.30	48.60	4.24	0.01	
600 K	183.00	87.20	112.00	6.10	0.01	0.20
900 K	400.00	191.00	186.00	8.91	0.01	
300 K	97.10	46.30	45.70	6.48	0.004	
600 K	272.00	130.00	103.00	9.08	0.004	0.30
900 K	587.00	280.00	172.00	13.10	0.004	

Table 5.2 Inverse of the relaxation time of different scattering mechanisms in PbTe for different temperatures T and different carrier energies  $\varepsilon$ .

Increasing temperature reduces  $\mu$  and hence shifts the  $(-\partial f_0/\partial \varepsilon)$  peak towards lower energy, as shown from Fig. 5.1 (b) and (c). This increases the contribution of the polar scattering by optical phonons to the net scattering rate.

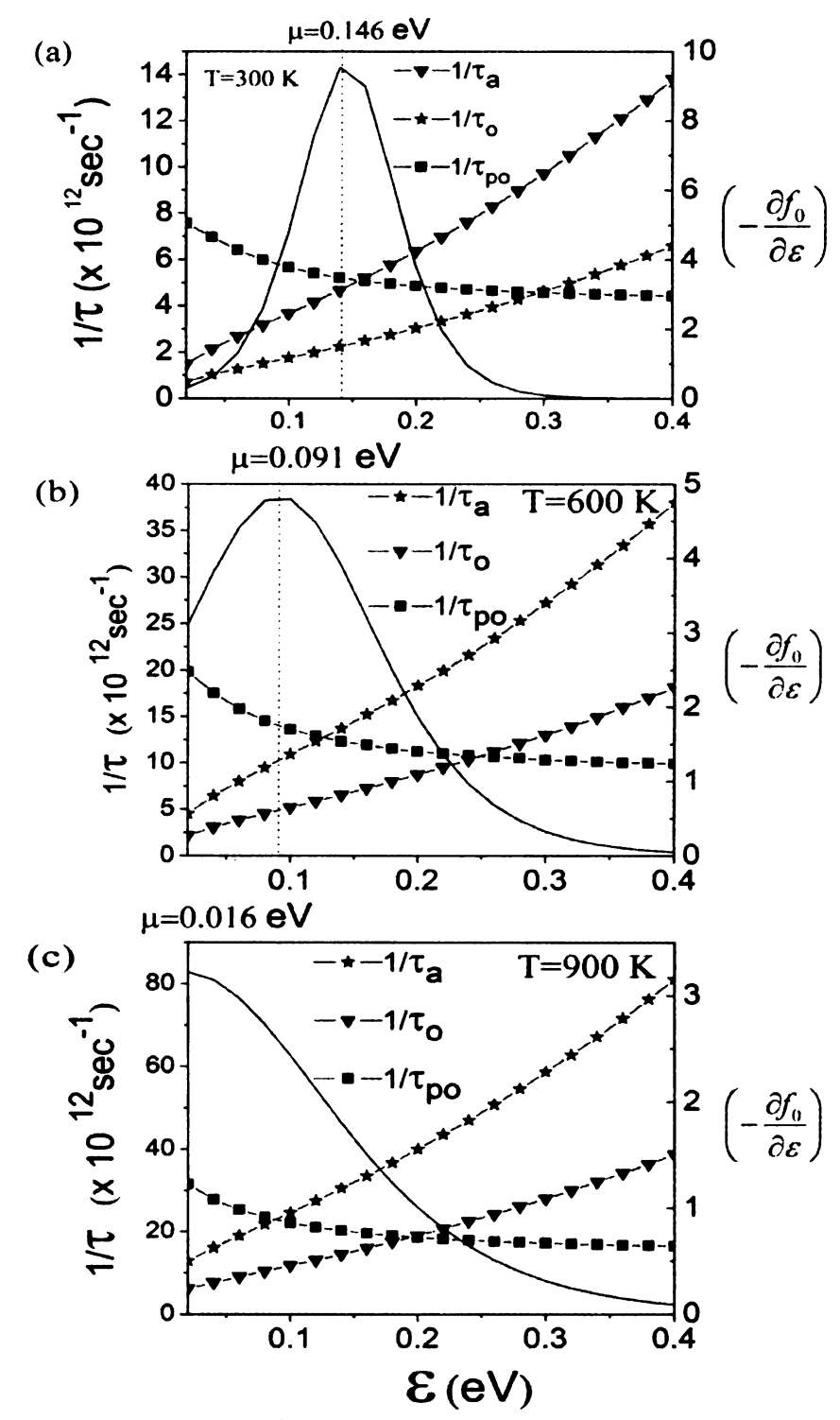


Figure 5.1 Energy dependence of the inverse of the relaxation time of the three dominant scattering mechanisms ( $\tau_a$ ,  $\tau_o$  and  $\tau_{po}$ ) in PbTe for electron carrier density  $n = 5 \times 10^{19}$  cm<sup>3</sup> at different temperatures (a) 300K (b) 600K (c) 900 K. The smooth curves gives the  $(-\partial f_0/\partial \varepsilon)$  indicating the energy region contributing to the transport at different temperatures.

## 5.6 The Electronic Thermal Conductivity

We will now evaluate the electronic thermal conductivity using the T and  $\varepsilon$  dependence of  $\tau$ , as discussed in Sec. 5.5. But before this we would like to make some general observation. The total thermal conductivity  $\kappa_{tot}$  is usually defined and measured at zero electric current and is a sum of the lattice contribution  $\kappa_l$  and the electronic part at zero current  $\kappa_{el,J}$  and is given by (using Eqs. 5.25, 5.28 and 5.29) and  $\kappa_{\mu\nu} = \kappa \delta_{\mu\nu}$  for different types of electronic thermal conductivity

$$\kappa_{tot} = \kappa_l + \kappa_{el,l} \tag{5.84}$$

$$= \kappa_l + \kappa_{el.E} - T\sigma S^2 \,. \tag{5.85}$$

This  $\kappa_{tot}$  appears in the definition of ZT. [9] Since the thermal conductivity is a positive quantity for a thermally stable system  $(\kappa_{e,J} \ge 0)$ , it is therefore necessary that  $\kappa_{el,E} \ge T\sigma S^2$ . The dimensionless figure of merit which is then given by

$$ZT = \frac{T\sigma S^2}{\kappa_l + \kappa_{el.E} - T\sigma S^2}$$
 (5.86)

can be optimized by manipulating  $\kappa_{el,E}$ . Sofo and Mahan [96] found that for a given lattice thermal conductivity  $\kappa_l$ , the best thermoelectric is when  $\kappa_{el,E} = T\sigma S^2$ , which is equivalent to  $\kappa_{el,J} = 0$ . If we look at Eqs. (5.50)-(5.52) this equality occurs when  $\Sigma(\varepsilon,T) = A\delta(\varepsilon-\varepsilon_0)$ , i.e. the energy and charge transport take place in a single energy channel,  $\varepsilon = \varepsilon_0$ , i.e. perfect energy filtering. Even in this case one has to adjust the chemical potential such that  $|\mu - \varepsilon_0| \approx 2.5k_BT$  to maximize ZT. In this case  $ZT \to \infty$  when the lattice thermal conductivity is ignored ( $\kappa_l = 0$ ). In a recent work Humphrey and Linke [137] have explored a similar energy filtering idea, but for an inhomogeneous system. They have shown that in the presence of a temperature gradient if one can

construct a graded thermoelectric such that the quantity  $\left(\frac{\varepsilon(\vec{r})-\mu}{k_BT(\vec{r})}\right)$  remains constant throughout the sample, then the energy and charge transport is adiabatic, which gives rise to perfect Carnot efficiency and this correspond to  $ZT=\infty$ , when the lattice thermal conductivity is ignored. The thermoelectric efficiency is given by [9]

$$\eta = \frac{T_{hot} - T_{cold}}{T_{hot}} \left( \frac{\sqrt{1 + ZT} - 1}{\sqrt{1 + ZT} + \frac{T_{cold}}{T_{hot}}} \right), \tag{5.87}$$

To achieve high efficiencies, high ZT materials and large temperature differences  $\Delta T = T_{hot} - T_{cold}$ , are needed ( $\eta \rightarrow \eta_{carnot} = \Delta T/T_{hot}$  when  $ZT \rightarrow \infty$ ).

#### 5.7 Results and Discussions

In order to calculate the electrical conductivity  $\sigma$ , S and  $\kappa_{el,E}$  for a given concentration n at different temperatures, Eqs. 5.42, 5.45, 5.49, and 5.53 have to be solved simultaneously, the common link being the chemical potential  $\mu$ . We used *Mathematica* program to solve these set of coupled equations.

As mentioned in the section 5.5 of this chapter, we have taken into account the temperature dependence of the energy gap  $E_g$  and the density of states effective mass  $m_d$  which are given in Eqs. 5.81, 5.82, and 5.83. For PbTe, as mentioned before, the gap occurs at the L point in the fcc BZ and  $\gamma = 4$ . At high concentrations,  $n \sim 10^{19} cm^{-3}$ , which are required for good thermoelectric, the n- or p-type PbTe can be described using a single (either conduction or valence) band model since for these concentrations, contributions to transport come primarily from one type of carrier. (Note: that for p-type

transport all transport equations have to be interpreted in terms of hole occupation function) Here we give the results for the n-type PbTe. Fig. 5.2 shows the temperature dependence of the chemical potential  $\mu$  for concentrations  $n = 5 \times 10^{19} cm^{-3}$  and  $n = 5 \times 10^{20} cm^{-3}$ . The change in  $\mu$  over the temperature range of 600 K is quite significant. This plays an important role in the observed T-dependence of  $\sigma$ , S and  $\kappa_{el,E}$  over this temperature range. Results of  $\sigma$  and S with a comparison with experimental values, taken from Ref. [128], are shown in Fig. 5.3. The parameters used to calculate  $\tau_{tot}$  were taken from Bilc et al's. work. [52]. Our theoretical results for  $\kappa_{el,E}$  and  $\kappa_{el,J}$  will be discussed in Sec. 5.9.

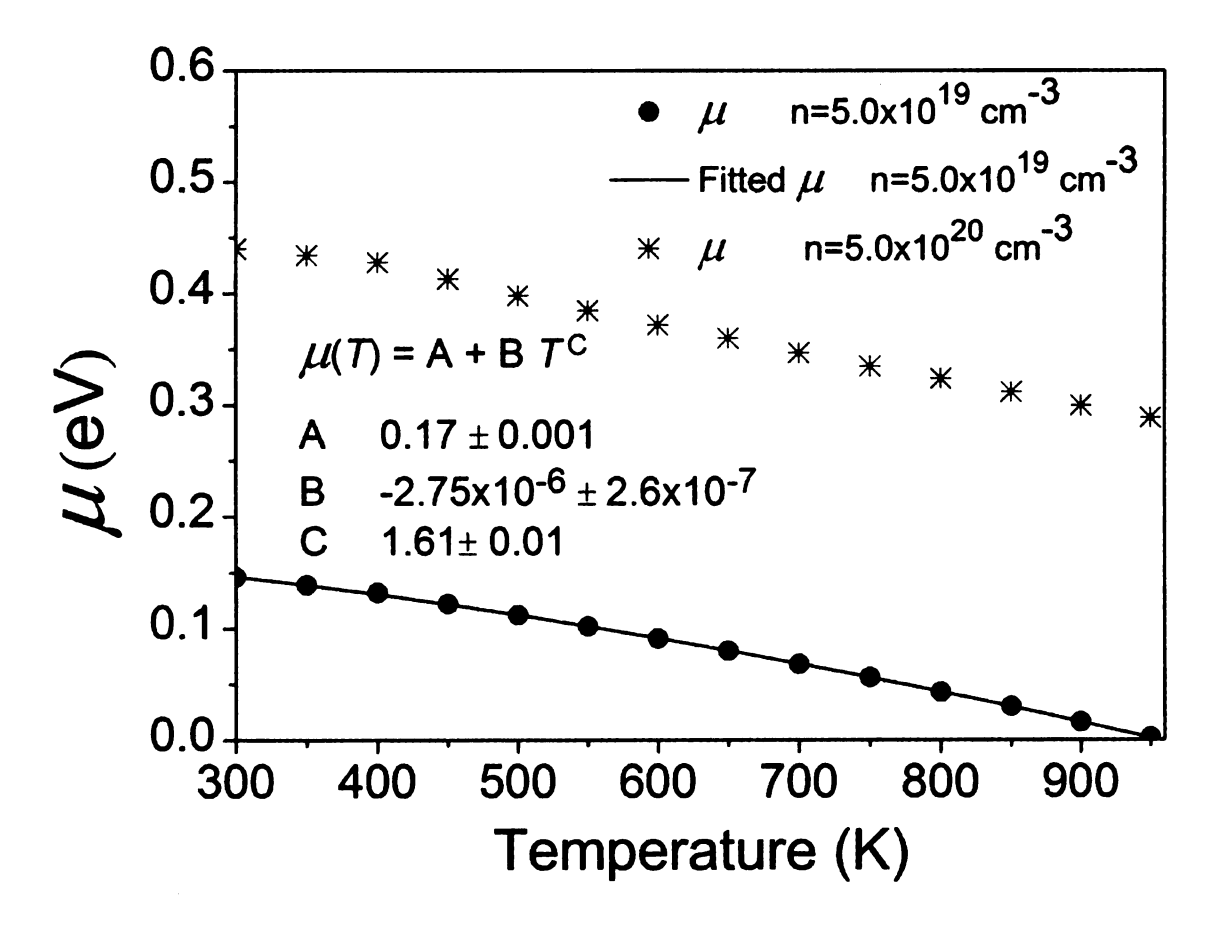


Figure 5.2 Temperature dependence of the chemical potential  $\mu$  for *n*-type PbTe at different concentrations  $n = 5 \times 10^{19}$  cm<sup>-3</sup> and  $n = 5 \times 10^{20}$  cm<sup>-3</sup>.

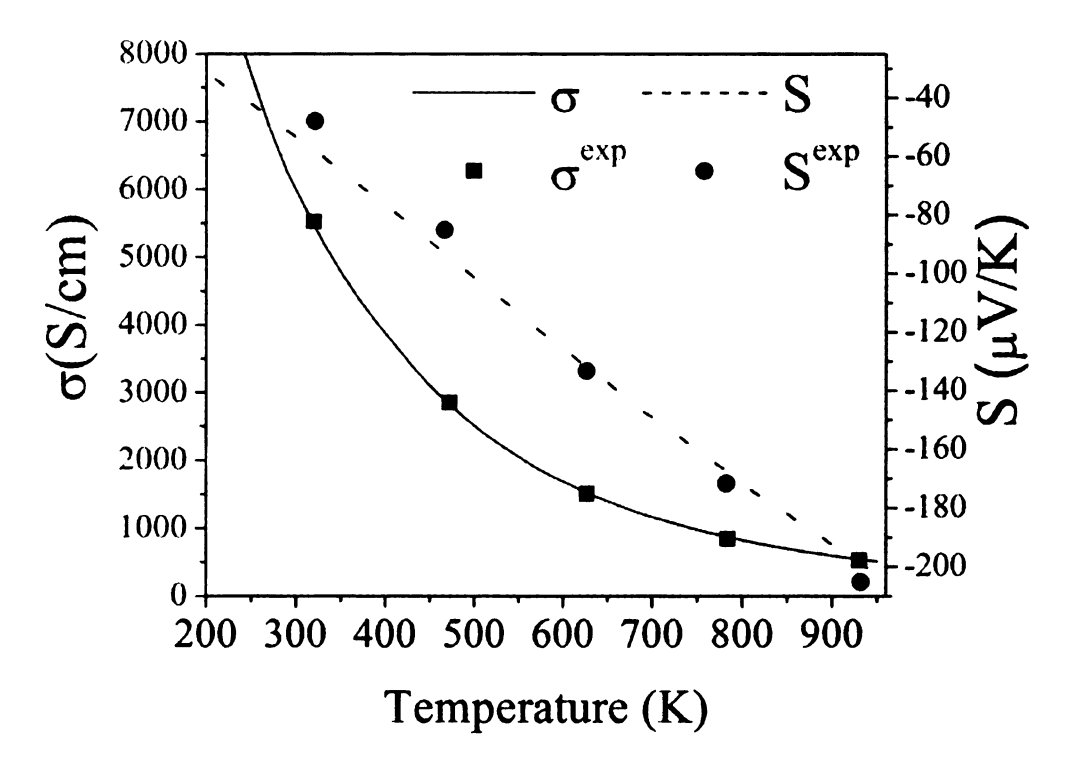


Figure 5.3 Temperature dependence of the electrical conductivity  $\sigma$  and thermopower S for n-type PbTe at concentration  $n = 5 \times 10^{19}$  cm<sup>-3</sup>. The experimental values are shown as solid points from Ref [128].

# 5.7.1 Energy and Temperature Dependence of the Relaxation time

In order to understand the temperature and energy dependence of the total relaxation time in PbTe we plot the total relaxation time  $\tau_{tot}$  (see Eq. 5.80) as a function of carriers energy  $\varepsilon$  for different temperatures. Fig. 5.4 shows the energy dependence of  $\tau_{tot}$  for deferent temperatures. As we can see, the relaxation time decreases with increasing  $\varepsilon$ , and decreases with increasing temperature for a given  $\varepsilon$ . We scaled  $\tau_{tot}$  for different temperatures in order to see how the scaled  $\tau_{tot}$  depends on  $\varepsilon$ . Fig. 5.5 shows that for different T, the energy dependence of  $\tau_{tot}$  is almost the same; therefore we fit  $\tau_{tot}(T=300, \varepsilon)$  to find the energy dependence of  $\tau_{tot}$  (see Fig. 5.6). After that it was straight forward to find the T dependent of the  $\tau_{tot}$  (see Fig. 5.7). The total relaxation time of PbTe can be approximated extremely well by a scaling function

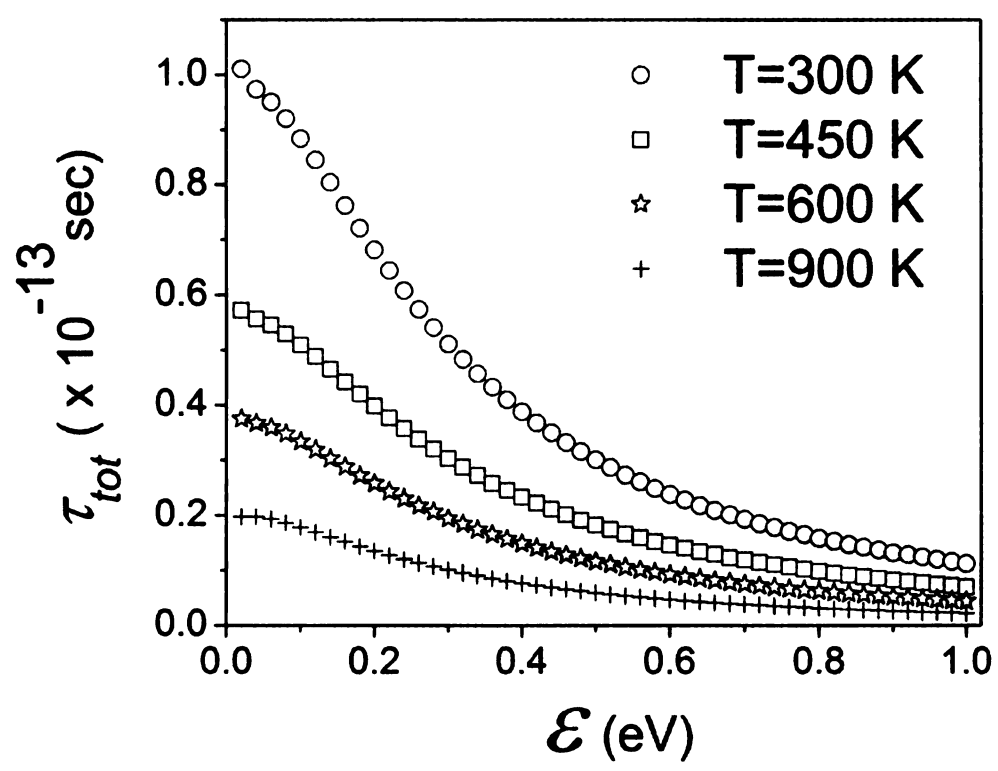


Figure 5.4 Energy dependence of the total relaxation time  $\tau_{tot}$ , calculated from Eq. 5.80, for *n*-type PbTe at concentration  $n = 5 \times 10^{19}$  cm<sup>-3</sup> for different temperatures.

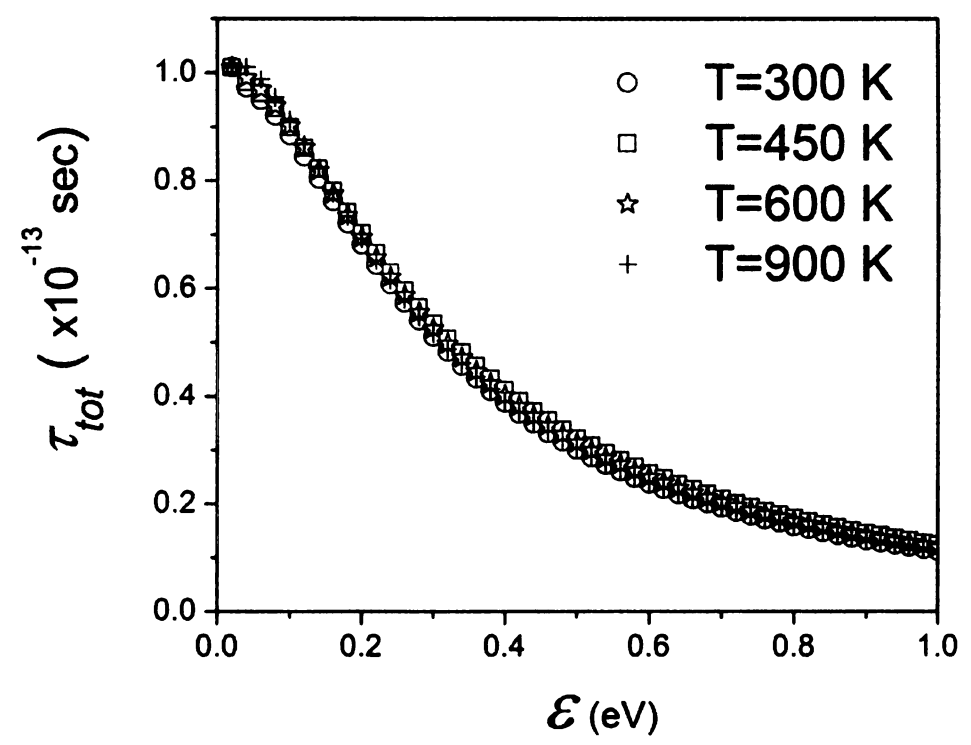


Figure 5.5 Energy dependence of the scaled (to 300K) total relaxation time  $\tau_{tot}$  at different temperatures.

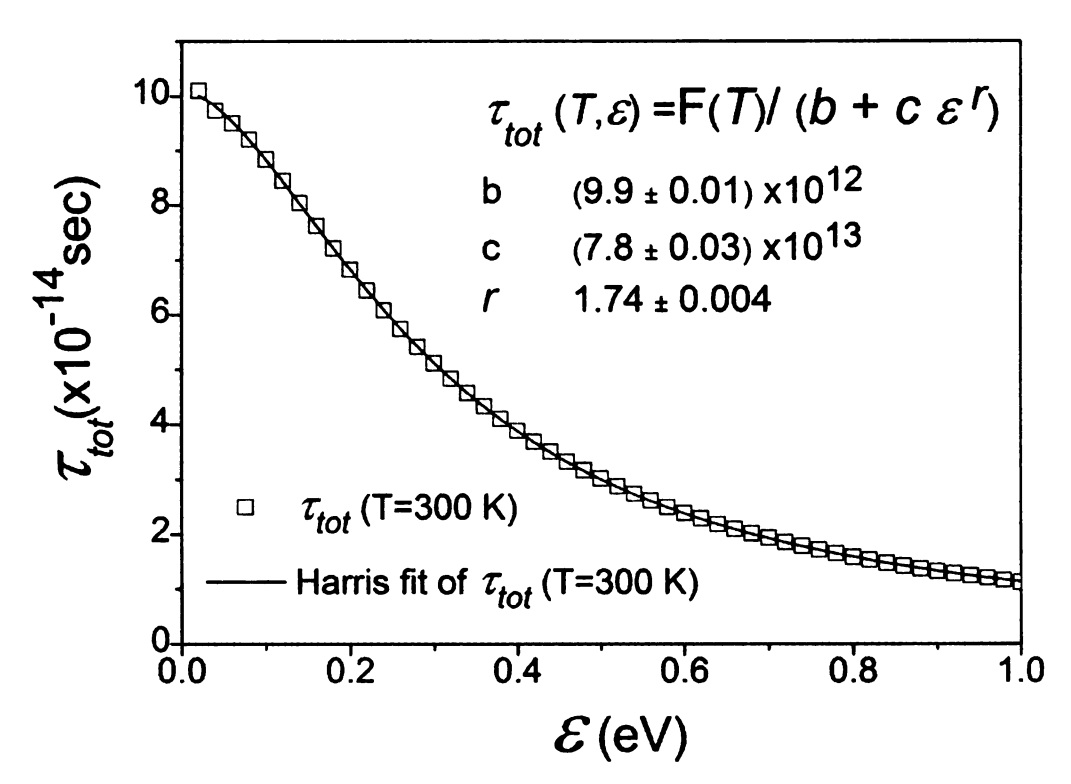


Figure 5.6 Energy dependence of the total relaxation time  $\tau_{tot}$  for T=300 K.

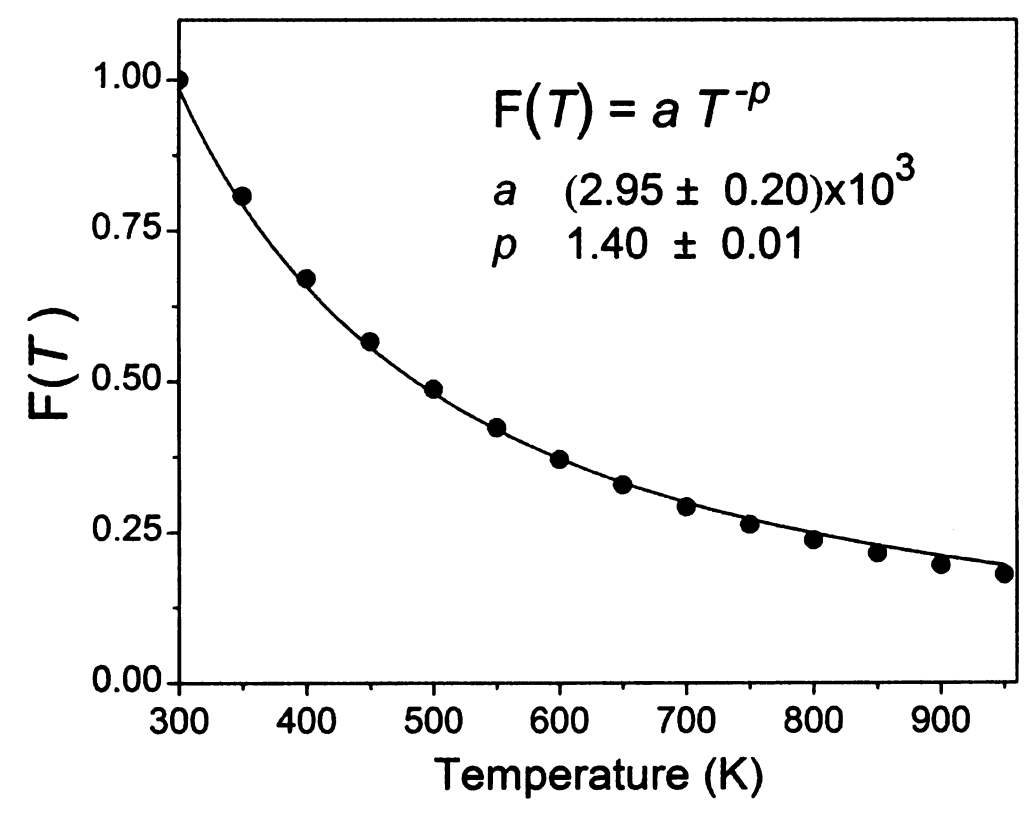


Figure 5.7 Temperature dependence of the total relaxation time  $\tau_{tot}$  at  $\varepsilon = 0.1$  eV.

$$\tau_{tot} = \frac{aT^{-p}}{(b + c\varepsilon^r)},\tag{5.88}$$

where a, b, c, p and r are the fitted parameters, which depend on the carrier concentration. We used this expression to check the calculated electrical conductivity  $\sigma$  and the thermopower S, (see Fig. 5.8 and Fig. 5.9). This expression of  $\tau_{tot}$  gives excellent agreement (within 5%) with the values of  $\sigma$  and S calculated directly from the scattering mechanisms.

To check how sensitive the electrical conductivity  $\sigma$  is to the energy dependence of  $\tau_{tot}$ , we plot  $\sigma$  for different values of the r parameter (see Eq. 5.88) as shown in Fig. 5.10. The absolute values of  $\sigma$  change with r. As r increases from 0 scattering in the energy range of interest (0.0-0.3 eV as discussed in Sec. 5.5) gets suppressed leading to an increase of  $\sigma$  for all T. However, after scaling  $\sigma$ , we notice that it is not sensitive to the energy dependence of  $au_{tot}$ . In order to understand why the temperature dependence of  $\sigma$ is so weekly dependent on the parameter r of Eq. 5.88, we look in detail the different physical quantities that give rise to the observed T-dependence. The scaling form for the total scattering time  $\tau_{tot}$  gives p = 1.4. This power law dependence comes from two sources,  $T^{-1}$  dependence from the phonon occupation number at high T  $(k_B T \gg \hbar \omega)$ ,  $\left[\tau^{-1} \sim \frac{k_B T}{\hbar \omega}\right]$  and a  $T^{-0.4}$  from the temperature dependence of the density of state through the parameter  $m_{d0}$  (see Sec. 5.5 for different phonon induced relaxation rates). The question is where the additional  $T^{-0.8}$  dependence of  $\sigma$  comes from: In order to find this, we made a simple calculation. We assumed  $\tau_{tot}$  to be constant and then calculated the Tdependence of  $\sigma$  coming from other sources. We find that  $\sigma \sim T^{-0.8}$ , the T-dependence of  $\mu$  playing a crucial role in this T-dependence. In this respect, PbTe at the doping

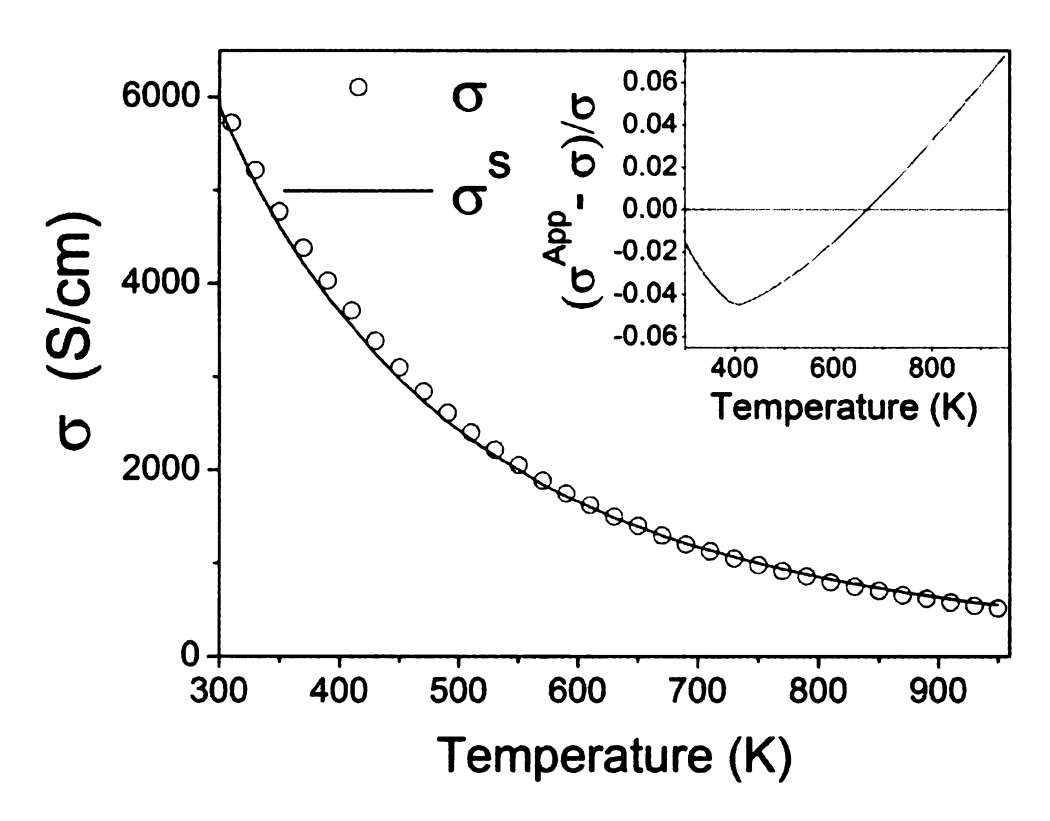


Figure 5.8 A comparison between the electrical conductivity  $\sigma$  using the scattering mechanisms of the relaxation time with the scaled formula.

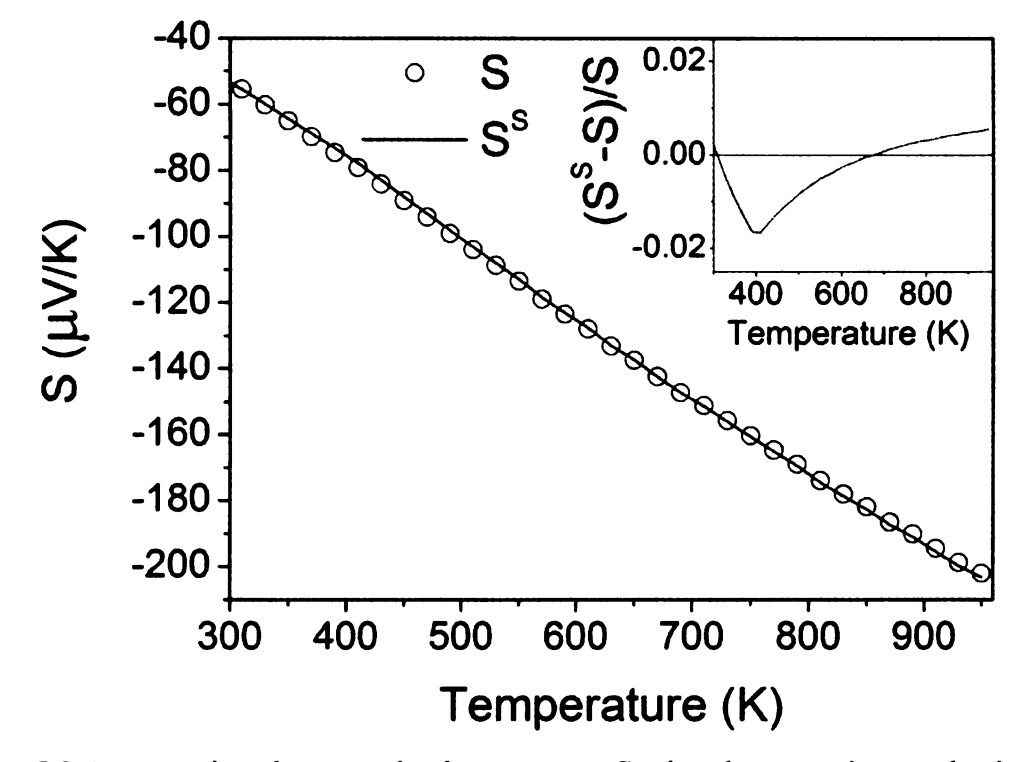


Figure 5.9 A comparison between the thermopower S using the scattering mechanisms of the relaxation time with the scaled formula.

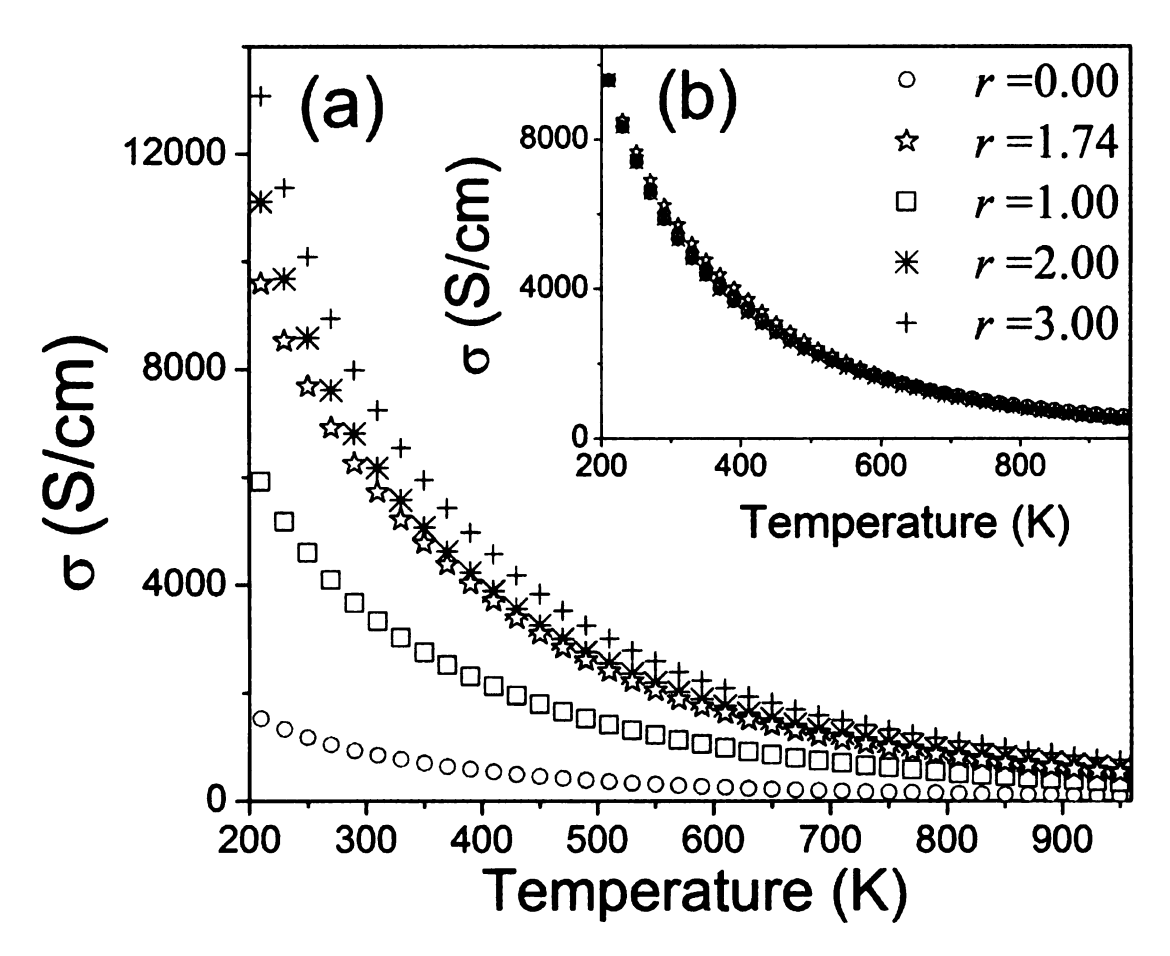


Figure 5.10 (a) Temperature dependence of  $\sigma$ , using the scaling formula of the total relaxation time for different r parameter. (b) Temperature dependence of the scaled  $\sigma$  (to r = 1.74).

levels of thermoelectric interest, differs significantly from both highly degenerate limit and the non-degenerate limit [9], and is somewhere in between.

## 5.7.2 Electronic Thermal Conductivity and the Validity of Wiedemann-

#### Franz law

We will now use the full T and  $\varepsilon$  dependence of the effective relaxation time (using our scaled form Eq. 5.88), T dependence of chemical potential and other parameters to look at the electronic thermal conductivity. Our work is a generalization of the earlier work by Bhandari and Rowe [104] who looked at this problem but only with acoustic phonon scattering. They had claimed that the acoustic phonon scattering was the dominant scattering mechanism in PbTe at high temperature. Our calculations for  $\tau_{tot}$ , as we discussed earlier in Sec. 5.5, show that it is not appropriate to ignore the deformation potential  $(\tau_o)$  and polar  $(\tau_{po})$  scattering by optical phonons to get a proper understanding of the transport coefficients. Our results for the electronic thermal conductivity match perfectly with their results if we only consider the acoustic phonon scattering. In Fig. 5.11 we give the T dependence of  $\kappa_{el,E}$  and  $\kappa_{el,J}$ . Both decrease with T but the difference increases with T. One question is how close PbTe is to a perfect thermoelectric ( $ZT = \infty$  when  $\kappa_l = 0$ , see Eq. 5.87). In this limit,  $ZT = \sigma S^2 T / \kappa_{el,J} =$  $(\kappa_{el,E}/\kappa_{el,J}) - 1$ . We plot this quantity in Fig. 5.12, it goes from ~0.1 at 300K (metallic limit) to ~ 3 at 900K. PbTe does approach a perfect thermoelectric at high temperatures but is far from it.

Next we address the validity of Wiedemann-Franz (WF) law. The first question is whether  $\kappa_{el,E} = L_0 \sigma T$  or  $\kappa_{el,J} = L_0 \sigma T$  where  $L_0 = 2.45 \times 10^{-8} W\Omega/K^2$ ? For a metal or a highly degenerate semiconductor it is the first equation that is correct. [9, 123] We can

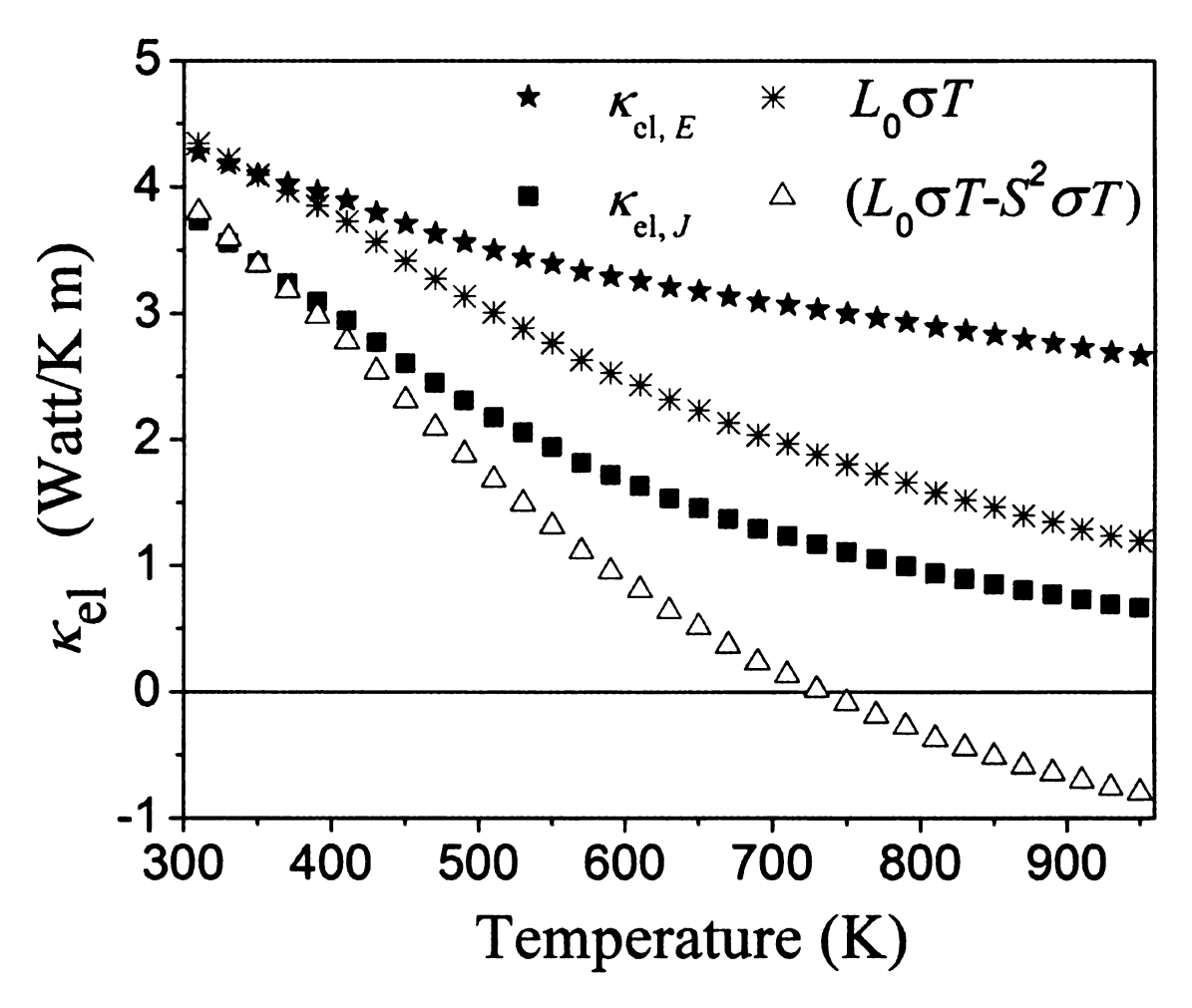


Figure 5.11 Temperature dependence of the electronic thermal conductivity  $(\kappa_{el})$  at constant electric field E  $(\kappa_{el,E})$  and at constant current density J  $(\kappa_{el,J})$  using Boltzmann transport equations. We also give their values using WF law.

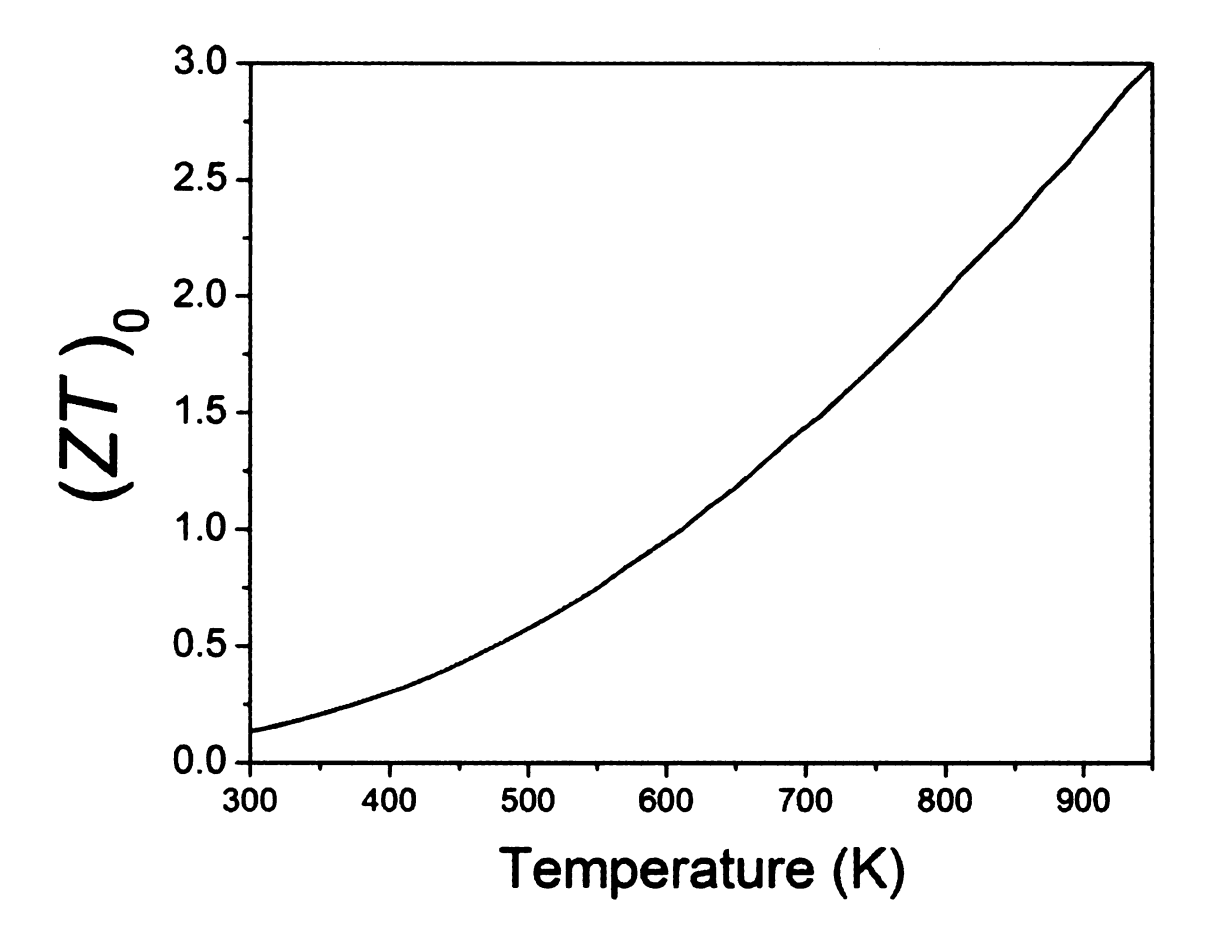


Figure 5.12 Temperature dependence of ZT for *n*-type PbTe at concentration  $n = 5 \times 10^{19}$  cm<sup>-3</sup> assuming  $\kappa_l = 0$ .

use the calculated  $\sigma$  (Fig. 5.8) and this equation to estimate  $\kappa_{el,E}$ . However there is a fundamental problem! If we use this as  $\kappa_{el,E}$  then estimate  $\kappa_{el,J}$  using the calculated values of  $\sigma$  and S (the plot  $L_0\sigma T - S^2\sigma T$  in Fig. 5.11), we find that for T > 700 K,  $\kappa_{el,J} < 0$ . But since  $\kappa_{el,J}$  is a response function it must be positive definite. So we cannot use the equation  $\kappa_{el,E} = L_0\sigma T$  to estimate  $\kappa_{el,E}$  from experimental  $\sigma$  and then calculate  $\kappa_{el,J}$  using the experimental value of  $\sigma$  and S.

The next thing we can do is to use the second equation,  $\kappa_{el,J} = L_0 \sigma T$ . This appears to be more reasonable and is closer to the values of properly calculated  $\kappa_{el,J}$ . This

is what is usually done in the estimation of electronic contribution to the total thermal conductivity  $\kappa_{tot}$  using experimental values of  $\sigma$ , S. As we can see in Fig. 5.11, the use of WF law overestimates the electronic contribution  $\kappa_{el} \equiv \kappa_{el,J}$  and therefore underestimates the lattice contribution. The proper lattice contribution should be actually higher (by more than 0.5 W K<sup>-1</sup>m<sup>-1</sup>).

In order to find the temperature dependence of electronic thermal conductivity at constant current  $(\kappa_{el,J})$ , one defines an effective Lorenz number as [122]

$$L = \frac{\kappa_{el,J}}{\sigma T} \,. \tag{5.89}$$

Fig. 5.13 shows the effective Lorenz number vs. temperature for different carrier concentrations. As we can see, the effective Lorenz number L approaches  $L_0$  (metallic like electric thermal conductivity) with increasing concentration and decreasing temperature. As pointed out in Sec. 5.6, for a perfect thermoelectric  $\kappa_{el,J} = 0$ , i.e. L = 0.

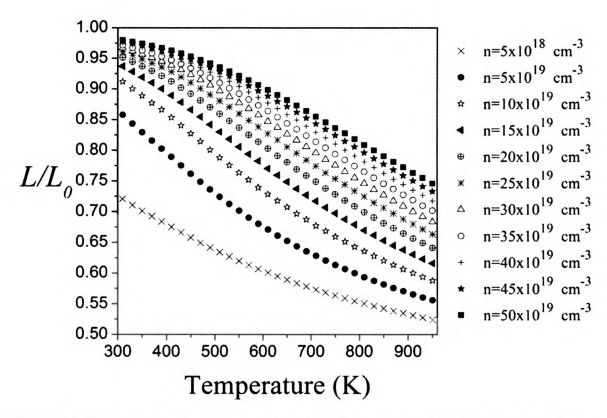


Figure 5.13 Temperature dependence of the scaled effective Lorenz number ( $L/L_0$ ) for *n*-type PbTe at different concentration n. ( $L_0=2.45\times10-8~W\Omega K^{-2}$ )

#### 5.8 Summary

Transport calculations using the nonparabolic Kane model for energy dispersion in PbTe show that the deformation potential of acoustic phonons  $(\tau_a)$ , the deformation potential of optical phonons  $(\tau_o)$ , and the polar scattering by optical phonons  $(\tau_{po})$ , are comparable and make significant contributions at temperatures above 300 K. Temperature and energy dependence of the total relaxation time  $\tau_{tot}$  calculations show that the T-dependence comes from two sources, one from the high-T limit of phonon occupation number and the other from the density of states associated with the carriers. In the temperature range 300 K < T < 900 K,  $\sigma(T)$  for n-type PbTe  $\sim T^{-2.2}$ . This T-dependence of  $\sigma$  comes from several sources (band structure parameters i.e. effective

mass, chemical potential  $\mu$  and relaxation time  $\tau$ ), the T-dependence of  $\tau$  ( $\sim T^{-1.4}$ ) however dominates, the other important source being a strong T-dependence of  $\mu$ . It turns out that energy dependence of  $\tau_{tot}(T,\varepsilon)$  does not seem to control the T-dependence of  $\sigma$  in this temperature range and for carrier concentration ( $n \sim 10^{19} cm^{-3}$ ). This should have implications in current attempts to change the energy dependence of electron scattering to control the T-dependence of  $\sigma$ .

Careful electronic thermal conductivity calculations were done using the same model and parameters which were used to fit  $\sigma$  and S. Our calculations show that using WF law  $(\kappa_{el,J} = L_0 \sigma T)$  to estimate this contribution of the thermal conductivity will overestimate the electronic contribution and hence underestimate the lattice contribution to the total thermal conductivity. This suggests that the very low values of lattice thermal conductivity found from using WF law may not be quite right.

## Chapter 6

## **General Summary**

PbTe was one of the first materials studied in the middle of the last century when there was a revival of interest in thermoelectricity.[4] This compound, its alloys with SnTe and PbSe, and related compounds called TAGS (alloys of AgSbTe<sub>2</sub> and GeTe) were for many years the best thermoelectric materials at temperatures ~700 K.[5] In recent years, quantum wells of PbTe/Pb<sub>1-x</sub>Eu<sub>x</sub>Te, PbSe<sub>0.98</sub>Te<sub>0.02</sub>/PbTe superlattices.[6] and quaternary compounds AgSbPb<sub>2m</sub>Te<sub>2m+2</sub> (m=9,10) [7] have attracted considerable attention because of their large thermoelectric figure of merit (FOM). Similar quaternary systems with Ag replaced by Na are also promising high temperature thermoelectric [8]. Most of the above systems have stoichiometry closer to the parent compound PbTe. This has lead to a great deal of experimental and theoretical activity in PbTe and similar IV-VI narrow band-gap semiconductors in last few years.

A detailed microscopic understanding of the nature of the defect states in PbTe and SnTe has been an old but a challenging problem, because it is known that, in narrow band-gap semiconductors like PbTe and SnTe, one does not see shallow defect states but deep defect states (DDS) which need not be inside the band gap.[11-15] Inspite of several theoretical attempts the problem of defects in PbTe, particularly the physics underlying deep defect states, has not been well understood until my *ab initio* density functional studies presented in this thesis.

Several calculations of the transport coefficients of PbTe and related systems have been reported over the years. [52, 95, 102, 104, 105] These earlier works did not explore the relationship between the energy and temperature dependence of the effective relaxation rate and the T-dependence of  $\sigma$ ,  $\kappa_{el,J}$  and  $\kappa_{el,E}$ . Although the validity of using Wiedemann-Franz (WF) law [123] to obtain electronic thermal conductivity at high temperatures has been questioned in the literature [104], it is still widely used to estimate the lattice thermal conductivity from the total experimental thermal conductivity. The lattice thermal conductivities estimated this way are turning out to be very small, well below the so called alloy limit [136]. This reduction has been attributed to the enhanced phonon scattering from the nanostructures present in the samples. Thus to have a more definite picture one must critically examine the use of WF law.

In my thesis, I have presented two major contributions in PbTe and related systems. (1) Results of my calculations to understand the physics behind the formation of deep defect states in PbTe and SnTe using self-consistent *ab initio* electronic structure calculations within density functional theory (DFT) and supercell models, and (2) A careful investigation of the energy and temperature dependent transport processes in *n*-doped PbTe, particularly at high temperatures.

Electronic structure calculations on defects in PbTe show that when a Pb atom is substituted by a defect, the single particle density of states (DOS) gets perturbed over the entire valence and conduction bands. In addition, there are major changes in the DOS near the band gap region for most of the defects. This should have significant impact on the transport properties of these new compounds. We find that Na does not change the DOS within 0.5 eV of the valence and conduction band extrema; thus it is an ideal

acceptor. In contrast, other alkali atoms and Ag and Cu give rise to an increase in the DOS near the top of the valence band and negligible change in the DOS near the bottom of the conduction band. The divalent defects (s<sup>2</sup>-type) Hg, Cd, Zn give rise to resonant states near the bottom of the conduction band and suppress the DOS near the top of the valence band (which is good for *n*-type thermoelectrics). Group V (As, Sb and Bi) impurities ( $p^3$ -type) introduce resonant states in the conduction band and should be good for *n*-type thermoelectrics. In contrast, the trivalent impurities (Ga, In, and Tl;  $s^2p^1$ -type) either introduce bound states in the gap or resonant states near the bottom of the conduction band or the top of the valence band. My calculations strongly suggest that the currently used mixed valence model [43-45] for these defects is not correct. Te vacancy also has a strong effect on the DOS of PbTe near the band gap region. New states appear in the band gap below the CBM, these states comprise primarily of the p states of Pb neighboring the vacancy. In contrast, the Pb vacancy increases the DOS near the top of the valence band but by a small amount. Te vacancy should be n-type whereas Pb vacancy should be p-type. Iodine appears to be an ideal donor, it does not change the DOS of PbTe near the band gap, just shifts the Fermi energy to the conduction band. The divalent atoms S and Se also do not change the DOS near the CBM. There is however some depletion of the DOS near the VBM. These results should have important implications in the thermoelectric properties of, e.g., the n-type ternary compound PbTe<sub>1-x</sub>S<sub>x</sub>, [53] where one can synthesize mixed Te/S systems without appreciably affecting the conduction-band states and hence the *n*-type charge and energy transport.

Electronic structure calculations of defects in SnTe show that when a Sn atom is substituted by a defect, the DOS of the valence and conduction bands get strongly

perturbed, similar ti PbTe. Sn vacancy causes very little change near the bottom of the conduction band DOS whereas there is an increase in the DOS near the top of the valence band. Te vacancy on the other hand creates new states in the band gap region and near the bottom of the conduction band. Ag impurity perturbs the valence band states due to the Ag d-states hybridizing with the Te p bands. The difference in the total DOS with and without Ag impurity shows a small peak near the top of the valance band. Sb impurity shows resonant states near the bottom of the SnTe conduction band. Results for In impurity shows that, unlike PbTe, the deep defect states in SnTe are resonant states near the top of the valence band. In PbTe these deep defect states lie in the band-gap region (act as n-type). This fundamental difference in the position of the deep defect states in SnTe and PbTe explains the experimental anomalies seen in the case of In impurities (act as n-type in PbTe and p-type in SnTe).[13, 87] In addition, we also find a major difference in Cd-induced defect states in PbTe and in SnTe. This has to do with the valence s-states of Sn which are strongly perturbed by the defects. In contrast, Pb valence s do not get perturbed by the defect. However, more careful calculations are needed to understand the physics behind this difference between Cd defects states in PbTe and SnTe.

Transport calculations in PbTe show that scattering rates associated with deformation potential of acoustic phonons  $(\tau_a)$ , the deformation potential of optical phonons  $(\tau_o)$ , and the polar scattering by optical phonons  $(\tau_{po})$ , are all comparable. All these make significant contributions at temperatures above 300 K. Temperature and energy dependence of the total relaxation time  $\tau_{tot}$  calculations show that the T-dependence comes primarily from two sources, one from the high-T limit of phonon

occupation number and the other from the density of states associated with the carriers. In the temperature range 300K < T < 900K, for n-type PbTe we find  $\sigma(T) \sim T^{-2.2}$ , in agreement with experiment. This T-dependence of  $\sigma$  comes from several sources (band structure parameters i.e. effective mass, chemical potential  $\mu$  and relaxation time  $\tau_{tot}$ ). The T-dependence of  $\tau_{tot}$  ( $\sim T^{-1.4}$ ) however dominates, the other important source being a strong T-dependence of the chemical potential  $\mu$ . It turns out that energy dependence of  $\tau_{tot}(T,\varepsilon)$  does not seem to control the T-dependence of  $\sigma$  in this temperature range and for carrier concentration ( $n \sim 10^{19} cm^{-3}$ ). This should have implications in current attempts to change the energy dependence of electron scattering to control the T-dependence of  $\sigma$ . [102, 103]

Careful electronic thermal conductivity calculations were done using the same model parameters which were used to fit  $\sigma$  and S. Our calculations show that using WF law  $(\kappa_{el,J} = L_0 \sigma T)$  overestimates the electronic contribution. Subtracting this from measured total thermal conductivity therefore underestimates the lattice contribution. This suggests that the very low values of lattice thermal conductivity found from using WF law may not be quite right.

Finally, I would like to make few general remarks. Electronic structure calculations within density functional theory (DFT) offer varieties of tools to determine the stability of compounds, their atomic geometries, their band structure and transport properties. Within DFT the stability of compounds (their total energies) are well predicted. Therefore, the theory can indeed help in predicting new compounds with new electronic properties. One can use these calculations not only to understand why already synthesized good thermoelectric materials show these properties, but also to search for

new potential thermoelectric materials. However, the issue of how accurate the DFT studies of defect states using supercell models, one needs further calculations with larger supercell. More quantitative studies (experimental) and comparison with theoretical calculations are needed to check that.

In order to characterize the thermoelectric properties of a material, transport calculations for  $\sigma$ , S, and  $\kappa_{el}$  have to be performed carefully. Unfortunately, to perform such calculations one has to make approximations whose validity is not always fully under control. By this I mean that we do not have an estimate of the magnitude of the errors made. Approximation such as the rigid band model, where the electronic band structure of doped semiconductors is assumed to be the same as for the undoped semiconductors, needs to be critically examined. We saw that the host band structures do get modified strongly for defect concentrations  $\gtrsim 1\%$ . The other approximation is the relaxation time approximation made in describing the electronic scattering mechanisms.

The other problem we would like to mention is the problem of LDA/GGA in underestimating the band-gap. [32, 61] For narrow band-gap semiconductors, which most good thermoelectric are, this could be a problem in calculating the transport coefficients. Although methods like GW approximation [68] have developed in recent years, their applications to study the electronic structure and transport properties of complex materials are still at their its infancy. One expects considerable theoretical effort to be put in this direction in the future. I believe strongly that for a proper understanding of transport properties of complex systems a close interaction between theory and experiment is necessary.

## REFERENCES

- [1] G. P. Agrawal and N. K. Dutta, *Semiconductor Lasers* (van Nostrand Reinhold, New York, 1993), p.547; S. Chatterjee and U. Pal, Optical Eng. 32, 2923 (1993).
- [2] T. K. Chaudhuri, Int. J. Energy Res. 16, 481 (1992).
- [3] J. H. Dughaish, Physica B **322**, 205 (2002).
- [4] A. F. Ioffe, Semiconductor Thermoelements and Thermoelectric Cooling (Infosearch, London, 1957).
- [5] E. A. Skrabek and D. S. Trimmer, in CRC Handbook of Thermoelectrics, edited by D. M. Rowe (CRC Press, Boca Raton, 1995), p.267.
- [6] T. C. Harman, D. L. Sprears, and M. J. Manfra, J. Electron. Mater. 25, 1121 (1996);
   T. C. Harman, P. J. Taylor, M. P. Walsh, and B. E. LaForge, Science 297, 2229 (2002).
- [7] K. F. Hsu, S. Loo, F. Guo, W. Chen, J. S. Dyck, C. Uher, T. Hogan, E. K. Polychroniadis, and M. G. Kanatzidis, Science 303, 818 (2004).
- [8] P. F. P. Poudeu, J. D'Angelo, A. D. Downey, J. L. Short, T. P. Hogan, and M. G. Kanatzidis, Angew. Chem. Int. Ed. 45, 3835 (2006).
- [9] G. S. Nolas, J. Sharp, and H. J. Goldsmidt, *Thermoelectrics: Basic Principles and New Materials Development* (Springer, Berlin, 2001).
- [10] S. D. Mahanti, P. M. Larson, D. Bilc, and H. Li, in *Chemistry, Physics, and Material Science of Thermoelectric Materials: Beyond Bismuth Telluride*, edited by M. G. Kanatzidis, S. D. Mahanti, and T. Hogan (Kluwer Academic, New York, 2003), p.227; N. P. Blake and H. Metiu, *ibid.*, p.259.
- [11] S. T. Pantelides (Ed.), Deep Centers in Semiconductors: A State-of-the-Art Approach (Grodon and Breach Science, Yverdon, Switzerland, 1992). For a more recent discussion of shallow versus deep defects and the role of defects in semiconductor see, e.g., H. J. Queisser and E. E. Haller, Science 281, 945 (1998).
- [12] S. T. Pantelides, Rev. Mod. Phys. **50**, 797 (1978).
- [13] C. S. Lent, M. A. Bowen, J. D. Dow, R. S. Allgaiger, O. F. Sankey, and E. S. Ho, Solid State Commun. 61, 83 (1987).
- [14] N. J. Parada and G. W. Pratt, Phys. Rev. Lett. 22, 180 (1969).
- [15] N. J. Parada, Phys. Rev. B 3, 2042 (1971).

- [16] W. Kohn and J. M. Luttinger, Phys. Rev. 98, 915 (1955); W. Kohn, Solid StatePhysics, edited by F. Seitz and D. Turnbull (Academic, New York, 1957), vol. 5.
- [17] B. A. Volkov, L. I. Ryabova, and D. R. Khokhlov, Physics-Uspekhi 45, 819 (2002).
- [18] S. Ahmad, K. Hoang, and S. D. Mahanti, Phys. Rev. Lett. **96**, 056403 (2006); **96**, 169907(E) (2006).
- [19] D. Bilc, S. D. Mahanti, E. Quarez, K.-F. Hsu, R. Pcionek, and M. G. Kanatzidis, Phys. Rev. Lett. 93, 146403 (2004).
- [20] D. J. Singh, *Planewaves, Pseudopotentials, and the LAPW Method* (Kluwer Academic, Boston, 1994).
- [21] A. H. Edwards, A. C. Pineda, P. A. Schultz, M. G. Martin, A. P. Thompson, and H. P. Hjalmarson, J. Phys.: Condens. Matter 17, L39 (2005).
- [22] S. Lany, H. Wolf, and T. Wichert, Phys. Rev. Lett. 92, 225504 (2004).
- [23] S. D. Mahanti and D. Bilc, J. Phys.: Condens. Matter 16, S5277 (2004).
- [24] S. Ahmad, D. Bilc, S. D. Mahanti, and M.G. Kanatzidis, in Semiconductor Defect Engineering- Materials, Synthetic Structures and Devices, edited by S. Ashok, J. Chevallier, B.L. Sopori, M. Tabe, and P. Kiesel (Mater. Res. Soc. Symp. Proc. 864, Warrendale, PA, 2005), E9.23.
- [25] H. Overhof and U. Sossler. Phys. Stat. Sol., 37 691, 1970.
- [26] G. Martinez, M. Schluter, and M.L. Cohen. Phys. Rev. B 11, 651 (1975).
- [27] J.A. Valdivia and G.E. Barberis, J. Phys. Chem. Sol., **56**, 1141(1995).
- [28] S.H. Wei and A. Zunger, Phys. Rev. B 55, 13605 (1997).
- [29] E.A. Albanesi, C.M.I. Okoye, C.O. Rodriguez, E.L.P.Y. Blanca, and A.G. Petukhov, Phys. Rev. B 61, 16589 (2000).
- [30] M. Lach-hab, D.A. Papaconstantopoulos, and M.J. Mehl, J. Phys. Chem. Sol. 63, 833 (2002).
- [31] P. Hohenberg and W. Kohn, Phys. Rev. 136, B864 (1964).
- [32] J. P. Perdew, K. Burke, and M. Ernzerhof, Phys. Rev. Lett. 77, 3865 (1996).

- [33] K.I. Shimizu, Y. Nisida, and S.I. Narita, J. Phys. Soc. Japan 46, 1797 (1979).
- [34] W.E. Tennant, Solid State Commun. 20, 613 (1976).
- [35] R.F.W. Bader, Atoms in Molecules A Quantum Theory. Oxford University Press, 1990.
- [36] Peter A. Schultz, Phys. Rev. Lett. 96, 246401 (2006), and references therein.
- [37] P. Blaha, K. Schwarz, G. K. H. Madsen, D. Kvasnicka, and J. Luitz, WIEN2k, An Augmented Plane Wave + Local Orbitals Program for Calculating Crystal Properties, edited by Karlheinz Schwarz (Technische Universitat Wien, Austria, 2001).
- [38] D. D. Koelling and B. Harmon, J. Phys. C 13, 6147 (1980).
- [39] Y. Noda, K. Masumoto, S. Ohba, Y. Saito, K. Toriumi, Y. Iwata and I. Shibuya, Acta Cryst. C 43, 1443 (1987).
- [40] P. E. Blöchl, Phys. Rev. B **50**, 17953 (1994); G. Kresse and D. Joubert, *ibid* **59**, 1758 (1999).
- [41] G. Kresse and J. Hafner, Phys. Rev. B 47, 558 (1993); 49, 14251 (1994); G. Kresse and J. Furthmüller, *ibid* 54, 11169 (1996); Comput. Mater. Sci. 6, 15 (1996).
- [42] Y. Gelbstein, Z. Dashevsty, and M. P. Daviel, Physica B 363, 196 (2005).
- [43] L. I. Ryabova and D. R. Khokhlov, JETP Lett. 80, 133 (2004).
- [44] I. A. Drabkin and B.Ya. Moizhes, Fiz. Tekh. Poluprovodn. 17, 969 (1983) [Sov. Phys. Semicond. 17, 611 (1983)]; B. A. Valkov and O. A. Pankratov, Sov. Phys. JETP 61, 164 (1985).
- [45] D. R. Khokhlov and B. A. Volkov, in *Proceedings of the 23rd International Conference on Physics of Semiconductors, Berlin, 1996* (World Scientific, Singapore, 1996), Vol. 4, p. 2941.
- [46] P.W. Anderson, Phys. Rev. Lett. 34, 953 (1975).
- [47] B. A. Volkov and O. M. Ruchaiskii, JETP Lett. 62, 217 (1995).
- [48] H. P. Hjalmarson, P. Vogl, D. J. Wolford, and J. D. Dow, Phys. Rev. Lett. 44, 810 (1980).
- [49] V. I. Kaĭdanov, Y. I. Ravich, Usp. Fiz. Nauk 145, 51 (1985) [Sov. Phys. Usp. 28, 31 (1985)].

- [50] S. Ahmad, S.D. Mahanti, K. Hoang, and M. G. Kanatzidis, Phys. Rev. B, 74 155205 (2006).
- [51] H. Hazama, U. Mizutani, and R. Asahi, Phys. Rev. B 73, 115108 (2006).
- [52] D. Bilc, S. D. Mahanti, and M. G. Kanatzidis, Phys. Rev. B 74, 125202 (2006).
- [53] J. Androulakis, R. Pcionek, E. Quarez, O.Palchik, H. Kong, C. Uher, J. J. Dangelo, T. Hogan, X. Tang, T. Tritt, and M. G. Kanatzidis, in *Materials and Technologies for Direct Thermal-to-Electric Energy Conversion*, edited by Jihui Yang, Timothy P. Hogan, Ryoji Funahashi, George S. Nolas (Mater. Res. Soc. Symp. Proc. 886, Warrendale, PA, 2006), F05-08.
- [54] E. Kaxiras, Atomic and Electronic Structure of solids, Cambridge University Press, (2003).
- [55] W. Kohn, L. J. Sham, Phys. Rev. 136, B864 (1964).
- [56] J. Kohanoff, Electronic Structure Calculations for Solids and Molecules: Theory and Computational Methods, Cambridge University Press, (2006).
- [57] J. Kubler and V. Eyert. *Electronic structure calculations, in: Electronic and Magnetic Properties of Metals and Ceramics*, volume 3A. VCH Verlagsgesellschaft, Weinheim, 1992.
- [58] M. Richter, J.Phys. D: Appl. Phys. 13, 1017 (1998).
- [59] H. Jansen. Phys. Rev. B 7, 1912 (1988).
- [60] H. Eschrig, G. Seifert, and P. Ziesche, Solid State Commun. 56, 777 (1985).
- [61] R. O. Jones and O. Gunnarsson. Rev. Mod. Phys. 61, 689 (1989).
- [62] W. Kohn and L. J. Sham. Phys. Rev. 140, A1133 (1965).
- [63] J. P. Perdew and Y. Wang, Phys. Rev. B 45, 13244 (1992).
- [64] A. K. Rajagobal, J. of phys. C 11, L943 (1978).
- [65] A. K. Rajagobal, and J. Callaway, Phys. Rev. B 7, 1912 (1973).
- [66] A. H. MacDonald and S. H. Vosko, J. Phys. C: Solid state Phys. 12, 2977 (1979).
- [67] A. Gonis, Theoretical Material Science, Material Research Society (2000).

- [68] W. G. Aulber, L. Jonsson, and J. W. Wilkins, Solid State Physics 54, Academic Press, Orlando (2000).
- [69] D.A. Drabold, and S. K. Estreicher, Topics in Applied Physics: Theory of Defects in Semiconductors (2007).
- [70] R. P. Messmer, G. D. Watkins, Phys. Rev. lett. 25, 656 (1970).
- [71] S. Ögut, H. Kim, J. R. Chelikowsky, Phys. Rev. B 56, R11353 (1997).
- [72] G. Baraff, M. Schlüter, Phys. Rev. B 19, 4965 (1979).
- [73] O. Gunnarsson, O. Jepsen, and O. K. Anderson, Phys. Rev. 27, 7144 (1983).
- [74] M. J. Puska, O. Jepsen, O. Gunnarsson, and R. M. Nieminen, Phy. Rev. B 34, 2695 (1986).
- [75] S. B. Zhang, J. E. Northrup, Phys. Rev. Lett. 67, 2339 (1991).
- [76] J. J. Sakurai, Advanced Quantum Mechanics. Addision Wesely (1967).
- [77] D. D. Koelling and B. Harmon, J. Phys. C 10, 3107 (1977).
- [78] A. H. MacDonald, W. E. Pickett, and D. D. Koelling, J. Phys. C 13, 2675 (1978).
- [79] M. J. Puska, S. Pöykkö, M. Pesola, and R. M. Nieminen, Phys. Rev. B 58, 1318 (1998).
- [80] C. M. I. Okoye, J. Phys.: Condens. Matter 14, 8625 (2002).
- [81] P. J. Lin, W. Saslow and M. L. Cohen, Solid State Commun. 5, 893 (1967).
- [82] F. Herman, R. L. Kortum, I. B. Ortenburger, and J. P. Van Dyke, J. Physique Coll. **29** (Suppl.) C4 62 (1968).
- [83] S. Rabii, Phys. Rev. 182 821 (1969); S. Rabii, Bull. Am. Phys. Soc. 13 413 (1968).
- [84] K. M. Rabe, and J. D. Joannopoulos, Phys. Rev. B 32 2302 (1985).
- [85] R. F. Bis, and J. R. Dixon, J. Appl. Phys. 40, 1919 (1969).
- [86] L. Esaki, and P. J. Stiles, Phys. Rev. Lett. 16 1108 (1966); L. Esaki, J. Phys. Soc. Japan 21, 589 (1966); R. Tsu, W. E. Howard, L. and Esaki, Phys. Rev. 172, 779 (1968).
- [87] S A Nemov, Yu I Ravich, Physics-Uspekhi 41 (8) 735 (1998).

- [88] D. Khokhlov, Lead Chalcogenides: Physics and Applications, Vol. 18 of Optoelectronic Properties of Semiconductors and Superlattices (Taylor and Francis, New York, 2003).
- [89] C. Wetzel et al., Phys. Rev. Lett. 78, 3923 (1997).
- [90] A. K. Ramdas and S. Rodriguez, Rep. Progr. Phys. 44, 1297 (1981).
- [91] S. T. Pantelides, Ed., Deep Centers in Semiconductors: A State-of-the-Art approach (Gordon & Breach, Lausanne, Switzerland, ed. 2, 1992); A. M. Stoneham, Theory of Defects in Solids (Clarendon, Oxford, 1975).
- [92] G. A. Slack, (1997) in *Thermoelectric Materials-New Directions and Approaches, Symp. Proc. Mater. Res. Soc.*, ed. T. M. Tritt, M. G. Kanatzidis, H. B. Lyon, G. D. Mahan, 478:47-54. Pittsburgh: Mater. Res. Soc.
- [93] H. J. Goldsmid, and A. W. Penn, Phys. Lett. A 27, 523-524 (1968).
- [94] P.G. Klemens, (1991) in Modern Perspectives On Thermoelectrics and Related Materials, eds. D.D. Alred, C. B. Vining, & G. A. Slack, (Materials Res. Soc., Pittsburg), p. 87.
- [95] L.D. Hicks and M.S. Desselhaus, Phys. Rev. B 47, 12 727(1993).
- [96] J.O. Sofo and G.D. Mahan, Phys. Rev. B 49, 4565 (1994).
- [97] G.L. Bennett, in: D.M. Rowe (Ed.), CRC Handbook of Thermoelectrics, CRC Press, New York, 1995, pp. 515–537.
- [98] P. Zhu, Y. Imai, Y. Isoda, Y. Shinohara, X. Jia and G. Zou, J. Phys.: Condens. Matter 17, 7319 (2005).
- [99] K. Kishimoto and T. Koyanagi, J. Appl. Phys. 92 2544 (2002).
- [100] G. D. Mahan, Solid State Phys. 51 81 (1998).
- [101] T. C. Harman, D. L. Sprears, and M. J. Manfra, J. Electron. Mater. 25, 1121 (1996); T. C. Harman, P. J. Taylor, M. P. Walsh, and B. E. LaForge, Science 297, 2229 (2002).
- [102] J.P. Heremans, C.M. Thrush and D.T. Morelli, Phys. Rev. B 70, 115334 (2004).
- [103] J. R. Sootsman, H. Kong, C. Uher, A. Downey, J. James, D. Angelo, C. Wu, T. P. Hogan, T. Caillat, and M. G. Kanatzidis (unpublished).

- [104] C.M. Bhandari and D. M. Rowe, J. Phys. D: Appl. Phys. 18, 873 (1985).
- [105] M.P. Singh and C.M. Bhandari, J. Phys. 62, 1309 (2004).
- [106] D. M. Zayachuk, Semiconductors 31, 173 (1997).
- [107] D. M. Freik, L. I. Nykyruy, and V. M. Shperun, Semicond. Phys., Quantum Electron. Optoelectron. 5, 362 (2002).
- [108] J. Callaway and A.J. Hughes, Phys. Rev. 156, 860 (1967) and 164, 1043 (1967).
- [109] S.T. Pantelides in *Deep Centers in Semiconductors*, ed. S.T. Pantelides (Gordon and Breach, New York, 1986)
- [110] G.F. Koster and J.C. Slater, Phys. Rev. 95, 1167 (1954) and 96, 1208 (1954)
- [111] J. Callaway, J. Math. Phys. 5, 783 (1964)
- [112] F. Aryasetiawan and O. Gunnarsson, Rep. Prog. Phys. 61, 237 (1998)
- [113] F.P.Larkins, J. Phys. C: Sol. St. Phys. 4, 3065 (1971)
- [114] D.R. Hamann, M. Schlüter, and C. Chiang, Phys. Rev. Lett. 43, 1494 (1979)
- [115] R. Car and M. Parrinello, Phys. Rev. Lett. 55, 2471 (1985)
- [116] A. Zunger and A. Katzir, Phys. Rev. B 11, 2378 (1975)
- [117] L. Nordstrom and D. J. Singh, Phys. Rev. B 53, 1103 (1996)
- [118] N. P. Blake, S. Latturner, J. D. Bryan, G. D. Stucky, and H. Metiu, J. Chem. Phys., 115:8060 (2001)
- [119] P. Larson, S. D. Mahanti, and M. G. Kanatzidis, Phys. Rev. B 61, 8162 (2000)
- [120] P. Larson, S. D. Mahanti, and M. G. Kanatzidis, Phys. Rev. B 65, 045205 (2002)
- [121] P. Larson, S. D. Mahanti, S. Sportouch, and M. G. Kanatzidis, Phys. Rev. B 59, 15660 (1999)
- [122] J. R. Drabble, and H.J. Goldsmid, International Series of Monographs on Semicondoctors: *Thermal Conduction in Semiconductors*, Volume 4 (Pergamon Press, 1961).
- [123] J. M. Ziman, *Principles of The Theory of Solids* (Cambridge University Press, New York, 1964), p. 179.

- [124] Yu. I. Ravich, B. A. Efimova, and I. A. Smirnov, Semiconducting Lead Chalcogenides (Plenum Press, New York, 1970), Vol. 5, p. 299.
- [125] Yu. I. Ravich, B. A. Efimova, and V. I. Tamarchenko, Phys. Status Solidi B 43, 11 (1971).
- [126] Y. W. Tsang and M. L. Cohen, Phys. Rev. B 3, 1254 (1971).
- [127] H. Yokoi, S. Takeyama, N. Miura, and G. Bauer, Phys. Rev. B 44, 6519 (1991).
- [128] B. A. Efimova, L. A. Kolomoets, Yu. I. Ravich, and T. S. Stavitskaya. Soviet Physics semiconductors 4, 1653 (1971).
- [129] W. Kohn, Sol. St. Phys. 5, 257 (1957).
- [130] S.T. Pantelides, Rev. Mod. Phys. **50**, 797 (1978)
- [131] T. A. Kaplan, and S. D. Mahanti, *Electronic Properties of Solids Using Cluster Methods*, Plenum Press, New York (1995).
- [132] J. Androulakis, K. F. Hsu, R. Pcionek, H. Kong, C. Uher, J. J. D'Angelo, A. Downey, T. Hogan, M. G. Kanatzidis, *Advanced Materials* 18, 1170 (2006).
- [133] E. O. Kane, Semiconductors and Semimetals, edited by R. K. Willardson and A. C. Beer (Academic Press, New York, 1975), Vol. 1, Chap. 3.
- [134] S. Lany, H. Wolf, and T. Wichert, Phys. Rev. Lett. 92, 225504 (2004).
- [135] T. Mattila, and A. Zunger, Phys. Rev. B 58, 1367 (1998).
- [136] W. Kim, R. Wang, and A. Majumdar, Nanotoday 2, (2007).
- [137] T. E. Humphrey, H. Linke, Phys. Rev. lett. 94, 096601 (2005).

